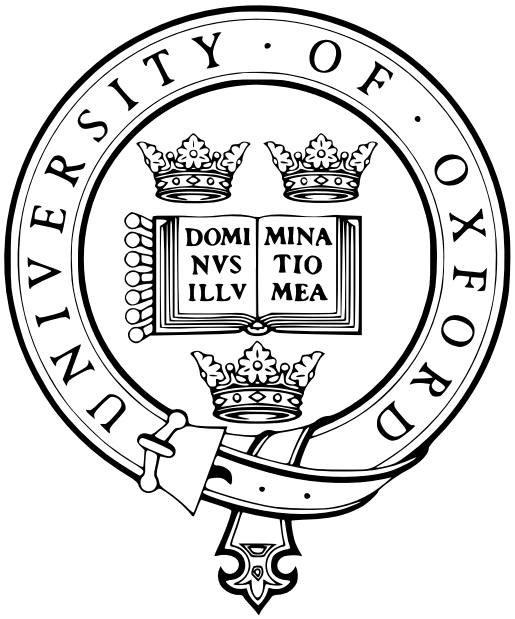


The colloidal liquid-gas interface: kinetics of phase separation, confinement and optical manipulation

Balkis Dohni

Lincoln College
University of Oxford

Supervisors: Prof. Roel P. A. Dullens
Prof. Dirk G. A. L. Aarts

A thesis submitted for the degree of
Doctor of Philosophy

December 2021

Abstract

In this thesis, the colloidal liquid-gas interface is studied. First, the evolution of colloidal gas-liquid phase separation in a colloid-polymer mixture through nucleation and growth is addressed. Using confocal microscopy, different statepoints are observed and three different mechanisms are found in distinct regions of the phase diagram: at low polymer concentration the colloidal liquid droplets coalesce until they fill the field of view, at higher polymer concentration, the colloidal liquid droplets stick to each other continuously throughout the entire observation period, and at the highest polymer concentration probed, the droplets stick to each other until a certain point where their size remains constant. Growth laws are computed and compared to theoretical predictions. The structure of the patterns formed as phase separation takes place and the motion of the growing droplets are analysed for each mechanism. Next, the thermal capillary waves of the colloidal liquid-gas interface in confinement are observed with confocal microscopy. The line tension as well as the dispersion relation are measured. The relaxation times of the modes of the fluctuations are measured and compared to theoretical predictions. Then, a tightly focused beam of laser light is used to nucleate a droplet of colloidal liquid into the colloidal gas phase for different laser powers and different heights above the colloidal liquid-gas interface. The kinetics of the growth and final size of the droplet were found to be unaffected by laser power and height above the colloidal liquid-gas interface. The kinetics of the growth of the droplet reveal that the growth is driven purely by electrostrictive effects and not by thermal gradients induced by the laser light. Finally, the evaporation of liquid droplets nucleated with optical tweezers is studied through fluorescence microscopy after the laser used for tweezing was switched off. From solving the diffusion equation, the diffusion coefficient of the colloids into the gas phase is measured. It is found not to vary with the height above the liquid-gas interface or the laser power used to nucleate the droplets. For droplets grown at a height of $20\,\mu$m, droplets sink at a constant velocity as they evaporate and interact with the liquid-gas interface below them.

Declaration

This thesis is submitted for the degree of Doctor of Philosophy in Physical and Theoretical Chemistry at the University of Oxford. No part of this thesis has been accepted or is currently being submitted for any degree, diploma, certificate or other qualification in this University or elsewhere. This thesis is wholly my own work, except where indicated.

Contents

Abstract **i**

Declaration **iii**

1 Introduction **1**

1.1 Interfaces 1

1.2 Colloidal systems 2

1.3 Colloidal interfaces 3

1.4 Manipulating the colloidal liquid-gas interface 4

1.5 Scope of the thesis 5

2 Background and experimental methods **7**

2.1 Colloidal systems 8

2.1.1 Definition, time and lengthscales 8

2.1.2 Colloidal interactions 10

2.2 Colloid-polymer mixtures 11

2.2.1 Depletion interaction 11

2.2.2 Phase diagram 12

2.2.3 Interface fluctuations 13

2.3 Confocal microscopy and optical tweezing 17

2.3.1 Confocal microscopy 17

2.3.2 Optical tweezing 18

2.4 Experimental methods 20
2.4.1 Preparation of the Xanthan solutions 20
2.4.2 Colloid synthesis 21
2.4.3 Experimental phase diagram 24
2.4.4 Experimental interface fluctuations 25
2.4.5 Optical tweezing setup 29

3 Dynamics of phase separation via nucleation and growth for a colloid-polymer mixture 33

3.1 Introduction 34
3.2 Theory of the kinetics of phase separation 36
3.3 Experimental methods 38
3.3.1 Sample cell 38
3.3.2 Image acquisition 39
3.4 Results and discussion 41
3.4.1 Phase diagram 41
3.4.2 Kinetics of growth 43
3.4.3 Structure 46
3.4.4 Motion of the droplets 49
3.5 Conclusion and outlook 50

4 Thermal capillary waves of a colloidal liquid-gas interface in confinement 53

4.1 Introduction 54
4.2 Theoretical background 55
4.2.1 Static case 55
4.2.2 Dynamic case: the dispersion relation 57
4.3 Experimental methods 61
4.3.1 Sample cell design 61

4.3.2 Data acquisition . . . 61
4.3.3 Bubble location and edge detection . . . 62
4.3.4 Corrections of the radii . . . 63
4.4 Results and discussion . . . 65
4.4.1 Droplet of statepoint 1 with $R_0 = 5\,\mu$m . . . 66
4.4.2 Droplet of statepoint 1 with $R_0 = 29\,\mu$m . . . 67
4.4.3 Comparison between statepoint 1 and 2 . . . 69
4.4.4 Measurement of the dispersion relation . . . 70
4.5 Conclusion and outlook . . . 72

5 Laser-induced formation of colloidal liquid droplets in the colloidal gas phase 77

5.1 Introduction . . . 78
5.2 Theory . . . 79
5.3 Experimental methods . . . 83
5.3.1 Sample cell design . . . 83
5.3.2 Image acquisition . . . 84
5.3.3 Image corrections and measurement of droplet radius . . . 84
5.4 Results and discussion . . . 85
5.4.1 Final size of the droplet . . . 85
5.4.2 Growth kinetics . . . 88
5.5 Conclusion and outlook . . . 91

6 Evaporation of laser-induced droplets of colloidal liquid in the colloidal gas phase 93

6.1 Introduction . . . 94
6.2 Theoretical background . . . 95
6.3 Experimental methods . . . 96
6.3.1 Image corrections . . . 96

6.4 Results and discussion 98
6.4.1 Droplet evaporation at height 20 μm 100
6.4.2 Droplet evaporation at heights 40 μm and 60 μm 103
6.5 Conclusion and outlook 106

7 Conclusion and future work **109**

Bibliography **113**

Acknowledgements **121**

Chapter 1

Introduction

1.1 Interfaces

Interfaces are found everywhere in nature and everyday life. They can be found between similar phases like the surface of vinegar droplets in oil, which is a liquid-liquid interface. Alloys, which have allowed humanity to create and manipulate stronger materials since as early as the Bronze age [1], the interface lies between two solid phases and is called grain boundaries. Interfaces can also separate phases of different nature. For instance, a raindrop on a window has three interfaces: one between the window and the drop, the second is between the droplet and the air, and the third is between the window and the air. In fact, there are as many types of interfaces as there are couples of phases.

Fluid interfaces have drawn an increasing interest over the past couple of decades [2]. The development of microfluidics in both academia and industry has meant working at scales where interfacial phenomena are dominating [3–5] and processes such as droplet formation, stability or coalescence are crucial to several different fields including cosmetics [6,7], food [8], oil recovery [9] and inkjet printing, where droplet detachment is a key phenomenon to control [10]. Most of these processes involve interfaces in molecular systems which are difficult to resolve at the molecular level. Their motion is very fast too, and interfacial phenomena involve complex mechanisms for which observation and control are difficult to achieve in molecular systems.

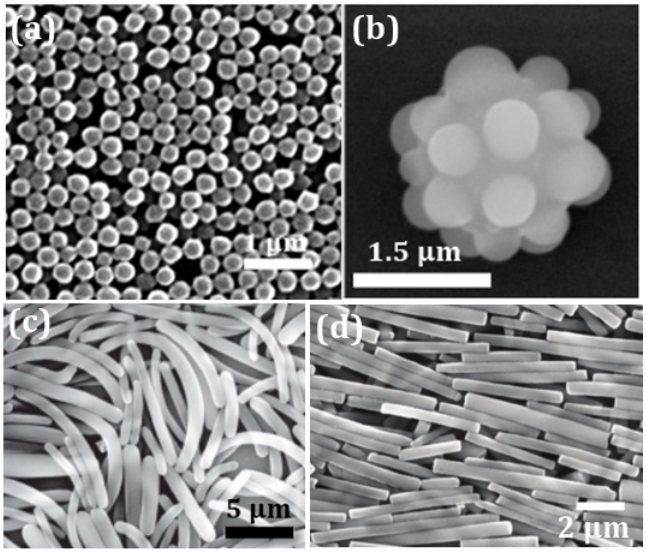


Figure 1.1: Scanning electron microscope pictures of various examples of colloids. (a) Polymethylmethacrylate spheres, (b) A 3-trimethoxysilyl propyl methacrylate raspberry [14], (c) SU-8 photoresist bananas [15] and (d) SU-8 photoresist rods [16].

1.2 Colloidal systems

Colloids are objects with a size between 10 nm to 10 μm [11]. They are found in nature, like red blood cells or fat in milk, but can also be synthesised in the lab. As suggested by these examples, colloidal particles are found in solutions, which we then call *colloidal suspensions*, and come in different shapes. From spheres to rods, to more exotic shapes like raspberries or bananas, synthetic colloids offer a great range in terms of particle shape, material and size, see Figure 1.1, [12–15]. In a solution, a colloidal particle is much bigger than the molecules of the solvent it is suspended in. Those molecules exhibit thermal motion and bump into the colloidal particle randomly through time. On average, these collisions do not move the colloidal particle. However, in any instant of time, the colloid being small enough, it moves in the solution in the direction given by the sum of all the momenta transferred by the surrounding solvent molecules [17]. As a consequence, colloids undergo Brownian motion, similarly to atoms and molecules, thereby scanning phase space in a similar way. As a result, colloids behave similarly to them, at the statistical mechanics level [17] and show analogous phases: crystal, liquid and gas [18]. Similarly, rod-like colloidal particles behave similarly to molecular liquid crystals and display similar phases: smectic, nematic and isotropic [16, 19].

However, contrary to atoms and molecules, the motion of colloidal particles happen over a timescale of the order of a second [11]. This means that colloidal motion can be observed

experimentally much more easily than for atoms or molecules, for instance through means such as bright or confocal microscopy [16, 20]. In other words, colloids can be experimentally easily tracked in space and time down to the single particle level [16]. In addition to the large timescales and lengthscale of colloids, their interactions can be tuned using chemistry techniques, such as changing the colloids' surfaces or adding salts to modify electrostatic interactions [11, 21]. Colloids are also *soft* in that their Young's modulus is significantly lower than that of atomic systems. As the Young's modulus is an energy per unit volume, for an atomic species it is of the order of $\mathrm{eV/\AA}^3 \sim 1 \times 10^{11}\,\mathrm{Pa}$, whereas for colloidal systems, it is of the order of $k_BT/(\mu m)^3 \sim 1 \times 10^{-3}\,\mathrm{Pa}$. The Young's modulus in colloidal systems is therefore 10^{14} orders of magnitude smaller which means that deforming these colloidal systems is much easier. The softness coupled with tunable surface chemistry as well as easily observable lengthscales and timescales with thermodynamically identical behaviour to atoms and molecule make colloids a powerful model systems for them.

1.3 Colloidal interfaces

Colloidal systems can also be used to observe interfaces. In dense systems, colloids have been used to observe grain boundaries as a model to atomic boundaries between crystallites in alloys [22, 23]. Solid-liquid interfaces have also been observed in spherical colloidal systems in order to better understand the process of nucleation and growth of a crystal [24]. With rod-like colloids, interfaces between the isotropic and nematic phases [16], and between smectic an nematic phases [25] have also been studied.

In more dilute suspensions, the colloidal fluid phase can be lead to phase separate into a *colloidal liquid* and *colloidal gas* phase [26]. This is achieved by mixing non-adsorbing polymers to a solution of colloids and it is due to the depletion interaction [11]: polymer molecules are entropically excluded from a volume around the surface of the colloid, the depletion zone. When two depletion zones overlap, the resulting osmotic imbalance pushes the colloids closer to each other. The higher the concentration of polymer in the solution, the stronger this polymer-mediated attraction is, and the larger the polymer molecules used, the longer the range of the attraction [11]. The interaction between colloids can thus be easily experimentally tuned through the size of the polymer and its concentration.

Fluid-fluid phase separation generally happens either through spinodal decomposition [27, 28] or through nucleation and growth [29]. This applies both for molecular and colloidal liquid-gas systems, for which it has been studied both in apolar solvents [30] and in aqueous solvents [27]. In bulk, as phase separation takes place, the colloidal liquid sediments to the bottom of the container as it is denser, such that at equilibrium, the interface separating the colloidal liquid and the colloidal gas is on average flat [26]. It is characterised by a surface tension γ, in units of a force per unit length or an energy per unit area. As a consequence, an order of magnitude for it can be calculated as $\gamma = k_B T/R_c^2$, where k_B is the Boltzmann constant, T is the temperature and R_c is the size of the colloid [11]. Using a micron for R_c, one obtains a typical order of magnitude of $\gamma \sim 1 \times 10^{-9}\,\mathrm{N/m}$ for a colloidal interface against about $1 \times 10^{-3}\,\mathrm{N/m}$ for molecular systems, hence, the colloidal liquid-gas interfacial tension is often qualified as *ultra-low*. The low surface tension means that thermal fluctuations create corrugations on the interface of the order of the micron, which is observable via optical microscopy techniques such as confocal microscopy [26].

1.4 Manipulating the colloidal liquid-gas interface

Actively deforming a fluid-fluid interface is desirable not only for the insights it brings into interfacial phenomena, but also for application in micro-fluidic devices [31, 32]. It has been realised in molecular systems by using atomic force microscopy probes [33, 34], and even with non contact methods such as using electric fields [35] and optical tweezers [36, 37]. Since their invention in the seventies by Ashkin [38], optical tweezers have been a powerful non destructive and non-contact method used across physics, chemistry and biology to move micrometre sized objects with forces of the order of the piconewton [39–41]. Optical tweezers consist of a tightly focused beam of laser light that is able to attract dielectric colloids with a higher refractive index than that of their surrounding medium [39]. Optical tweezers have been used to move one [39], or to manipulate a group of colloids in order to create a grain boundary loop in a colloidal crystals [23]. On the other hand, lasers have been used to deform molecular liquid-liquid interfaces [36, 37]. Deforming the colloidal liquid-gas interface using optical tweezers, i.e. manipulating a large number (> 100) colloids at once has been done recently [42] with low laser powers, which opens possibilities for further work using this system, which we address in this thesis.

1.5 Scope of the thesis

In this thesis, we use a colloid-polymer mixture to create a colloidal liquid-gas interface which we observe from the kinetics of its formation, to its behaviour under confinement. We also actively manipulate it using optical tweezers by nucleating a droplet of colloidal liquid in the the colloidal gas phase and letting it evaporate.

First, the general methods and basis used throughout the thesis are explained. In particular, the synthesis of the colloids and the preparation of the solution of polymer are detailed before we explain how we characterise the colloidal liquid-gas mixture using a phase diagram. The theory and experimental protocol to measure the interface's properties such as the surface tension are also described. We introduce the theoretical background of laser tweezing, essential to understand how we built our original optical setup used to both locally tweeze the colloid-polymer mixtures and image them on a larger length scale.

Then, the kinetics of phase separation via nucleation and growth are studied. We focus on mixtures with low colloid concentration and observe phase separation through confocal microscopy as the polymer concentration is increased. We measure the growth laws of the colloidal liquid domains as a function of time and study the structure they form as phase separation happens. The motion of the liquid domains is also investigated.

In chapter 4, the colloid-polymer mixtures are confined between two plates. This entails a change in geometry where the colloidal gas forms bubbles surrounded by colloidal liquid. The interface of this quasi-2D system is therefore circular. For bubbles of small radii, we examine the modes of the thermal capillary waves in real space and Fourier space to measure the line tension associated with the interface. Bubbles of larger radii require more time for their modes to fully relax and for the line tension to be measured. The dispersion relation of these waves is measured and compared to theoretical predictions.

Next, we our custom-built optical setup, which consists of a fluorescence microscope with optical tweezers to nucleate a droplet of colloidal liquid in the colloidal gas phase. The kinetics of nucleation and final size of the droplet are studied as a function of increasing laser power and increasing distance above the colloidal liquid-gas interface.

Finally, we switch the laser off and observe the evaporation of the colloidal liquid droplets.

This is done across a range of laser power and heights above the colloidal liquid-gas interface. The spatial and time evolution of the fluorescence intensity allow us to measure a diffusion coefficient for the colloids in the gas phase, provided that they are sufficiently far above colloidal liquid-gas interface to not interact with it.

Chapter 2

Background and experimental methods

Abstract

In this chapter, the theoretical background and experimental methods common to all the thesis are introduced. Colloids and colloid-polymer mixtures are defined, as well as the background to confocal microscopy and optical tweezing. Then, the protocols followed to synthesise the colloids and prepare the solutions of polymer are described, before an experimental phase diagram is presented. Next, the experimental measurement of the surface tension of a colloidal liquid-gas interface is described. Finally, the home built optical setup used to image and tweeze the colloid-polymer mixtures is presented.

2.1 Colloidal systems

2.1.1 Definition, time and lengthscales

Colloids are objects with a size between 10 nm to 10 μm. They are found in nature, like red blood cells or fat in milk, but can also be synthesised like in commercial paint. As suggested by these examples, colloids are found in solutions and come in different shapes. From spheres to rods, to more exotic shapes like raspberries or bananas, synthesised colloids offer a great liberty in shape, material and size tunability [12–15].

As they undergo Brownian motion, colloids behave thermodynamically similarly to atoms [17]. In a solution, a colloid is a much bigger particle than the molecules of the solvent it is suspended in. Those molecules experience Brownian motion and bump onto the colloid randomly through time. Of course, on average, these shocks do not move the colloidal particle. However, instantaneously, the colloid being small enough, it moves in the solution in the direction that is the given by the sum of all the momenta transferred by the surrounding solvent molecules [17]. Due to their behaving similarly to molecular systems, colloids show analogous phases: crystal, liquid and gas [18].

However, colloids are much larger and also much slower than molecules or atoms. The typical time scales of their diffusion is called the Brownian time τ_B and it is the time that it takes for a colloid to explore a region of space as big as its surface (in 2D) or volume (in 3D). In other words, in 2D,

$$\tau_B = \frac{R_c^2}{4D}, \tag{2.1}$$

where R_c is the radius of a spherical colloid and D is the diffusion coefficient of the colloid in solution. Einstein's formula [43] gives $D = k_B T/6\pi\eta R_c$ for a spherical colloid, with k_B the Boltzmann constant, T the temperature and η the viscosity of the solvent, which yields

$$\tau_B = \frac{6\pi\eta R_c^3}{4k_B T} = \frac{6 \times 1.10^{-3} \times (1.10^{-7})^{-3}}{4 \times 1.38.10^{-23} \times 298} \simeq 1\,\text{s}, \tag{2.2}$$

Where we chose $R_c = 100\,\text{nm}$ and $\eta = 1\,\text{mPa}\cdot\text{s}$, the viscosity of water. This means that the typical time scale for colloids is of the order of the second, and combined with their much larger length scales (compared with atoms and molecules), colloids are observable through much simpler

techniques than atoms and molecules, for example with optical microscopy. As a consequence, colloids make for powerful model systems to study the thermodynamics and statistical mechanics of atoms and molecules.

To characterise the motion of colloids, the Mean Square Displacement (MSD) $\langle \mathbf{r}^2(\Delta t) \rangle$ can be computed, where $\mathbf{r}$ is the displacement of the colloid over a time Δt and the angular brackets denote the ensemble average over all the realisations of the motion of the colloids. In a purely diffusive situation, colloids move only because of random thermal fluctuations such that the colloid's track $(x_C(t), y_C(t))$ follows a random walk. In that case, the average displacement of the colloid is zero, as it moves with equal probability in every direction of space. As a consequence, to measure the displacement of colloids, one calculates the MSD:

$$\mathrm{MSD}(\Delta t) = \langle (x_C(t_0 + \Delta t) - x_C(t_0))^2 + (y_C(t_0 + \Delta t) - y_C(t_0))^2 \rangle_{t_0} \tag{2.3}$$

Note that this formula is given here in 2D but the same reasoning applies in 3D. Einstein [43] proved that the MSD can be written as

$$\mathrm{MSD}(t) = 2d\, D\, t, \tag{2.4}$$

where D is the diffusion coefficient, which in 3D and the infinite dilution limit is [43]

$$D = \frac{k_B T}{6\pi\eta R_c}, \tag{2.5}$$

where η is the viscosity of the surrounding medium surrounding the colloids. This formula was established for spherical colloids in a suspension and comes from the competition between the thermal energy $k_B T$ working to move the colloids and the viscous drag that they undergo, $6\pi\eta R_c$ working against their motion. So, in the case where a colloid's motion is only driven by thermal fluctuations, the MSD is linear with time. If the MSD follows a power law as a function time $\mathrm{MSD} \propto t^\alpha$ with $\alpha < 1$, the motion is called *sub-diffusive*. This happens for instance in very concentrated solutions of colloids where they end up caged by their neighbours [44]. If on the contrary $\alpha > 1$, the motion of the colloids is *super-diffusive*. In a situation where a flow at velocity v is dominating the particles' motion, $\mathrm{MSD} = v^2 t^2$ for instance.

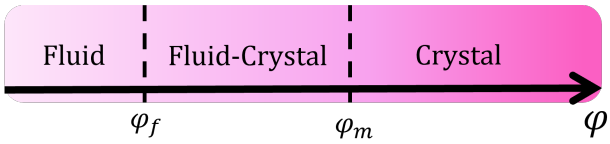


Figure 2.1: Equilibrium phase diagram for a hard-sphere system of colloids. $\phi_f = 0.494$ is the volume fraction where crystallisation starts and $\phi_m = 0.545$ is the melting volume fraction.

2.1.2 Colloidal interactions

The easiest model to characterise the interactions between colloids is the *hard-sphere* model, in which colloids cannot penetrate each other. Their potential of interaction V_{HS} is the one sketched on Figure 2.2 [45] and is given by

$$\begin{cases} V_{HS}(r) = 0 & \text{if} \quad r > R_c \\ V_{HS}(r) = \infty & \text{if} \quad r < R_c \end{cases}, \tag{2.6}$$

where r is the distance separating 2 colloids.

From this potential, the phase behaviour of hard spheres (see Figure 2.1) is indeed analogous to molecular systems, the difference being that the phases as described as a function of volume fraction instead of temperature [18]. Qualitatively, one behaves like the inverse of the other.

A more refined model of interaction between colloids is the DLVO potential, named after Derjaguin, Landau, Verwey and Overbeek [46,47]. It accounts for van der Waals and electrostatic interactions between the colloids. The first are given by

$$V_{vdW} = -\frac{AR_c}{24r}, \tag{2.7}$$

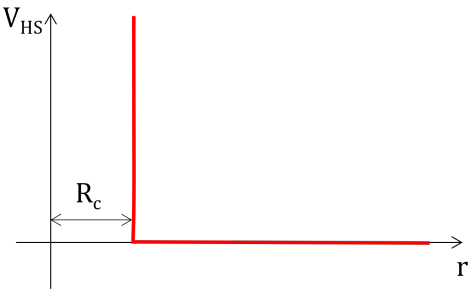


Figure 2.2: Potential of interaction of colloids in the hard-sphere case.

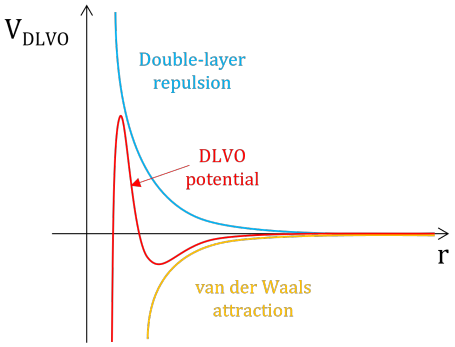


Figure 2.3: The DLVO potential V_{DLVO} and both its contributions: the double-layer repulsion and the van der Waals attraction.

with A the Hamaker constant [48]. As the Hamaker constant is positive for colloids made of the same material, van der Waals interactions are attractive. Electrostatic interactions come from electric charges present at the surface of the colloids. In a solution, salts can be added such that the appropriate counter-ions to these charges screen the repulsion. These electrostatic effects decay over a typical lengthscale of l_D, the Debye length. The result of the sum of the van der Waals interactions and the electrostatic ones is the DLVO potential of interaction V_{DLVO} shown on Figure 2.3. Van der Waals forces dominate at short and large distances, with the first minimum at low r often called the *primary minimum*. The other minimum at higher separation distance is referred to as the *secondary minimum*. Double layer interactions dominate at intermediate distances and are responsible for the maximum in the DLVO potential, which is reached at $r \simeq l_D$.

2.2 Colloid-polymer mixtures

From now on, the colloids are spherical and follow hard-sphere interactions.

2.2.1 Depletion interaction

Upon mixing a solution of colloid with non-adsorbing polymer, the colloids interact through the *depletion interaction*. It is an interaction that is in fact mediated by the polymer molecules. This was first described by Asakura and Oosawa [49,50] and then later by Vrij [51]. Polymer molecules cannot get too close to the surface of the colloid as it would be entropically unfavourable. This leaves a region around the colloid's surface called the depletion zone, whose concentration in

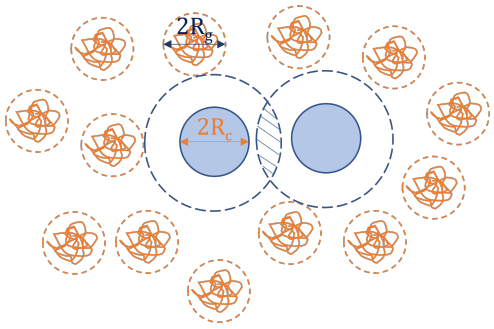


Figure 2.4: Schematics of the depletion interaction. The blue disks are colloids. They are surrounded by a blue dashed line which represents the depletion zone. The orange lines are polymer molecules. They are surrounded by a dashed circular line with radius their radius of gyration R_g. The crossed out blue zone is where the two depletion zones overlap.

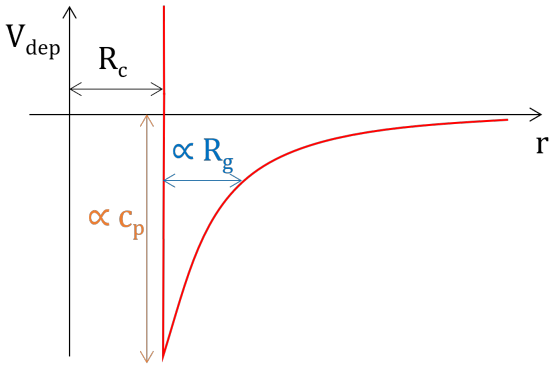


Figure 2.5: Potential due to the depletion interaction V_{dep}.

polymer is lower. When two depletion zones overlap, the resulting osmotic imbalance brings the colloids together, see Figure 2.4. In this thesis however, the polymer is larger than the colloid but the depletion picture still stands. This is due to the polymer's flexibility, which makes it lose internal entropy when getting near the particle's surface.

For colloid-polymer mixtures, three phases can (co-)exist [52]. One where the colloids are attracted to each other and highly concentrated such that they arrange themselves into a crystal, one where they are still fluid-like but close together, and a dilute phase. These are called respectively colloidal *crystal*, *liquid* and *gas* phases as they resemble their molecular counterparts [52]. The addition of polymer changes the potential of interaction of the colloids into the depletion potential V_{dep}, see Figure 2.5. Similarly to the hard sphere potential, there is a hard repulsion for $r < R_c$. Then, there is a minimum whose depth is proportional to the concentration of polymer, and whose range depends on the radius of gyration of the polymer R_g. In other words, the interaction between the colloids is experimentally completely tunable through c_p and R_g.

2.2.2 Phase diagram

The phase diagram is a graph in the (c_p, ϕ_c) plane, where ϕ_c is the volume fraction of colloids. In general, it looks like the schematic on Figure 2.6. On it we find the location of the different

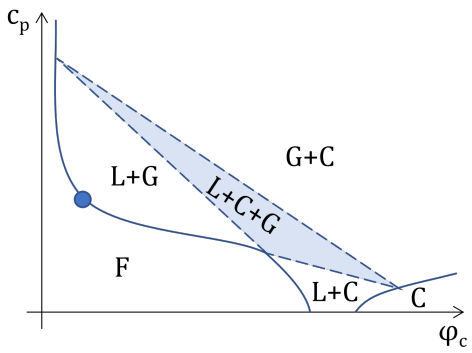


Figure 2.6: Schematics of a phase diagram. C, L and G correspond respectively to crystal, liquid and gas. The blue circle correspond to the critical point and the triangle to the coexistence region for all three phases in the case of an excluded volume polymer [30].

phases and where multiple ones co-exist. We note that for $c_p = 0$ i.e. in the absence of polymer, the phase diagram is identical to the hard-sphere one. Looking vertically along the c_p-axis, the introduction of polymer in the solution widens the coexistence region between fluid and crystal compared with the hard-sphere case.

As the potential of interaction is sensitive to R_g, so is the phase diagram, which is why the ratio R_g/R_c called q is crucial to the study of colloid-polymer mixtures. A higher value of q (i.e. larger polymer) pushes the line between fluid and liquid-gas phases downwards [30], making the liquid-gas region wider. The larger the polymer, the thicker the depletion zone around the colloids and (second consequence) the longer the range of the attraction between the colloids, thus making a liquid phase easier to stabilise. On the contrary, if the q value is low the liquid-gas coexistence region shrinks until it becomes metastable. This happens for q values typically below 1/3 [11].

2.2.3 Interface fluctuations

Aarts *et al.* [26] developed an experimental protocol to measure the surface tension of a colloidal liquid-gas interface. Here, we will introduce the theory of thermal capillary waves. We consider a 2D interface between a 3D colloidal liquid phase and a 3D colloidal gas phase that we study at a mesoscopic level. We thus look at typical lengths much larger than that of a single colloid, without being macroscopic either. The theoretical framework for this has been developed first by Mandelstam (in German) in [53] and later was reviewed by Vrij [54]. We here follow Aarts' derivation [55]. We start from the work W necessary to create a corrugation at constant

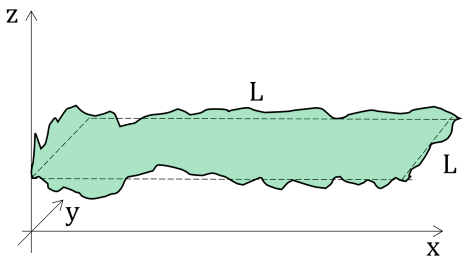


Figure 2.7: Schematics of the interface at a fixed time.

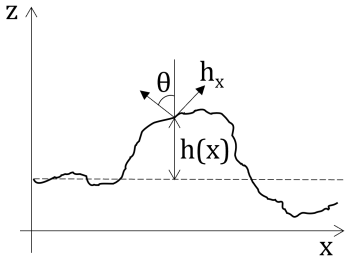


Figure 2.8: Zoomed in schematics of the interface.

temperature, which can be written as

$$W = W_g + W_c, \tag{2.8}$$

where W_g and W_c are respectively the contribution of gravity and capillary forces. The first results from the displacement of the liquid phase against gravity and the second accounts for the fact that while doing so, there is creation of more surface area between the two phases. The local interface position h with respect to its mean position is parametrised by Cartesian coordinates x and y as shown on Figure 2.7. Thermal fluctuations are the only forces contributing to the roughness of the interface. Their amplitude is assumed to be weak enough such that there are no overhangs on the interface.

To create a corrugation of an infinitesimal area $dxdy$ over a distance h gravity contributes

$$\delta W_g = \int_0^h h'\, g\Delta\rho\, dxdy\, dh' = \frac{1}{2}\, g\Delta\rho\, h^2\, dxdy, \tag{2.9}$$

where g is Earth's acceleration and $\Delta\rho$ is the difference in mass density between the two phases. On the other hand, capillary effects contribute such that

$$\delta W_c = \gamma dA = \gamma\, dxdy \left(\sqrt{1+\partial_x h^2+\partial_y h^2} - 1\right) \approx \frac{1}{2}\,\gamma\, dxdy\, \left(\partial_x h^2 + \partial_y h^2\right). \tag{2.10}$$

where $\partial_i h = \partial h/\partial i$ and $i = x, y$. Then we integrate over the total interface area $L \times L$, which gives

$$W_g = \frac{1}{2}\, g\Delta\rho \int\int dxdy\, h^2, \tag{2.11}$$

and

$$W_c = \frac{1}{2}\,\gamma \int\int dxdy\, \left(\partial_x h^2 + \partial_y h^2\right). \tag{2.12}$$

The total work necessary to create a corrugation in the interface is thus

$$W = \frac{1}{2}\, g\Delta\rho \int\int dxdy\, h^2 + \frac{1}{2}\,\gamma \int\int dxdy\, \left(\partial_x h^2 + \partial_y h^2\right). \tag{2.13}$$

The height h can be expanded in a Fourier series in a square with length L (see Figure 2.7) such that

$$h = \sum_{\mathbf{k}} h_{\mathbf{k}}\, e^{i(k_x x + k_y y)}, \tag{2.14}$$

with $h_{\mathbf{k}}$ the Fourier coefficients and $\mathbf{k} = (k_x, k_y)$. The summation is applied over all the Fourier modes k_x and k_y. We now use Parseval's identity to show that

$$W = \frac{1}{2} L^2 \sum_{\mathbf{k}} |h_{\mathbf{k}}|^2 \left(g\Delta\rho + \gamma k^2\right) \tag{2.15}$$

with $k^2 = k_x^2 + k_y^2$ and $k = |\mathbf{k}|$. Mandelstam then used the equipartition theorem to deduce that, given that the work necessary to create each mode is equal to $k_B T/2$, each component $h_{\mathbf{k}}$ of the displacement contributes in average

$$\langle |h_{\mathbf{k}}|^2 \rangle = \frac{k_b T}{\gamma L^2} \frac{1}{k^2 + L_c^{-2}}, \tag{2.16}$$

with $L_c = \sqrt{\gamma / g\Delta\rho}$ the capillary length.

The thermal fluctuations acting on the interface are random. As such, there are statistically no reasons why there would be more positive heights or negative heights; assuming that $h = 0$ is defined at the average. Consequently, the distribution of heights $P(h)$ is described by a Gaussian

$$P(h) = \frac{1}{\sqrt{2\pi\sigma^2}}\, e^{-h^2/2\sigma^2}, \tag{2.17}$$

where σ is its variance. We can obtain its expression from 2.16 and applying Parseval's theorem and we find

$$\langle h^2 \rangle = \frac{k_B T}{4\pi\gamma} \ln\left[\frac{k_{max}^2 + L_c^{-2}}{k_{min}^2 + L_c^{-2}}\right], \tag{2.18}$$

with $k_{min} = 2\pi/L$ and $k_{max} = 2\pi/l_m$. L is the system size and l_m is a microscopic length of the order of the colloid's radius R_c [30].

Experimentally, we can measure the interface properties (namely γ and L_c) through the height-

height correlation function $g(x,t)$, which is defined as

$$g_h(x,t) = \langle h(x',t')h(x+x',t+t')\rangle. \tag{2.19}$$

Here the angular brackets denote average over the primed quantities. We can then decouple the static correlation function $g_h(x) = g_h(x, t = 0)$, and the dynamic one $g_h(t) = g_h(x = 0, t)$. To obtain the expression for the static correlation function, we Fourier transform equation 2.16 as follows

$$g_h(x) = \sum_{\mathbf{k}} \frac{k_B T}{\gamma L^2} \frac{1}{k^2 + L_c^{-2}} e^{i\mathbf{k}\cdot\mathbf{s}} = \frac{k_B T}{\gamma L^2} \frac{L^2}{(2\pi)^2} \int d\mathbf{k} \frac{1}{k^2 + L_c^{-2}} e^{i\mathbf{k}\cdot\mathbf{s}}, \tag{2.20}$$

where we changed the summation into an integration and $\mathbf{s} = (x, y)$. Then, we switch from cartesian coordinates to cylindrical ones and integrate over θ

$$g_h(x) = \frac{k_B T}{\gamma} \frac{1}{(2\pi)^2} \int dk \frac{k}{k^2 + L_c^{-2}} \int_0^{2\pi} d\theta e^{ikx\cos\theta} = \frac{k_B T}{\gamma} \frac{(2\pi)}{(2\pi)^2} \int dk \frac{k}{k^2 + L_c^{-2}} J_0(kx). \tag{2.21}$$

J_0 is the Bessel function of the first kind. In the last integral, the boundaries are k_{min} to k_{max}. However, since $2\pi/L \approx 0$, we set k_{min} to zero. We also set k_{max} to ∞, which allows to perform the calculation and the static correlation function finally is

$$g_h(x) = \frac{k_B T}{2\pi\gamma} K_0\left(\frac{x}{L_c}\right), \tag{2.22}$$

where K_0 is the modified Bessel function of the second kind. The validity of setting k_{max} to infinity comes from the fact that assuming l_m to be R_c the colloid's diameter, $k_{max} L_c \approx 60$ (with $L_c \approx 1\mu m$). Aarts shows that the approximation is valid until the distance x is such that $x/L_c < 0.05$ [55]. Note that the static correlation function g_h contains the surface tension γ in the prefactor and the capillary length L_c inside the argument for the Bessel function, such that we can access both these parameters independently. Moreover, as $L_c = \sqrt{\frac{\gamma}{g\Delta\rho}}$, we can deduce the difference in mass density from that measurement too.

As for the dynamic correlation function, theory predicts modes that decay following $\exp(-t(\gamma k + g\Delta\rho/k)/2\eta)$ with η defined as the sum of the viscosity of the liquid phase and that of the gas phase [30]. Taking equation 2.16, introducing the exponential decay and Fourier transforming

back, we obtain

$$g_h(t) = \frac{k_B T}{2\pi\gamma} \int_0^{\bar{k}_{max}} d\bar{k} \frac{\bar{k}}{1+\bar{k}^2} \exp(-(\bar{k}+\bar{k}^{-1})t/2\tau + i\bar{\mathbf{k}}\cdot\mathbf{s}), \tag{2.23}$$

where $\bar{k} = kL_c$ and τ is the capillary time defined by

$$\tau = L_c \frac{\eta}{\gamma}. \tag{2.24}$$

As $g_h(t)$ is defined by $g_h(t) = g_h(x = 0, t)$, the position is fixed such that $\exp(i\bar{\mathbf{k}}\cdot\mathbf{s}) = 1$. Thus

$$g_h(t) = \frac{k_B T}{2\pi\gamma} \int_0^{\bar{k}_{max}} d\bar{k} \frac{\bar{k}}{1+\bar{k}^2} \exp(-(\bar{k}+\bar{k}^{-1})t/2\tau). \tag{2.25}$$

This expression is also equal to [42]

$$g_h(t) = \frac{k_B T}{2\pi\gamma} K_0\left(\frac{t}{\tau}\right). \tag{2.26}$$

Similarly to the static correlation function, the dynamic one $g_h(t)$ contains the surface tension in the prefactor. This time however, it is the capillary time that is in the argument of the Bessel function. So by measuring experimentally the correlation functions, we can measure the surface tension associated with the interface γ, and the capillary length L_c from which we can deduce the difference in mass density $\Delta\rho$; we can also access the capillary time τ.

2.3 Confocal microscopy and optical tweezing

2.3.1 Confocal microscopy

Confocal microscopy is an optical microscopy technique to probe micron-sized objects. It is thus convenient and relevant for the study of colloids. What confocal microscopy offers more than its bright field or fluorescence counterparts is the ability to resolve objects not only in the $(x, y)-$plane but also in depth, allowing for $z-$scans and reconstruction of a volume instead of a slice. This is achieved using fluorescently labelled colloids as well as a pinhole right in front of the photo-detector, which will filter out any light not coming from the focal plane.

The schematics of the main structure of a confocal microscope is shown Figure 2.9. In

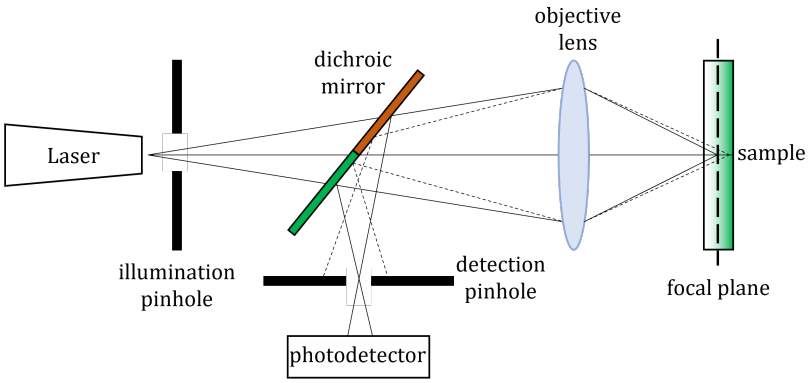


Figure 2.9: Conceptual schematic of a confocal microscope. The straight line represent the rays in the $z-$focal plane whereas the dotted lines are rays coming from another $z-$position. Those rays are filtered out by the detection pinhole and that signal is excluded, leaving only that which comes from one $z-$position.

practise, we use a dye which is excited by 543 nm laser light. This light goes through an illumination pinhole and via a dichroic mirror. It lets the illumination light through such that it is focused by the objective, which on Figure 2.9 is simplified into a single lens, onto the sample. The fluorophores in the colloids re-emit light at a higher wavelength, and the dichroic mirror reflects it towards a detection pinhole. If the light comes from the focal plane of the objective lens, then it passes through the detection pinhole and is collected by the photodetector. If however it comes from a plane at a higher or lower z, then the light is blocked by that pinhole. As a result, only the light coming from one the focal plane is collected. We can then move the objective lens with the piezoelectric mount and probe different $z-$planes, which allows us to explore a volume of solution instead of a slice of it or the superposition of multiple $z-$planes, as one would get in bright field or fluorescence microscopy.

2.3.2 Optical tweezing

Optical tweezing consists in manipulating micrometre-sized or smaller dielectric object using a tightly focused laser beam. It was originally developed and first experimentally put into place by Arthur Ashkin in 1986 [38, 39] and has been widely used since, with applications in biology to study the folding and unfolding of proteins for example or in colloid science [23, 40, 56]. It was originally called *single-beam gradient force trap*. The effect of tightly focused light on an object can be understood through three different theoretical frameworks depending on the ratio between the size of the object, R, and the wavelength of light, λ:

- If $R >> \lambda$, then the interaction of light and the object is best modelled by ray optics.
- If on the contrary $R << \lambda$, then the dielectric dipole approximation is the best model.
- If $R \simeq \lambda$, then one has to use Mie theory.

All these approaches yield similar qualitative results as regards the way the colloids behave when hit by light. Here, our colloids have a radius of $R_c = 100\,\text{nm}$ whilst we use a infrared laser with $\lambda = 1064\,\text{nm}$. This situation is the closest to the dielectric dipole approximation. For better clarity, we choose to explain the phenomenology through the ray optics approach.

Generally, the effect of tightly focused light on an object can be decomposed into two forces: the gradient force and the scattering force. The latter is also called *radiation pressure* and results from the linear momentum transfer from the photons to the particle. In other words, one can effectively picture the object being bombarded by photons. With each collision, the linear momentum of light is transferred to the object resulting in a displacement of the object in the direction of the propagation of light. This explanation is very similar to the concept of kinetic pressure, hence the name.

To understand the gradient force $\overrightarrow{F_G}$, we consider a dielectric particle with a refractive index higher than its surrounding medium, near the waist of a beam of highly focused laser light. The direction of propagation of the light is $\overrightarrow{u_z}$, see Figure 2.10. As shown on the left schematics Figure 2.10, a ray of light hitting the particle will be refracted twice: once as it enters the dielectric particle and once as it exits it. The light from that beam thus transfers its linear momentum to the particle and the force acting on the colloid is in the opposite direction to conserve momentum. For a colloid out of the optical axis, the ray which hits the colloid the closest to the optical axis transfers the most momentum. Thus, on Figure 2.10, $F_1 < F_2$ and the total force $\overrightarrow{F_G} = \overrightarrow{F_1} + \overrightarrow{F_2}$ is oriented towards the centre of the beam. If the particle is on the optical axis however (see right schematic on Figure 2.10), $F_1 = F_2$ and the resulting force $\overrightarrow{F_G}$ is along the optical axis. This result is key as it shows that a colloid placed in a beam of tightly focused light feels a force that pulls it towards the region of highest intensity, hence the original name, *single-beam gradient force trap*.

With the schematics of Figure 2.10, $\overrightarrow{F_G}$ points towards to the point of focus of the light, O. However, the scattering forces $\overrightarrow{F_S}$ act along the direction of the propagation of light $\overrightarrow{u_z}$ such that in reality the colloid ends up trapped on the optical axis and beyond O. In a lot of

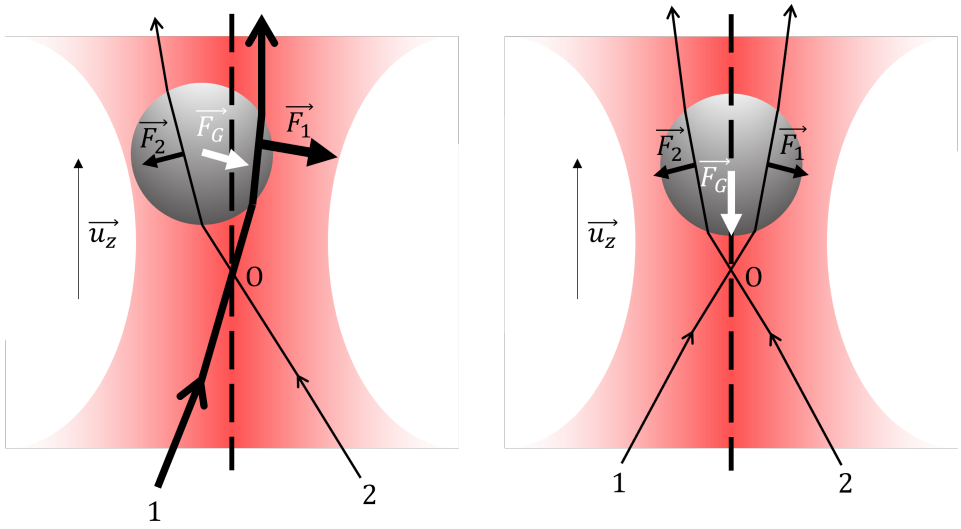


Figure 2.10: Left: colloid interacting with a beam of tightly focused laser light out of the optical axis (dashed line). The forces $\overrightarrow{F_1}$ and $\overrightarrow{F_2}$ originate from rays (1) and (2). As (1) hits the colloid closer to the optical axis, it carries a larger momentum, hence the bolder arrow and $\overrightarrow{F_G}$ is oriented towards the optical axis. Right: same scenario with the colloid on the optical axis this time. $\overrightarrow{F_G}$ is then oriented towards the focus of the laser beam, O.

experimental configurations, this issue is solved by shining the laser in the opposite direction to that of gravity. The radiation pressure is thus counterbalanced by the colloid's weight.

2.4 Experimental methods

2.4.1 Preparation of the Xanthan solutions

Xanthan is a polysaccharide that is secreted by the bacterium *Xanthomonas*. Its chemical formula consists of five-sugar repeating units that consist of a dimeric β-D-glucose backbone segment with a charged three-sugar side chain attached to every second backbone glucose. It dissolves in water and a small concentration of it results in noticeable changes in the viscosity of aqueous solutions [57], which explains why it is widespread in the food industry, where it is used as a thickener.

We use a batch of 4×10^6 g $\cdot$ mol^{-1} Xanthan powder provided by SKW Biosystems except for Chapter 3 where we use Xanthan of 4.5×10^6 g $\cdot$ mol^{-1} provided by Sigma-Aldrich. In solution, the conformation of Xanthan molecules depends notably on the concentration of electrolytes. It was shown that for salt concentrations below 5 mM, the Xanthan chains are disordered coils

because of the repulsions of the charged chains [58]. On the contrary, Koenderink *et al.* [59] showed that if one uses a 0.1 M NaCl solution, the chains are ordered double-helices. To prepare the Xanthan solution, we follow Koenderink's protocol [59] and dissolve 0.1 g of Xanthan in 50 mL of a 0.1 M NaCl solution in water in order to screen double layer repulsions, and we add 2 mM of sodium azide, which acts as an antimicrobial agent. The solution is heated under continuous magnetic stirring until the temperature reaches 85 °C. From there we leave the heating on for an additional hour and then stop it. We leave the magnetic stirring for an additional 15 hours while the solution cools down.

The result is a transparent solution, more viscous than water. The Xanthan chains obtained this way are semi-flexible and the radius of gyration is of 264 nm [60]. The concentration of this stock solution of Xanthan is defined as follows. The volume of Xanthan is given by the product of the volume of one polymer coil V_{1p} and the number of Xanthan molecules N_p:

$$N_p = \frac{m_{\text{powder}}\, N_A}{\text{MW}} \quad \text{and} \quad V_{1p} = \frac{4}{3}\pi R_g^3, \tag{2.27}$$

where m_{powder} is the mass of Xanthan powder that we dissolve and MW is the molecular weight of the Xanthan. The volume of Xanthan is thus $V = V_{1p} \times N_p$, and we adopt the definition commonly used for the concentration of Xanthan in the stock solution: $c_p^* = V/V_{\text{water}}$. We thus obtain $c_p^* = 24$.

2.4.2 Colloid synthesis

Fluorophore preparation

Before starting the colloid synthesis, we have to prepare the fluorophore Rhodamine AminoStyrene (RAS). To that end, we followed the recipe devised by Bosma *et al.* [61]. In a vial, 0.07 g of Rhodamie B isothiocyanate (RITC) was dissolved in 0.05 g 4-aminostyrene and 10 g ethanol. The mixture was brought under a nitrogen atmosphere and was stirred for a period of 4 days.

Synthesis of the colloids

The colloids we use are made of poly-methylmethacrylate (PMMA), which are stable in water and Xanthan does not adsorb onto them. They are made following a method first described by

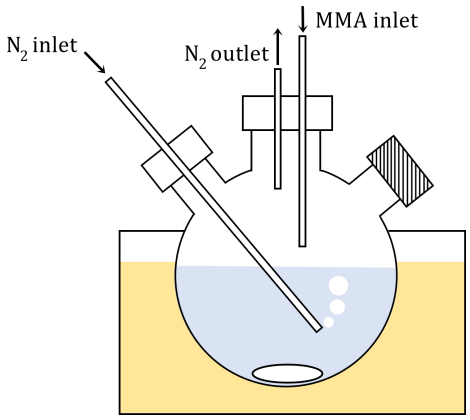


Figure 2.11: Schematics of the PMMA synthesis setup. The three-neck round bottom flask is immersed in an 80 °C oil bath.

Kumacheva *et al.* [12], which is an emulsion polymerisation process. The monomer molecules (here methylmethacrylate, MMA) do not mix with water which results in an emulsion of droplets of it in water. The droplets themselves are not where the polymerisation happens first as explained by Harkins [62]. The seeds/nuclei of PMMA are located in the aqueous phase. The MMA droplets act as reservoirs of monomer that slowly diffuse out to the nuclei and feed them to grow bigger. This is the reason why the monomer has to be added drop-wise, in what is called a *starve-feed* mechanism [62]. The extra monomer *feeds* the already formed nucleus until it stops receiving additional MMA.

Experimentally, we prepare fluorescently-labelled PMMA colloids as follows. In a 250 mL 3-neck round bottom flask that we washed with ethanol and with distilled water thoroughly beforehand, we dissolve 0.4 g of potassium persulfate in 140 mL of distilled water. We close one of the lateral necks with a glass lid whereas the two others are sealed with a rubber stopper. We place one short and one long needle through the stopper in the middle neck, and one long needle on the last neck of the flask, see Figure 2.11. That last one guides the nitrogen in the flask and directly inside the volume of the reagents. The short needle acts as a nitrogen outlet and the second long one to let the MMA in. The flask is placed in an oil bath at 80 °C for about 30 minutes under magnetic stirring at about 350 rpm such that the crystals of potassium persulfate dissolve and the reaction mixture reaches 80 °C. When it does, we pull the inlet of nitrogen above the surface of the aqueous solution before adding 0.5 mL of MMA drop-wise through the long needle in the middle of the flask. We let let it react for half an hour. A blueish halo appears after about 5 minutes, due to the Rayleigh scattering from the droplets of MMA in the water. After half an hour, the solution is very cloudy and almost completely white and opaque.

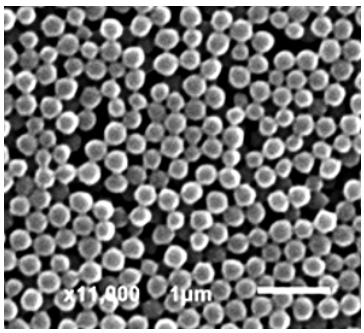


Figure 2.12: Scanning electron microscope image of the PMMA colloids right after synthesis and washing.



Figure 2.13: Final PMMA solution after synthesis and washing.

While the MMA is added drop-wise, we place 0.5 mL of RAS in a glass Petri dish and cover it. By the time the flask reaches the desired temperature, the ethanol will have evaporated, leaving only the RAS powder at the bottom of it. We add 2 mL of MMA to it and mix them while keeping the cover on it all as MMA is very volatile. We then add the mixture drop-wise through the same needle we used to add the undyed MMA. We let the polymerisation continue for an additional 30 minutes.

The colloids now need to be washed to transfer them in a solution of distilled water and to reduce polydispersity. To that end, the solution is poured into 4 centrifuge tubes which undergo centrifugation at 3500 rpm for 90 min. After that, the supernatant is removed and we keep the palet that we transfer into 12 Eppendorf tubes. We finish filling the tubes with distilled water until every one of them contains 1.5 mL of solution. They then undergo centrifugation at 6000 g for 15 minutes at the end of which we remove the supernatant and replace it with fresh distilled water. This washing cycle is repeated 5 times. At the end we perform one last wash at 1000 rpm for half an hour but this time we keep the supernatant and get rid of the small palet that usually contains bigger particles and some of the undissolved dye.

The result of this synthesis is spherical colloids of fluorescently-labelled PMMA of a radius $R_c = 100\,\text{nm}$, see Figure 2.12. In Figure 2.13, one can clearly notice the iridescence on the surface of the glass, which is due to Bragg reflections of the colloidal crystal that has formed, characteristic of a monodisperse solution of colloids which size is around the wavelength of visible light. The volume fraction of the PMMA in the stock solution is measured through its mass fraction and will be referred to as ϕ_c^*. For all the batches, ϕ_c^* is about 0.20.



Figure 2.14: Vial containing a mixture of colloid and polymer, 1 hour after mixing them together. We can see the sharp interface between the colloidal gas (light pink) and the colloidal liquid (deeper pink).

2.4.3 Experimental phase diagram

The experimental polymer concentration and colloid volume fraction are defined as

$$\phi_c = \frac{m_c}{m_c + m_p + m_{sol}} \phi_c^* \quad \text{and} \quad c_p = \frac{m_p}{m_c + m_p + m_{sol}} c_p^*, \tag{2.28}$$

where ϕ_c^* and c_p^* are the stock volume fraction of colloids and concentration of Xanthan respectively, m_c and m_p are the masses that we weigh out of those stock solutions. m_{sol} is the mass of additional 0.1 M NaCl solution in water that we use to dilute a statepoint.

In this thesis we focus on the liquid-gas co-existence region. To find it, we need to locate the binodal line which separates that region from the fluid phase. Experimentally, we prepare multiple vials which each contain a certain amount of stock solution of PMMA and a certain amount of stock solution of Xanthan. We then mix the solution and wait for one hour. After that, we visually inspect the vial. Some samples show two macroscopic phases with a clear, sharp interface in between, see Figure 2.14. Samples like these do phase separate, which means that they are located above the binodal line on the phase diagram. Then, we dilute the solution by adding a known volume of 0.1 M of NaCl in water. This is done to make sure that the Xanthan maintains its double helix conformation. We wait another hour and again, on visual inspection, if the sample shows two phases as it does in Figure 2.14, we continue diluting the sample. Once the sample shows one phase, then the mixture does not phase separate, which means that we crossed the binodal line in the phase diagram.

In the end, the experimental phase diagram is given in Figure 2.15. With the PMMA colloids we have synthesised and the Xanthan solutions we have prepared, the q value is 2.6, which is considered a high value, thus putting the mixture in the protein-limit.

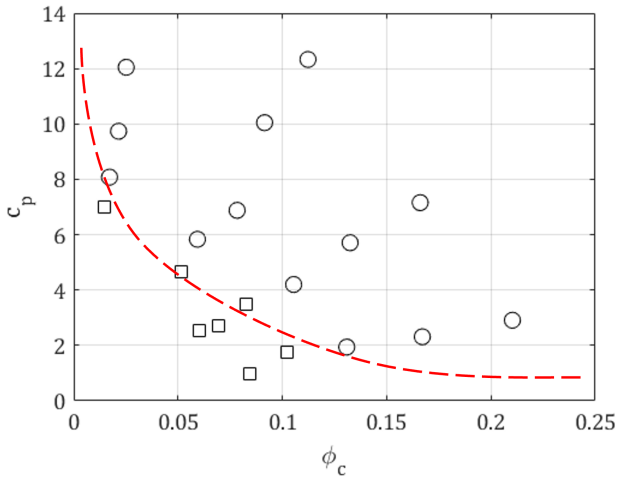


Figure 2.15: Experimental phase diagram. The circles represent mixtures which phase separated into liquid and gas while the square are fluid phase statepoints. The red dashed line is an approximate position of where the binodal line sits.

Locating the binodal line by successive dilutions is quick and does not consume a lot of the stock solutions. However, one has to bear in mind that the phase diagram thus obtained has some error. The first one is of course on the weighing of the different quantities of colloid and polymer stock solutions. Another more subtle one comes from the fact that for solutions close to the binodal, visual inspection becomes more and more difficult as the interface becomes more blurry. Moreover, the binodal line is not located at the same place on the phase diagram if a different batch of Xanthan or PMMA is used. So for each new batch, this exercise has to be done again.

2.4.4 Experimental interface fluctuations

Experimentally, we follow the protocol developed by Aarts *et al.* [26] to measure γ and we here give the details about the procedure for a statepoint with a volume fraction of colloid of $\phi_c = 0.047$ and a concentration of polymer of $c_p = 1.9$. We prepare a mixture in a sample cell that is big enough for macroscopic phase separation to take place, but also thin enough that we can image the interface using a confocal microscope. We used two types of sample cells. The first is a vial cut in an "L" shape, the second is the tip of a pipette tip stuck on a coverslip (see Figure 2.16). They are left overnight for phase separation to reach equilibrium on either of the confocal microscopes we use, either a Zeiss Exciter LSM 5 laser scanning confocal microscope with 543 nm laser source or a 12 kHz resonant scanner head (Thorlabs) and a 532 nm laser, coupled to an

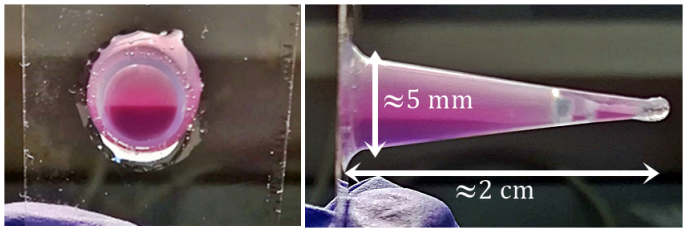


Figure 2.16: One of the types of sample cells through which we observe the thermal capillary waves. The tip of a pipette tip is stuck on a coverslip using UV glue. The cell is then filled using a syringe and needle before it is shut with a bit of epoxy glue. Left: Face through which the observation takes place. Right: Side view.

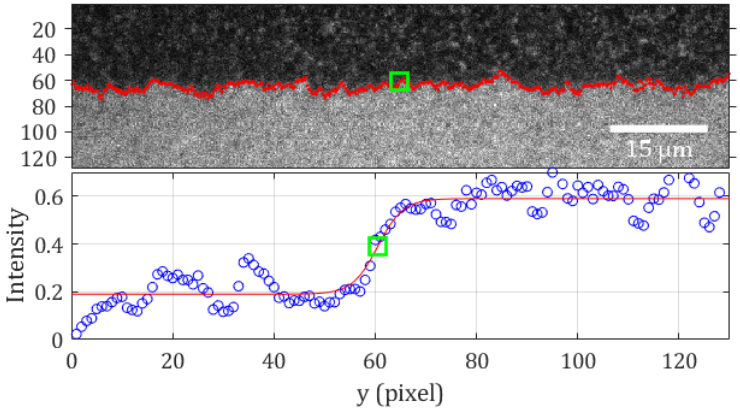


Figure 2.17: Top: Image of the interface taken on the confocal microscope, the red dots are the location of the interface as a function of $x-$position. Bottom: Intensity as a function of y for $x = 256$ pixel. The blue circles are the data and the red line is the hyperbolic tangent fit. The green square is on the inflexion point of the fit, which is defined as the position of the interface for that $x-$position. We also indicate that position on the top picture.

Olympus IX73 inverted microscope equipped with a $60\times$ (NA $= 1.42$) oil immersion objective (Olympus). The microscope is tilted such that the imaging is perpendicular to gravity. Then, we record 5000 images at 4.5 frames per second, for a total duration of about 20 min.

Next, we track the interface to extract $h(x,t)$ and calculate the spatial and time correlation functions in order to measure the surface tension. A classic way to find the interface is to use the Gibbs dividing surface [63]. However here, given that we only have access to the intensity of fluorescence of the colloids, we resort to another method. To track the interface, each image and analysed column-wise. As seen on the lower graph of Figure 2.17, the intensity of light and so the profile of concentration in colloids follows a hyperbolic tangent function. We thus define the location of the interface at each $x-$position as the inflexion point of the hyperbolic tangent which fits the intensity profile best. A fitting procedure runs through all the images and all the $x-$positions to find $h_{\text{raw}}(x,t)$, see Figure 2.17. This height $h_{\text{raw}}(x,t)$ has to undergo some corrections. The first one comes to adjust for the sample drifting along gravity on the stage,

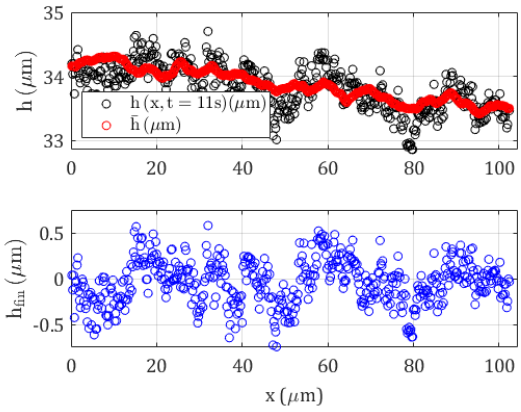


Figure 2.18: Top: Interface at a fixed time (here 11 s). The black circles are the data after the drift correction. The red circles are the average interface $\bar{h}(x)$. Bottom: Same data after removal of the average profile $\bar{h}(x)$.

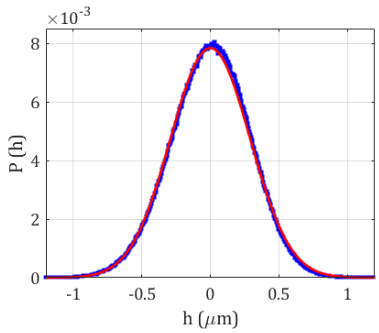


Figure 2.19: Distribution of the heights h. The experimental data is in blue and the Gaussian fit is in red. This fit yields a centre of the Gaussian located at $x = 4 \times 10^{-16}\,\mu$m, which is zero within Matlab's precision, and a variance of $\langle h^2 \rangle = 0.28\,\mu\text{m}^2$.

giving the impression that the interface is rising. This is due to the sample being stuck to the stage with blue-tack. As a consequence, for each value of x, i.e. for each horizontal bin of the image, we fit $h_{\text{raw}}(x,t)$ with a straight line $h_{\text{straight}}(x,t) = \alpha t + \beta$ and correct for the slope:

$$h_{\text{corr}}(x,t) = h_{\text{raw}}(x,t) - \alpha t \tag{2.29}$$

Then, we have account for any structure present in the interface throughout the data set. Ideally, the interface fluctuates around a perfectly flat average profile, i.e. for all $x-$position, $\bar{h}(x) = 0$. However, in practise, $\bar{h}(x)$ is rarely flat. This might come from impurities stuck on the glass like larger chunks of PMMA or Xanthan. To correct for that and obtain the final expression of the height, noted h_{fin}, we substract $\bar{h}(x)$ to $h_{\text{corr}}(x,t)$ for each time t, i.e. $h_{\text{fin}}(x,t) = h_{\text{corr}}(x,t) - \bar{h}(x)$. An example is shown on Figure 2.18.

After these corrections, we check that the distribution of all the positions of the interface through time and space follows a Gaussian law centred around zero [30]. The distributions of final heights, which we call simply h again, is shown on Figure 2.19. The variance of the Gaussian gives an estimate for the typical height of a corrugation $\sqrt{\langle h^2 \rangle} = 0.5\,\mu$m [30].

Now that we have extracted $h(x,t)$ we can calculate both the time and space correlation functions to measure the characteristics of that statepoints: the surface tension γ, the capil-

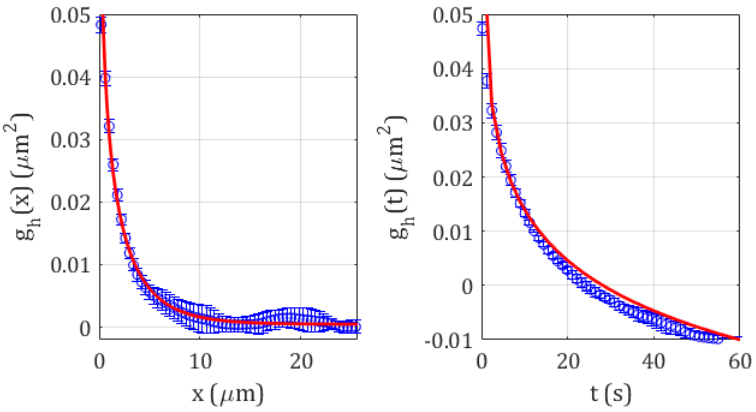


Figure 2.20: Space and time correlation functions $g_h(x)$ and $g_h(t)$. The error bars are given by the standard deviation of the five sets of data. The red lines are the fits using the average coefficients from the five fits. The negative part on the time correlation function does not bear any physical meaning and is introduced by the corrections carried out on the data. For this function we fit the data with the Bessel function and a constant coefficient.

γ	L_c	$\Delta\rho$	τ	γ_t
$33 \pm 2\,\mathrm{nN}$	$3.9 \pm 0.5\,\mu\mathrm{m}$	$220 \pm 55\,\mathrm{kg.m^{-3}}$	$334 \pm 159\,\mathrm{s}$	$48 \pm 2\,\mathrm{nN}$

Table 2.1: Table of results

lary length L_c, the difference in mass density between the liquid and gas phases $\Delta\rho$, and the correlation time τ. The first step is to divide the 5000 frame data set into 5 data sets of 1000 frames each. We analyse each data set independently, and because they are taken on the same statepoint, these will be considered as 5 repeats of the same experiment from which we can estimate the error on the characteristics of the interface. The correlation functions in space and time $g_h(x)$ and $g_h(t)$ are the average of the five correlation functions that we obtain. They are shown on Figure 2.20. We obtain the characteristics summed up in Table 2.1 for this statepoint.

We see that if the space correlation function decays to zero, the time one goes below zero and gives the impression that past a certain time, the interface heights are anti-correlated. This has been observed in this system before [64] and comes from the way the data is corrected. Different corrections can lead the spatial correlation function to go below zero while the time one remains positive. Looking at the table of the results 2.1, one sees a discrepancy between γ and γ_t, which is common for this system. We think that this has to do with the visco-elastic properties of Xanthan which affect the dynamic response of the interface, but more work would have to be done to study this. This justifies thee use of our corrections against those which would make the space correlation function negative. As we suspect that the dynamic behaviour

of the interface is influence by the visco-elastic properties of the Xanthan solution, we would rather have any error on the time correlation function, rather than the space one from which we extract the surface tension.

2.4.5 Optical tweezing setup

We built our own system of optical tweezers coupled with a fluorescence microscope, see Figure 2.21 for a picture of the setup and Figure 2.22 for a schematic. Following the schematic, one can distinguish two sub-systems. Anything from the right hand side of the sample is the tweezing setup, and anything at its left it the fluorescence setup. One is used to tweeze and the other, to image the sample.

Starting from the fluorescence microscope part, a mounted 530 nm LED is used as the source of excitation light. The advantage of this as opposed to a green laser is the absence of structure in the emitted light, meaning that the LED is a source of incoherent light. The price to pay is that the LED is not a monochromatic source, and that it is less powerful than a laser at the same wavelength. But we here use this to our advantage as the dye can in practise be excited by a range of wavelengths. The green light goes through a condenser (C) as the LED emits a wide cone of incoherent light, and is reflected off the dichroic mirror (DM) before it goes through the imaging objective (IO) to arrive collimated on the sample. The fluorescence signal then comes out of the sample and back through the imaging objective (IO). This signal has a larger wavelength than that of the excitation, allowing it to go straight through the dichroic mirror (DM) before it is collimated by the tube lens (TL). It eventually goes through two additional filters, (F_2), a short-pass with cut-off wavelength of 950 nm and (F_1), a long-pass with cut-off wavelength of 650 nm. This is effectively a band pass which rejects any light from the tweezing laser coming through, as well as any remaining green light from the LED, to only let the fluorescence signal through. At the end, the light is collected by a XiMEA colour camera.

Now, for the tweezing part of the setup, the light comes first from the 1064 nm infrared (IR) laser. The beam exiting the laser is expanded through lenses (L_1) and (L_2) such that it overfills the spatial light modulator (SLM) after being reflected by (M_1). The SLM is an optical component which receives one beam of light and outputs either multiple beams or steers the input beam in the $(x, y)-$plane at will. It is essentially a tunable diffraction element. More precisely, it consists of an array of liquid crystals whose orientation is tunable through the application of

a voltage. The key here is that each pixel of the array can be controlled independently, meaning that the orientation of each cell is independent from the rest. Changing the orientation of the liquid crystals changes the refractive index of the medium, which in its turn changes the phase of the reflected light, and thus the optical path length that the light travels. The optical setup was built with the intention to allow for the tweezing of multiple objects at the same time and their driving across the field of view. Such functionalities are not used in this work but definitely give incentive to pursue the research presented in this thesis in those directions. Instead, we here use the SLM for its high reflectivity. One crucial element for the SLM to work is that the light incident on its face should not exceed an angle of about $10\,^{\circ}$. The output light is then shrunk back through lenses (L_3) and (L_4) such that the beam fits the size of the back aperture of the tweezing objective (TO), which focuses it down into the sample. The (F_3) mirror is placed to deflect out the LED light that reflects off the dichroic mirror (DM) and goes through the imaging and tweezing objectives (IO) and (TO), as it can be focused on the face of SLM and potentially damage it.

In the building stages of the setup, the SLM was also used for its ability to correct for spherical aberrations introduced by the different optical elements. To that end, we image the IR laser on the camera (removing the ($F1$) filter that excludes IR light) in the absence of a sample and observe that the spot of light is not circular with diffraction rings. Instead, it tends to be elongated in a certain direction. Through the software that controls the SLM, we correct for this such that the light that is received by the sample is as aberration-free as possible. The advantage of this setup is that the imaging and the tweezing are going through two, different and independent objectives. The imagine objective (IO) is a $60\times$, air objective with a numerical aperture of 0.7. It is equipped with a collar to adjust its working distance from 0.1 to 1.3 mm. On the other hand, the tweezing objective (TO) is a $60\times$ oil objective with a numerical aperture of 1.42. It is however not equipped with a collar so it works at a fixed distance of 0.12 mm. To adjust the z-position of the trap, this objective is fixed on a z-translation mount. This means that, contrary to setups where both the tweezing and the imaging light go through the same objective, here the field of view is not attached to the position of tweezing and can be much larger, while we tweeze our colloid-polymer solutions locally. Moreover, the very different working distances of both objectives means that we can image through the thickness of a microscope slide while we tweeze through a thickness number 1 coverslip (of a thickness in the range of $130\,\mu$m and $170\,\mu$m). The sample is mounted on a stage where we can adjust the

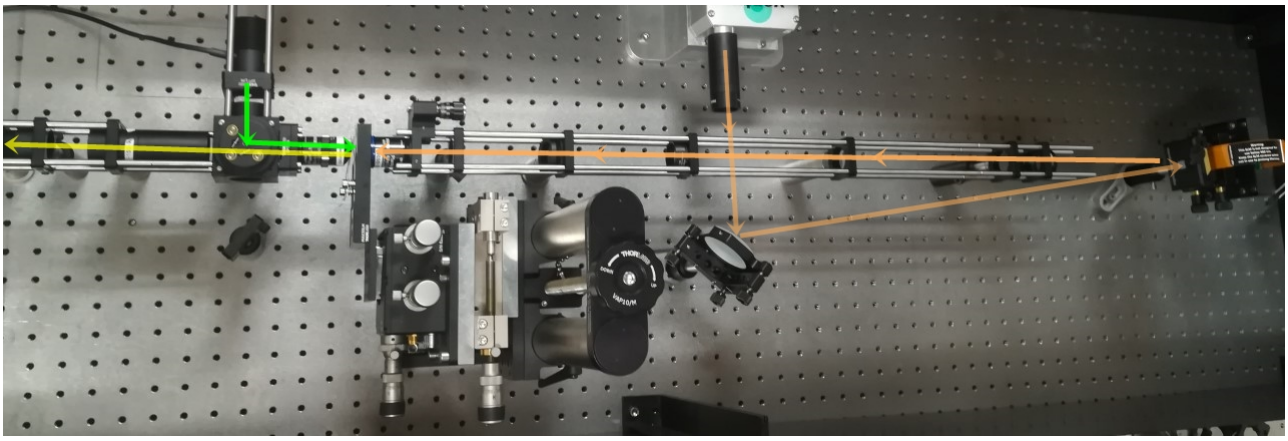


Figure 2.21: Top view of the optical setup. The orange rays are infrared ($\lambda = 1064\,\text{nm}$), the green is the excitation light coming from the green diode and the yellow is the fluorescence signal coming out of the sample.

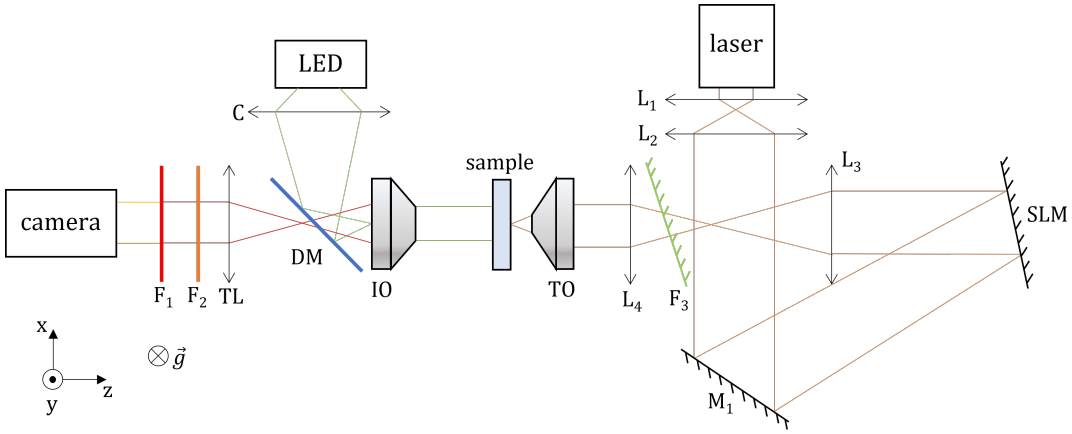


Figure 2.22: Optical setup schematics (top view). The orange rays are infrared (IR) light ($\lambda = 1064\,\text{nm}$), the green is the excitation light coming from the green diode and the yellow is the fluorescence signal coming out of the sample after filtering out the IR light.

position in the three directions of space. It is also worth mentioning that given the geometry of the setup, we are tweezing perpendicularly to gravity, which means that nothing counterbalances the radiation pressure.

Acknowledgments

Arran Curran and Taiki Yanagishima are thanked for practical assistance and useful discussions.

Chapter 3

Dynamics of phase separation via nucleation and growth for a colloid-polymer mixture

Abstract

In this chapter, the evolution of colloidal gas-liquid phase separation in a colloid-polymer mixture through nucleation and growth is studied. Using confocal microscopy, different statepoints are observed and three different mechanisms are found in distinct regions of the phase diagram. One consists in the nucleation of droplets whose growth is arrested; the second is continuous growth without macroscopic phase separation, and the third is growth until macroscopic phase separation. Next, growth laws are computed and compared to theoretical predictions. The structure of the patterns formed as phase separation takes place shows that the size of the Voronoi cells around the liquid droplets correlates linearly with their sizes. Finally, the motion of the growing droplets is found to be different for each mechanism.

3.1 Introduction

The separation of a mixture in two or more phases is a frequent phenomenon in everyday life and a crucial theme in both academia and industry [65]. The easiest example one can think of is when making some salad dressing; upon mixing vinegar and oil, the vinegar does not mix with the oil and forms droplets. In the industrial world, understanding how to formulate an ink that will be absorbed by the paper and "stick" to it is an issue that boils down to mixing and un-mixing components in a mixture [66]. In biology, cells have a lot of compartments, yet not as many membranes. The way that this is managed is that the proteins and enzymes are mixed such that phase separation happens which keeps the different molecules where they belong, without the use of a physical barrier between the different compartments [67].

The biological example and the ink jet printing one are different in that the former relates to liquid/liquid phase separation whereas the latter deals with colloids. Here, we are interested in the colloidal liquid and colloidal gas phases, which are formed upon mixing colloids with a polymer under the right proportions so that the colloids experience an effective attraction to each other due to the depletion interaction (see Chapter 2) [11]. Under the right conditions, this leads to phase separation into a colloidal liquid (rich in colloid, poor in polymer) phase and a colloidal gas (poor in colloid, rich in polymer) phase. Generally, a colloid-polymer mixture can phase separate into a maximum of three phases (gas, liquid and crystal) and a simple examination of the phase diagram suffices to predict which phases will appear after preparing a mixture experimentally. However, the phase diagram does not contain any information regarding the *kinetics* of phase separation, i.e. the mechanisms and pathways taken by a system to reach the equilibrium predicted by the phase diagram. Evans *et al.* [68] reported fifteen different pathways to phase separation into liquid-gas, liquid-crystal, gas-crystal or all three of them; some of which are particularly intricate, with phases appearing and disappearing in order to reach equilibrium.

In general, two mechanisms are observed in phase separating systems. One is *nucleation and growth* and the other is *spinodal decomposition*. They are different and occur at statepoints that are located in specific places in the phase diagram. Statepoints located above the spinodal line (see solid black line in Figure 3.1) are expected to phase separate through spinodal decomposition. The system forms a bicontinous network of liquid and gas phases intertwined. The domains then grow and snap as shown in [30]. Statepoints located between the binodal

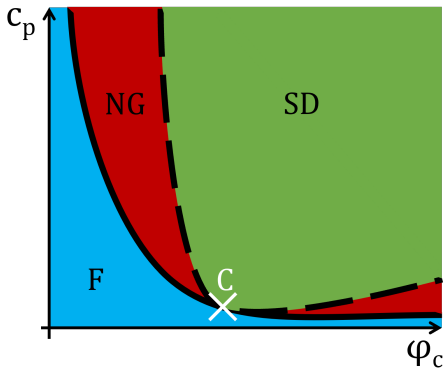


Figure 3.1: Schematic of a phase diagram. The blue region is the fluid phase. The solid black line is the binodal line while the black dotted one is the spinodal line. The red and green regions separate into liquid and gas phases through different mechanisms. NG denotes nucleation and growth while SD denotes spinodal decomposition. Point C is the critical point. Note that this phase diagram is not up to scale.

and spinodal lines phase separate through nucleation and growth (between the solid and dashed black lines on Figure 3.1). A thermal fluctuation creates a droplet larger than a critical size, which continues to grow as the price to pay in surface energy becomes negligible with respect to the gain in volume free energy. For droplets that are too small, the surface free energy is too high and the droplet shrinks. It is the balance between the surface and volume terms which determines whether the droplets grow or not. When they grow to another larger critical size, gravity starts to affect the droplets, which sink to the bottom of the container. Contrary to spinodal decomposition, nucleation and growth has an energy barrier associated with it, and droplets will only nucleate and grow if their sizes are above the critical nucleus size.

Anderson *et al.* [69] found that as phase separation takes place at high polymer concentration, the colloids aggregate and the system *gels*. They observe two different morphologies for the gels formed through two different pathways. The first one is *RLCA*, Reaction-Limited Cluster Aggregation, where the liquid droplets were rather compact and amorphous [70]. In this regime, colloids do not stick immediately to a cluster and the rate-limiting step is to overcome an energy barrier. This means that colloids can still diffuse from one cluster to another. At higher polymer concentration, another regime appears called *DLCA*, Diffusion-Limited Cluster Aggregation, where the liquid droplets become ramified and the colloids stick to liquid droplets without hopping off. All these studies were done for mixtures of colloid and polymer with a low q value (see Chapter 2), i.e. systems with a short-ranged attraction. In contrast, our system has a high q value ($q = 2.6$) and the attraction that the colloids feel is thus longer ranged than

in the systems mentioned previously. As a result, our system exhibits a stable liquid-gas phase separation. In this chapter, we use confocal microscopy to observe phase separation taking place after mixing the PMMA colloids with Xanthan polymer. We study the different pathways taken by the system to phase separate via the nucleation and growth of droplets, their growth laws and the structures they form. The mobility of the droplets is also discussed.

3.2 Theory of the kinetics of phase separation

Theoretical arguments [71,72] and light scattering experiments [70,73] have revealed that growth laws for nucleation and growth show similarities with spinodal decomposition. Given that the spinodal kinetics are less mathematically complicated, we follow Aarts's thesis [30] on the kinetics of spinodal decomposition to provide growth laws. So we start from the the framework of Cahn-Hilliard theory [74–77] for spinodal decomposition. Within this theory, there is a competition between large wavelengths in density fluctuations with low density gradients, which are more thermodynamically favourable, and short wavelengths ones, for which particles only have to diffuse over short distances. As a result one mode q_m grows faster than others and is given by

$$q_m^2 = -\frac{1}{2\kappa}\left(\frac{\partial\mu}{\partial n}\right), \tag{3.1}$$

where μ is the chemical potential, n the number density of particles and κ the square gradient coefficient [74, 75]. From this mode, we can construct the wavelength $L = 2\pi/q_m$ which is a few times the colloid's diameter for a mixture far from the critical point [30]. As time goes by, the system coarsens and L grows in a diffusive way. If we consider the velocity of an object of size L driven by a chemical potential gradient of the order of $\nabla\mu \propto k_BT/L$, we find the growth rate to be given by

$$\frac{dL}{dt} = \frac{-\nabla\mu}{f} \propto \frac{k_BT/L}{\eta L}, \tag{3.2}$$

with f the friction coefficient and η the viscosity. Integrating this equation, one finds

$$L(t) = \left(\frac{k_BT}{\eta}t\right)^{1/3}. \tag{3.3}$$

This is the *diffusive regime*. Then, as sharp interfaces are formed, the surface tension γ starts to play a role and the dynamics are governed by the Navier-Stokes equation

$$\rho D_t \mathbf{u} = \eta \nabla^2 \mathbf{u} - \nabla p - g \Delta\rho \, \mathbf{e_3}. \tag{3.4}$$

In equation 3.4, the left hand side represents the inertial terms with ρ the density, $\mathbf{u}$ the velocity of the liquid phase and D_t the material derivative. Given that the Reynold's number ($Re = \rho L u/\eta$) is small, this term is negligible with respect to the right hand side, which contains respectively the viscous term, the hydrostatic pressure and gravity. The unit vector $\mathbf{e_3}$ points downwards along gravity. For small L, gravity is negligible too and the Navier-Stokes equation is left with viscous terms balancing the pressure p due to the Laplace pressure. Comparing the orders of magnitude involved, one obtains

$$||\eta \nabla^2 \mathbf{u}|| \propto \eta \frac{u}{L^2} \text{ and } ||\nabla p|| \propto \frac{1}{L}\frac{\gamma}{L}, \tag{3.5}$$

which leads to a linear growth of L in this *viscous hydrodynamic regime*, at a velocity of

$$u_c \propto \frac{\gamma}{\eta}. \tag{3.6}$$

We added the subscript c to the velocity as this is the capillary velocity. This regime crosses the previous one (the diffusive one) at a length of

$$L_T \propto \sqrt{\frac{k_B T}{\gamma}}, \tag{3.7}$$

which is known as the thermal length.

The inertial term starts to play a role when the Reynolds number becomes on the order of unity. If we take the capillary velocity as the characteristic velocity in this regime, this happens at a crossover length of

$$L_\eta \propto \frac{\eta^2}{\rho\gamma}. \tag{3.8}$$

Entering the inertial regime, the inertial term in the Navier-Stokes equation 3.4 becomes

$$||\rho D_t \mathbf{u}|| \propto \rho \frac{L}{t^2} \tag{3.9}$$

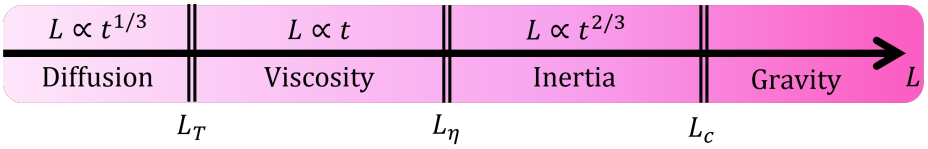


Figure 3.2: Growth laws summarised. The axis is an $L-$axis, above which are the growth laws and below which are the driving force of the growth. The L values listed below the axis are the cross-over lengths at which the system moves from one regime to the other.

and balances the pressure term such that

$$L(t) \propto \left(\frac{\gamma}{\rho}t^2\right)^{1/3}. \tag{3.10}$$

Eventually, the gravity term becomes as important as the Laplace pressure at

$$L \propto \sqrt{\frac{\gamma}{g\Delta\rho}} = L_c, \tag{3.11}$$

which is the capillary length. Past this size, phase separation is driven by gravity. All the growth laws are summarised in Figure 3.2 and we see clearly that each regime is characterised by a distinct power law.

3.3 Experimental methods

3.3.1 Sample cell

We use the top of a blue pipette tip stuck on a coverslip (of thickness between 130 μm and 170 μm) with UV glue (UV NOA 63). The coverslip is thin enough such that observation through the 60$\times$ objective is possible. We filled these cells with a syringe and needle as the blue pipette tips leaves an opening just as wide as the diameter of a needle, before we seal them with a drop of epoxy glue. Finally, we glue four microscope slides on top of the coverslip with epoxy glue such that the bottom of the cell is more rigid. The sample cell is then duct-taped to the microscope stage. A picture of the sample cell is shown on Figure 3.3. This sample cell is wide enough such that the mixture is not confined and small enough that preparing a mixture does not require a lot of PMMA or Xanthan stock solutions. It is also easy to fill and seal, and remains mechanically stable on the microscope stage.

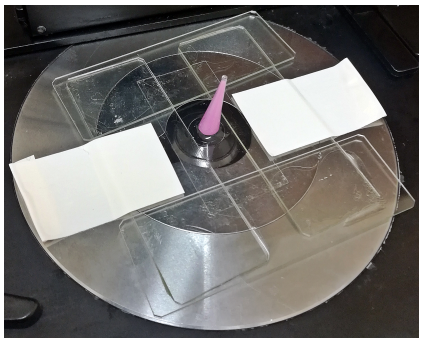


Figure 3.3: Picture of a complete sample cell. It is filled with a PMMA-Xanthan mixture right after mixing and sealing the cell with epoxy glue at the top of the pipette tip.

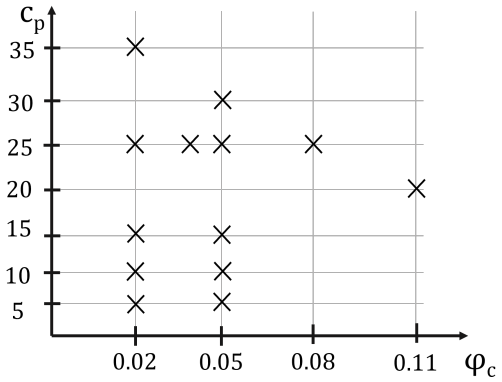


Figure 3.4: Phase diagram of all the statepoints observed.

We prepare different samples each corresponding to a statepoint such that their volume is fixed at 200 μL, all using the same stock solutions of PMMA and Xanthan with $\phi_c^* = 0.21$ and $c_p^* = 37$ (see Chapter 2 for the definitions of ϕ_c^* and c_p^*) . The mixtures are prepared in an Eppendorf tube before being shaken on a vortex for a minute and transferred to the sample cell with a syringe and needle. A phase diagram with all the statepoints observed is shown in Figure 3.4.

3.3.2 Image acquisition

We observe the colloid-polymer mixtures under confocal microscopy using a 12 kHz resonant scanner head (Thorlabs) and a 532 nm laser, coupled to an Olympus IX73 inverted microscope equipped with a 60× (NA = 1.42) oil immersion objective (Olympus). Each experiment lasts for around seventeen hours, unless stated otherwise. We take $z-$stacks of total height 30 μm and step size 0.5 μm. Each $z-$stack takes about 25 s to record and we wait and additional 5 s before taking the next one, such that the duration between two images taken at the same height

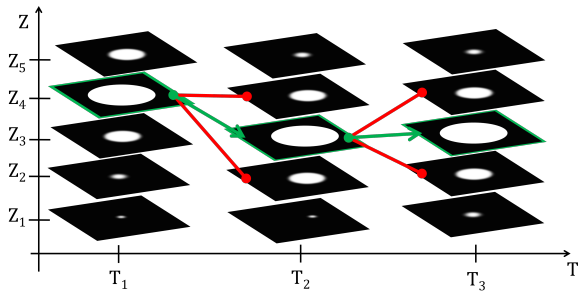


Figure 3.5: Schematic of the method used to find and follow the $z-$plane with the most droplets in focus when the evolution of sample is slow. In stack T_1, the image $I(T_1)$ is found by visual inspection, at $Z = Z_1$. Then, we compute the correlation between $I(T_1)$ and the $z-$images on stack T_2 located between $Z_1 \pm 3$. This corresponds to the arrows between $z-$stacks and it is simplified to only $Z_1 \pm 1$ images for better clarity. The image with the highest correlation is $I(T_2)$ and is highlighted in green here.

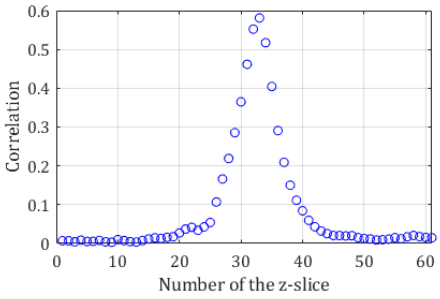


Figure 3.6: Correlation between $I(T_1)$ and all the z-slices for $T = 2$. The graph is shown for all the images in the T_2 $z-$stack for better clarity although in practise we only compute those at slices between $Z_1 - 3$ and $Z_1 + 3$. The maximum correlation is clearly identified here at slice number $Z_2 = 34$.

is 30 s. The pixel size in the (x, y) plane is 200 nm unless stated otherwise.

Next, we want to find and follow the $z-$plane with the most droplets in focus. We observe a slow and monotonic drift in z, which we attribute to the piezo, and over the course of seventeen hours, we find that the sample has typically drifted by a few microns. To identify the images of the time series that we will follow, we use two different methods depending on the speed at which the droplets grow. For statepoints which evolve slowly, we follow the scheme sketched in Figure 3.5. We look at the entire first $z-$stack and visually find the first image $I(T_1)$ (T_i is the index corresponding to the number of the $z-$stack such that $t = i \times 30\,\mathrm{s}$), with height noted Z_1, which has most droplets in focus. To find $I(T_2)$, we compute the correlation between $I(T_1)$ and images in the stack T_2 located between $Z_1 - 3$ and $Z_1 + 3$, see Figure 3.6. $I(T_2)$ is the image with the highest correlation with $I(T_1)$. We then proceed iteratively from image T to image $T + 1$.

For fast changing statepoints, picking the image as that with the highest correlation to the previous one is much less efficient as the changes between one z-stack and the next are much more significant. We pick the first image $I(T_1, Z_1)$ and the last image $I(T_{\mathrm{end}}, Z_{\mathrm{end}})$ as the ones in $z-$stacks T_1 and T_{end} with most droplets in focus. Then, we assume that the drift in z is monotonic and linear between Z_1 and Z_{end}, and we identify the image at index T such that

$$Z_T = Z_1 + \frac{Z_{end}}{\mathrm{end} - 1}(T - 1) + \frac{Z_1}{\mathrm{end} - 1}(\mathrm{end} - T). \tag{3.12}$$

For some statepoints, phase separation happens so quickly that the microscope drift is negligible and we take a time series at fixed z position. We record one image per 2.5 seconds until the liquid phase (or sometimes the gas phase) fills the field of view.

Next, we need to correct for photo-bleaching which makes the image look dimmer as the seventeen hours of the experiment go by. We calculate the average intensity of the first picture of the time series, $\hat{I}(T_1)$ (the hat denotes the average), and we multiply the image taken at index T such that its average is the same as $\hat{I}(T_1)$. In other words, $I(T)_{corr} = I(T) \times \hat{I}(T_1)/\hat{I}(T)$. This operation is performed for all statepoints except for those where the liquid phase invades the field of view as the image becomes brighter and bleaching is not noticeable.

3.4 Results and discussion

3.4.1 Phase diagram

First, we qualitatively characterise the phase separation for the different statepoints studied (see Figure 3.4). We identify four different mechanisms which we term NG-1, NG-2, NG-3 and NG-4. Images of these mechanisms at the beginning and at the end of their evolution are shown in Figure 3.8, along with the times at which they were recorded. The locations of these four mechanisms are indicated in the phase diagram in Figure 3.7. All the statepoints noted NG-i show droplets of liquid phase in the gas phase whereas the one noted F on the phase diagram in Figure 3.7 displays only one fluid phase. NG-1 starts with droplets which grow by sticking to each other, as in NG-2. However, through the NG-1 mechanism, the liquid droplets do not grow as much as the other NG-i mechanisms show, and both the growth and the motion of the liquid droplets are arrested. By contrast, in NG-2, droplets continuously grow and move. The NG-3 mechanism displays growth by coalescence of the liquid droplets until the liquid phase invades the entire field of view. This is the mechanism which leads to macroscopic phase separation. Finally, the NG-4 mechanism is characterised by initial droplets being far less circular than seen through the other mechanisms. This mechanism looks intermediate between nucleation and growth and spinodal decomposition, which is consistent with this mechanism being observed for statepoints being closer to the spinodal line. The non-circular droplets also grow by sticking to each other.

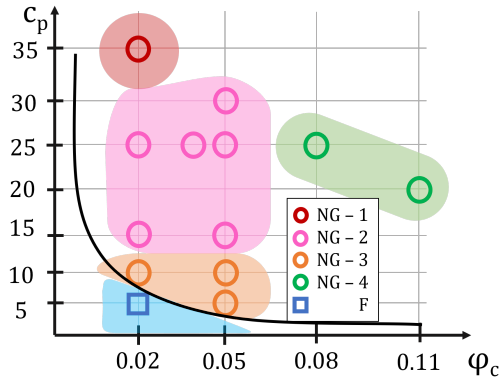


Figure 3.7: Phase diagram of the samples examined in this chapter. The solid black line is the binodal line. It separtes the fluid phase (F) from the rest of the phase diagram were phase separation was observed.

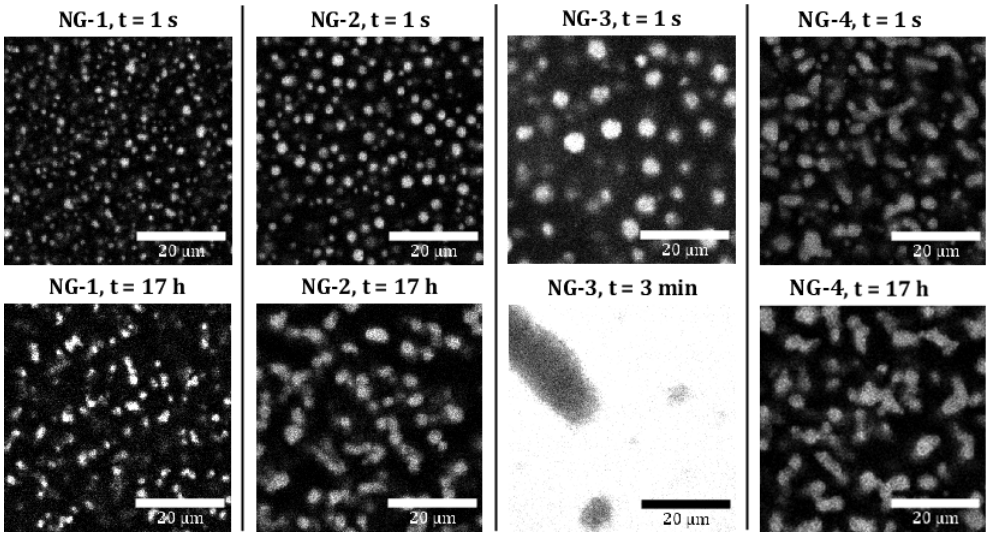


Figure 3.8: Confocal microscopy images taken at the beginning and at the end of the experiments for each mechanism. All the scale bars are identical and measure 20 μm.

We do not observe any event of unsticking and diffusing of droplets to stick somewhere else, making it closer to DLCA in that regard. The one behaviour that we do not observe is the long and thin strings of particles, characteristic of DLCA. This might be because such behaviour takes place at even higher polymer concentrations than what we probed. Moreover, individual colloids are too small to be resolved individually with precision, so events of free colloids diffusing are not visible with our technique.

A macroscopic picture of the NG-1 and NG-2 statepoints a day after the end of the experiments is shown in Figure 3.9. The dark bright pink phase is collapsed at the bottom of the sample cell and when we put the sample cell upside down, it does not flow down. Based on these observations, we conclude that the structure formed is a gel, as a liquid would flow to the

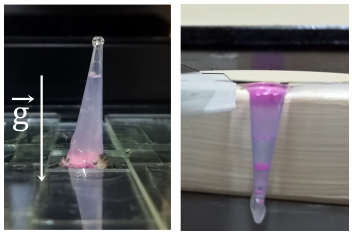


Figure 3.9: Left: NG-2 type statepoint 24 h after finishing the experiment. The bright pink phase used to fill the entire sample cell right after the experiment but a day later, the structure collapsed. Right: Another NG-2 type statepoint a day after finishing an experiment. We put the sample upside down but the structure sticks to the top and does not fall down, hinting at the gel structure inside the sample cell.

bottom. NG-3 however does flow if we tilt the sample cell, showing that the phases are still liquid and gas, even a day after the experiment has finished.

3.4.2 Kinetics of growth

From now on, we focus on the part of the phase diagram where nucleation and growth is the mechanism for phase separation, i.e. we study mechanisms NG-1, NG-2 and NG-3.

The starting time of the experiment is different for every statepoint because depending on how fast the sample forms droplets or liquid droplets, we lose a bit of information at the very early times, between the end of the vortex mixing and the beginning of the acquisition. Now, for NG-1 or NG-2 type statepoints, the dynamics are slow such that starting the imaging a few minutes after mixing does not make much of a difference. However, for NG-3 type statepoints, (and especially the statepoint with $c_p = 5$ and $\phi_c = 0.05$), phase separation happens so fast that those few minutes between preparing the mixture and putting the sample under the microscope are meaningful. We therefore focus on rates or exponents of growth. To locate the liquid droplets, we binarise the image using the average intensity as the binarisation threshold. Then, we identify all the groups of white pixels but remove those under 10 pixels to get rid of the noise. We also exclude the liquid droplets at the edge of the image for which we cannot determine the size.

We now examine the evolution of the number of liquid droplets through time, $N(t)$. The result is shown Figure 3.10. All the statepoints show a number of liquid droplets which decays, confirming the fact that the observation that the droplets either stick to each other in scenarios NG-1 and NG-2, or coalesce for NG-3. However, for NG-1 and NG-2 mechanisms, $N(t)$ does not decay to zero while for NG-3, it does. Statepoints which follow the NG-3 mechanism

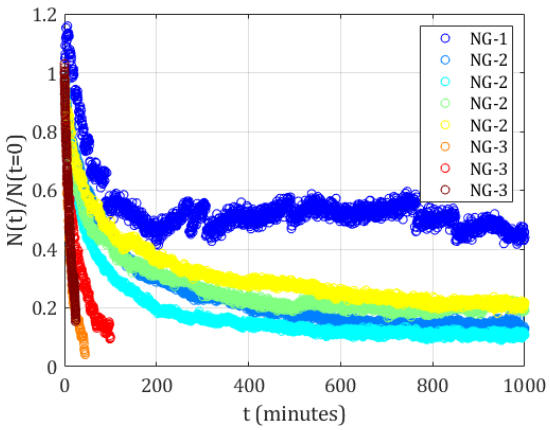


Figure 3.10: Number of droplets as a function of time for all probed statepoints.

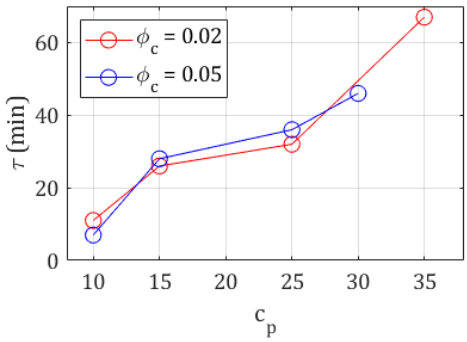


Figure 3.11: Decay time of the n umber of droplets τ as a function of the concentration of polymer c_p for two fixed volume fractions of colloids, $\phi_c = 0.02$ and $\phi_c = 0.05$.

were studied until the number of droplets dropped below 15, which is why in Figure 3.10, the $N(t)/N(0)$ curves do not reach zero exactly. We note that the statepoint corresponding to the red curve phase separates through the NG-3 mechanism, i.e. with liquid phase growing and occupying more of the sample cell, yet at the end of the experiment, a z-stack revealed that the surface was not like a typical liquid-gas interface. Normally, a liquid-gas interface is on average flat with thermal fluctuation provoking corrugations that typically rise to a micron or so [26]. However here, the interface showed wide and static hills and troughs (see Figure 3.12). This is coherent as this statepoint is $(\phi_c = 0.05, c_p = 10)$ and lies close to the NG-2 zone in the phase diagram in Figure 3.7.

Next, we measure a typical decay time τ for $N(t)$ by fitting an exponential decay with an offset in the end, i.e. a function of the form $N(t) = N_0 \exp(-t/\tau) + N_\infty$ and extract τ for statepoints with a colloid volume fraction of $\phi = 0.02$ and $\phi = 0.05$, as a function of polymer concentration c_p. The graph $\tau(c_p)$ is shown in Figure 3.11. We observe that the decay time increases with polymer concentration, but that the volume fraction of colloids hardly affects it. We understand this as the addition of a bit of Xanthan significantly increases the viscosity of a mixture, meaning that the diffusion of liquid droplets is greatly hindered for a small increase of Xanthan concentration. However, the volume fraction of colloid ϕ_c is low for all statepoints studied here, so ϕ_c has very little effect on the variations of τ.

Now, we examine the kinetics of growth of the liquid droplets by tracking their sizes as they grow. We define the size of a droplet, $r_c(t)$, as the square root of the number of white pixels

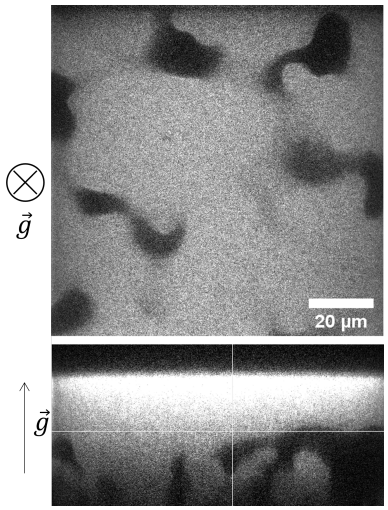


Figure 3.12: Top: Confocal microscopy image of the statepoint at the limit between NG-2 and NG-3 regimes. Bottom: Z-stack of that same statepoint, after the experiment. The surface that separates the bright phase (gel) and the dark phase (gas) has long-lived, wide bumps and troughs, proving that the bright phase is not liquid.

of a contained in one droplet after binarisation. This allows us to measure a size for the liquid droplets regardless of their shapes and even on images where a coalescence event is captured. Figure 3.13 shows the average size of the droplets through time for all the experiments on a linear scale on the left and a log-log scale on the right. The average size of the droplets following the NG-1 mechanism reaches a plateau and the growth is completely arrested. We speculate that as the droplets grow, their sizes reach the pores sizes of the Xanthan matrix which we do not know, at which point the growth is blocked by the elastic modulus of the polymer [78]. In other words, the energy cost to deform the surrounding matrix to accommodate further droplet growth might be too high, hence the arrested growth.

For the NG-2 mechanism, the liquid droplets continuously grow following a power law with an exponent of about 1/2, which is much slower than that of the NG-3 mechanism. It is however faster than the 1/3 expected for diffusion-driven growth (see equation 3.3). These statepoints could experience both diffusion and hydrodynamic effects, such that the colloids form cluster slightly faster than through a purely diffusive process. In the case of the NG-3 mechanism, the size of the droplets increases in time up until it cannot be measured anymore. This is either because the droplets grow larger than the entire field of view or because the z-plane of the imaging is in the gas phase and all the droplets of liquid sink down to merge with the bulk liquid. This increase is also linear with time as shown on the log-log plot on the right, which means that the growth there is driven by viscous hydrodynamic flow (see equation 3.6).

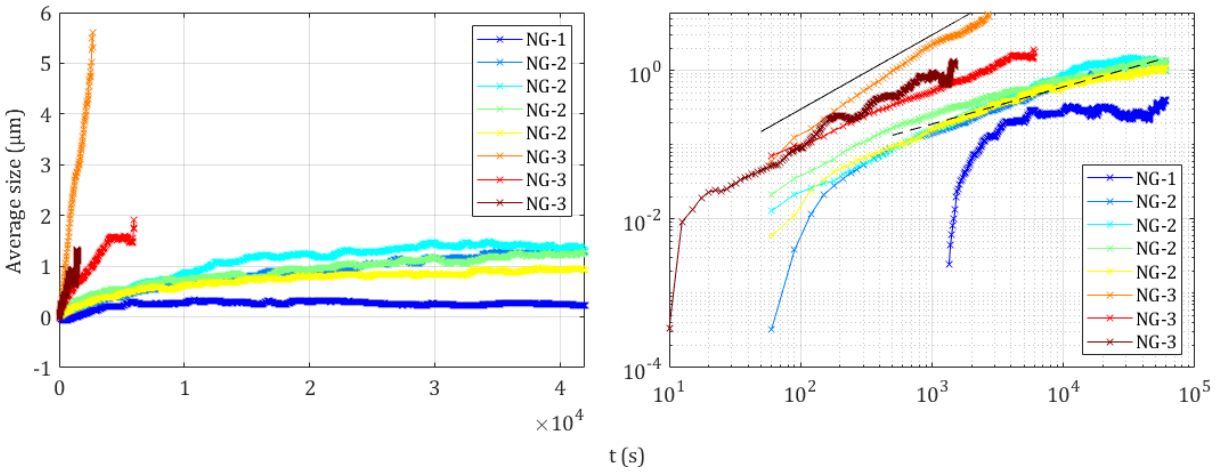


Figure 3.13: Left: Average size of the droplets/liquid droplets as a function of time, corrected to start at zero, i.e. $r_c(t) - r_c(0)$ as a function of time on a natural scale. Right: Average size of the droplets as a function of time on a log-log scale. The solid black line is a power law with an exponent of 1 and the dotted line corresponds to an exponent of 1/2.

3.4.3 Structure

To study the structure that the liquid droplets form as they grow in the different mechanisms, we plot the Delaunay triangulation of their coordinates for each picture. Figure 3.14 shows the first image and last image's Delaunay triangulations for mechanisms NG-1, NG-2 and NG-3. In the case of NG-1, the structure changes only slightly. Moving to NG-2 and then NG-3 (respectively Figure 3.15 and 3.16), the picture changes more and more between the beginning and the end. We also appreciate better here that the first snapshots are different from each other, even though they are always taken only a few minutes after preparing the mixture.

To study the structure changes quantitatively, we plot the square root of the surface area of each Voronoi cell as a function of time, $r_v(t)$, on the left graph, in Figure 3.17. Regardless of the mechanism, the curves all show an increase in r_v meaning that the average spacing between liquid droplets increases as time goes by. As liquid droplets stick together or coalesce, the distance from centre to centre between them increases, hence making r_v increase. This is illustrated in Figure 3.18. Moreover the curves for $r_v(t)$ qualitatively look very similar to the growth of the average size of a cluster as a function of time $r_c(t)$ (see the right graph on Figure 3.13). To compare them, we plot r_v as a function of r_c on the right hand side in Figure 3.17. The correlation is striking, and plotting them on a log-log scale shows that all the data falls on a straight line, regardless of the regime NG-i. This shows that $r_v \propto r_c$, meaning that as liquid droplets grow by sticking to other liquid droplets, or as droplets coalesce with each other, they

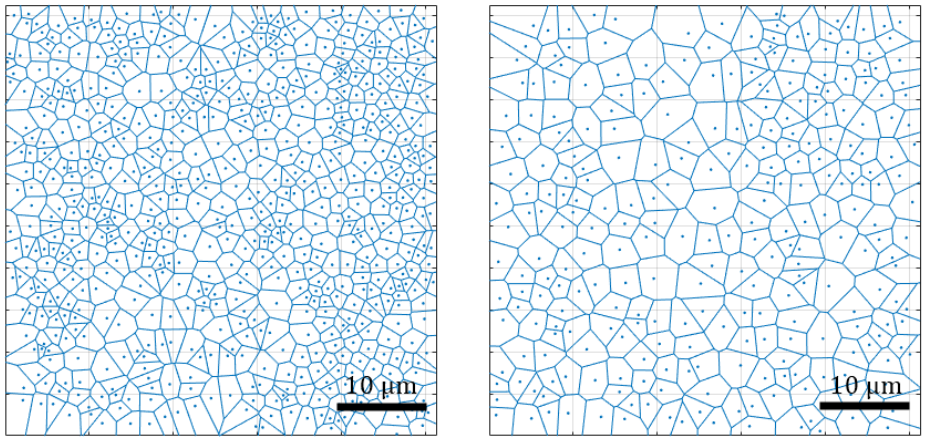


Figure 3.14: Delaunay triangulation of an NG-1 statepoint at $t = 0\,\mathrm{s}$, and $t = 16\,\mathrm{h}$.

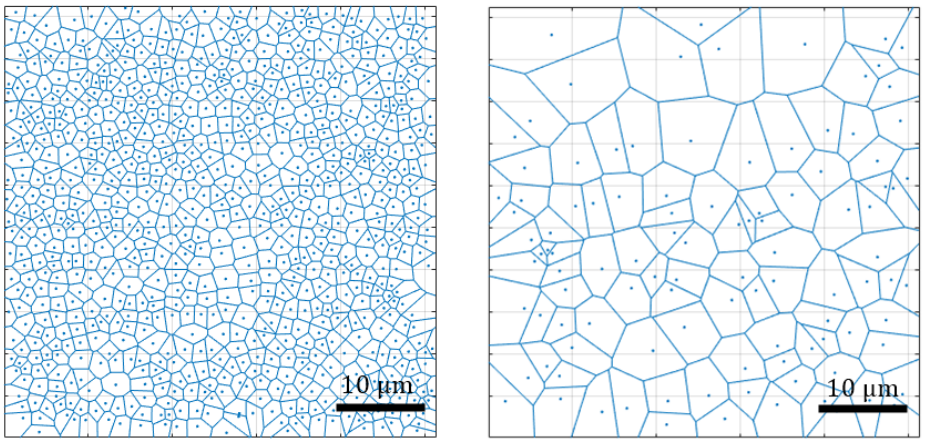


Figure 3.15: Delaunay triangulation of an NG-2 statepoint at $t = 0\,\mathrm{s}$, and $t = 16\,\mathrm{h}$.

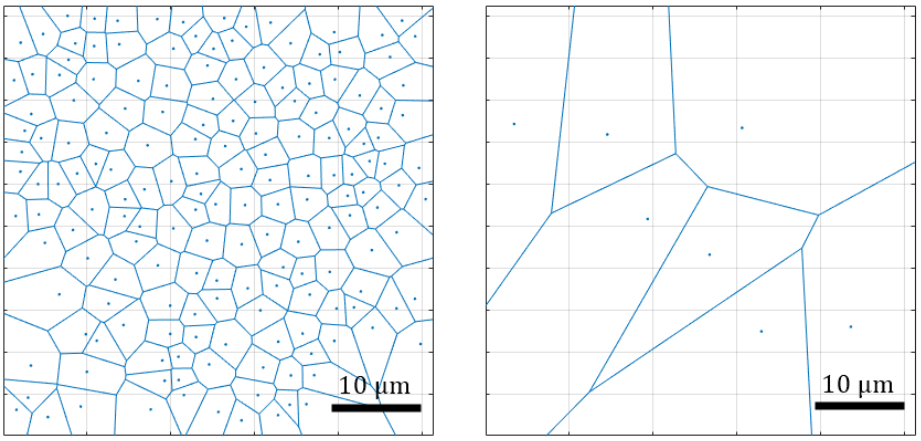


Figure 3.16: Delaunay triangulation of an NG-3 statepoint at $t = 0\,\mathrm{s}$, and $t = 45\,\mathrm{min}$.

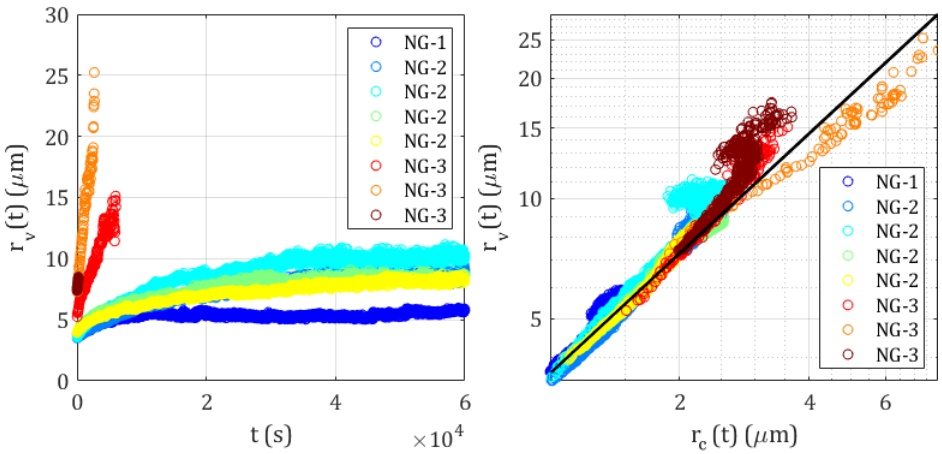


Figure 3.17: Left: average size of a Voronoi cell as a function of time $r_v(t)$. Right: average size of a Voronoi cell r_v as a function of the average size of a droplet r_c . The solid black line has a slope of 1.

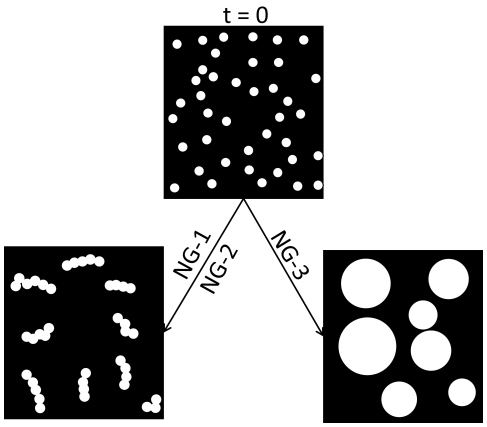


Figure 3.18: The centre-to-centre distance between liquid droplets increase happens for both statepoint forming liquid droplets (NG-1 and NG-2) and those where droplets coalesce (NG-3).

maintain their own *depletion zone* around them. It also means that smaller liquid droplets are surrounded by closer neighbours, whereas larger ones tend to have more space around them. A similar correlation was observed by R. Style *et al.* in [78] for a system of droplets grown in a polymer matrix through nucleation and growth in a liquid-liquid phase separation context. However, for their system, the graph of r_v as a function of r_c is a an cloud of points with a lower correlation than the straight line that we observe. They also showed that the more the positions of the starting nuclei of droplets are correlated, the closer to a straight line the graph of r_v as a function of r_c becomes. They attribute this to long range interactions between nuclei. In our case, where a straight line is observed, the long range interaction between the liquid droplets of colloids might come from the depletion interaction and the high $q-$value of our colloid-polymer system.

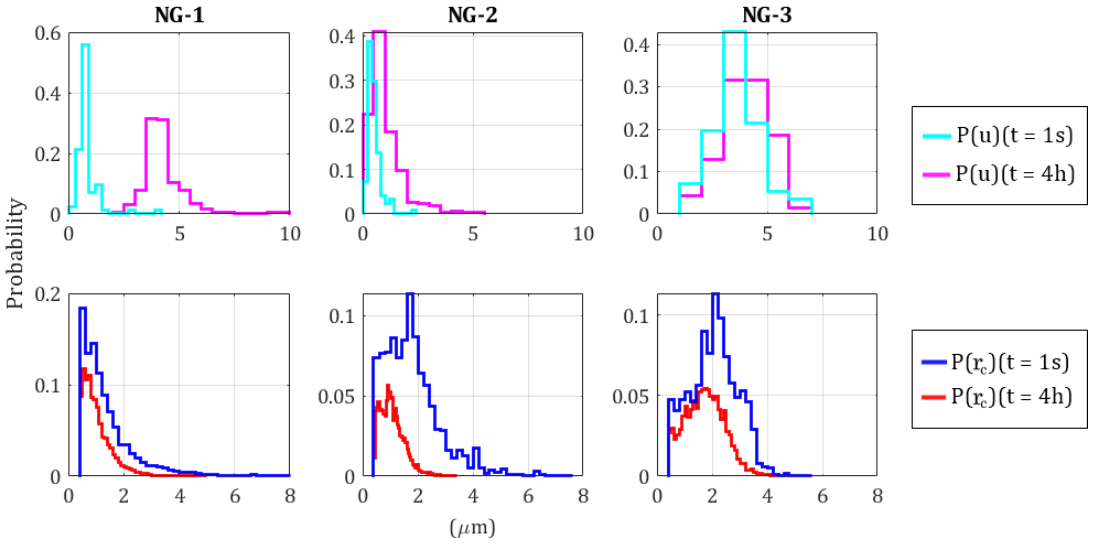


Figure 3.19: Each regime is a column of two graphs. Top line: distribution of displacements $u(t = 0)$ in pink and $u(t = 4\text{h})$ in cyan. Bottom line: distribution of sizes $r_c(t = 0)$ in red and $r_c(t = 4\text{h})$ in blue.

3.4.4 Motion of the droplets

Here, we aim to analyse the motion of the droplets. We have tracked them and know their coordinates as a function of time $(x(t), y(t))$. However, given that their sizes r_c is a function of time, calculating their mean square displacement (see Chapter 2) would not be insightful. Instead, droplet motion is studied through visual inspection of the confocal microscopy images, which indicates that in the NG-1 case, as time goes by, more and more droplets stop moving. We also focus on the distribution of displacements $u(t)$ as a function of time and compare them at $t = 0$ and at $t = 4\text{h}$ during a time Δt of 600 s. In other words,

$$u(t) = \sqrt{(x(t + \Delta t) - x(t))^2 + (y(t + \Delta t) - y(t))^2} \tag{3.13}$$

We compare these distributions in light of the distributions of sizes r_c at those same times i.e. at $t = 0$ and $t = 4\text{h}$, see Figure 3.19. Each column is a mechanism. On the top line are the distributions of displacements and on the bottom line are the distributions of sizes. For mechanism NG-1, $P(u)$ is significantly shifted towards smaller values of displacements, ending with a peak close to zero. This agrees with the observation that as time goes by, more and more droplets stop moving. Looking at the distribution of sizes, the change between $t = 1\,\text{s}$ and $t = 4\,\text{h}$ are very subtle, hinting at the fact that the growth is not very important throughout time. For the NG-2 mechanism, the change in the distributions of displacements shifts slightly

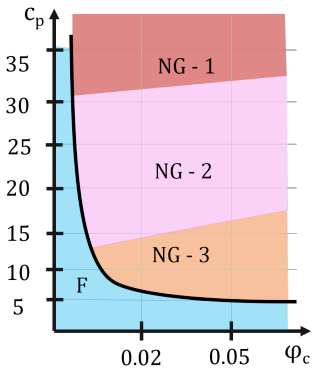


Figure 3.20: Phase diagram and positions of the three regimes NG-1, NG-2 and NG-3.

towards lower values and ends close to zero, while the distribution of sizes widens and shifts towards larger values. This reflects droplet growth. Finally, for NG-3 mechanism, $P(u)$ shifts slightly towards lower values but contrary to the NG-2 mechanism, the peak is far from zero. In addition, the distribution of sizes broadens and widens with a more significant peak. This indicates that the mobility of the droplets is not affected by their growth. We understand that in this case the growth is not purely diffusive as if it were the case, as the droplets grow, they would slow down. Here, flows must play a significant role such that the size of the droplets do not hinder their motion.

3.5 Conclusion and outlook

We have probed the dynamics of phase separation in the nucleation and growth process for a colloid-polymer mixture. We find that there are three kinetic paths, which we term NG-1, NG-2 and NG-3, each of which is observed in a different part of the phase diagram, as summarised in Figure 3.20. NG-1 is a mechanism found at high polymer concentration and characterised by the aggregation of droplets, which slow down until they are frozen, which in turn stops them from growing. We speculate the growth and movement is arrested by the structure of the Xanthan polymer matrix surrounding the droplets of liquid. The NG-2 mechanism is found at lower polymer concentration and displays droplet growth with an exponent of about 1/2 and motion all along the observation time, with droplets sticking to each other. The NG-3 mechanism found at the lowest polymer concentration above the binodal line shows coalescence of the liquid droplets, which grow linearly as a function of time, until the size of the droplets exceeds the field of view that we observe, and results in macroscopic phase separation. Regardless of the NG-i,

we observe a decay of the number of droplets as a function of time and a structure which evolves such that the size of a Voronoi cell increases linearly with the size of a droplet. Following Style's observation [78], we think that this may be due to the positions of the droplets being correlated via the Xanthan matrix and strong interactions of the droplets with each other through the high q value of our system.

Classifying the structures we observe in the usual reaction-limited or diffusion-limited cluster aggregation (RLCA/DLCA) fashion is not possible here. As for our system the individual colloids are not visible, we cannot tell if they are unsticking and travelling to other liquid droplets. Moreover, given that the NG-2 route shows droplets which aggregate, it would be interesting to observe it for longer and examine whether the growth stops before the structure collapses. This would then mean that NG-2 is in fact similar to NG-1 but given the lower concentration in polymer, the structure freezes later. On the other hand, probing the Xanthan matrix through rheological measurements for example would allow us to understand the mechanisms observed better. Finally, increasing the volume fraction of colloid, one could probe the spinodal decomposition region of the phase diagram with our high q value system and see whether similar arrested phase separation is observed at high polymer concentration.

Acknowledgments

Hannah Beeke and Julia Schollick are thanked for their useful preliminary work. Arran Curran is thanked for his technical help with the confocal microscopy, and Berend Van Der Meer is thanked for useful discussions.

Chapter 4

Thermal capillary waves of a colloidal liquid-gas interface in confinement

Abstract

In this chapter, the thermal capillary waves of the colloidal liquid-gas interface in confinement are studied. First, the theory of the static modes of fluctuations is introduced before their dynamics are discussed. Experimentally, the thermal capillary waves are observed on colloidal gas bubbles surrounded by colloidal liquid using confocal microscopy for different statepoints, and gas bubbles of different radii. The line tension as well as the dispersion relation are measured. The analysis leads to distinguish interfaces of a small size bubble which follow the theory explained here and larger ones, for which low modes need more time to equilibrate. Similarly, statepoints with a lower surface tension have low modes which need longer to relax than their lower counterparts. This comes from the fact that the relaxation time for each mode depends directly on the size of the interface and inversely on its surface tension.

4.1 Introduction

Fluid interfaces are ubiquitous in science and technology and even just over the past two decades, the number of publications on that topic has tripled [2]. The two-dimensional nature of interfaces between fluids can lead to innovative structures [79], and their properties can be can be applied to the formulation of cosmetics for instance [6], or to better understand how to form a foam for shampoos or beer [8].

Colloids are often used to study fluid interfaces may it be in academic contexts [79] or in industry, for example as stabilisers for certain foams [7], and colloids can also be used to make the fluid. Mixed with polymer under the right conditions, a colloid-polymer mixture can phase separate into colloidal liquid and colloidal gas phases. The interface separating those two phases shows an ultra-low surface tension $\gamma = k_B T/R_c^2 \simeq 1 - 100\,\mathrm{nN/m}$, against up to a million times more for molecular fluids [30]. This ultra-low surface tension means that thermal fluctuations are enough to excite the interface and its roughness is of the order of a micron, which is visible under confocal microscopy.

Confining the interface to a width comparable with its capillary length changes the geometry of the interface from a free, plane surface in bulk to a bubble which still fluctuates under thermal fluctuations. In biology, vesicles behave similarly. They are closed surfaces of bilayer membranes. Their mean shapes and fluctuations are governed by the competition of curvature energy and geometrical constraints on the enclosed volume and total surface area. A lot of theoretical and simulation work [80, 81] has been done to understand their deformations. Experimentally, confocal microscopy has been used to measure their bending rigidity [82], but looking at the dynamics of these fluctuations to measure a dispersion relation has yet to be done in a setting where the surface tension is non zero [83].

In this chapter, we derive the theory of thermal capillary waves on a circle and propose a dispersion relation to understand their dynamics for a system of colloid and polymer. We then experimentally observe these waves using confocal microscopy and measure the line tension of the gas bubbles, as well as study the changes induced by a change in statepoint. From the dynamics of the thermal fluctuations, we measure the dispersion relation of these thermal-capillary waves experimentally and compare them to what theory predicts.

4.2 Theoretical background

4.2.1 Static case

In our experiments, we observe the gas bubble through its mid-plane (see right-hand side in Figure 4.1), such that the interface is a fluctuating circle, where the height of the interface is described by the radius $r$which depends on the angle θ, see left-hand side in Figure 4.1. Following previous work done on this system [84], we first assume that the area of the bubble remains constant such that we can define a mean radius r_0 (see Figure 4.1), with a constant area of πr_0^2. The free energy of the interface is given by

$$F = \sigma C, \tag{4.1}$$

where C is the circumference of the bubble and σ the line tension associated with the interface. The circumference C is given by

$$C = \int_0^{2\pi} \sqrt{r(\theta)^2 + \left(\frac{\partial r(\theta)}{\partial \theta}\right)^2}\, d\theta. \tag{4.2}$$

Similarly to the case with a flat interface (see Chapter 2), we assume the fluctuations to be small such that we can approximate equation 4.2 as follows

$$C \approx \int_0^{2\pi} r(\theta)\, d\theta + \frac{1}{2r_0} \int_0^{2\pi} \left(\frac{\partial r(\theta)}{\partial \theta}\right)^2 d\theta. \tag{4.3}$$

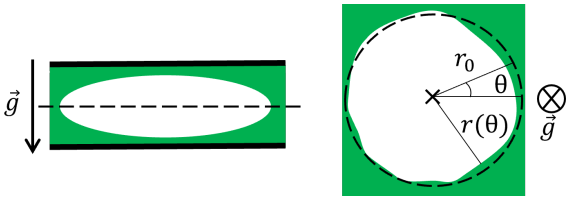


Figure 4.1: Left: Side view of the sample cell. The dashed line represents the plane through which we cut to observe the interface. Right: Top view of the interface. The dashed line is the circle of radius r_0 which has the same area as the bubble and same centre of mass. $r(\theta)$ is the radius of the real bubble at angle θ

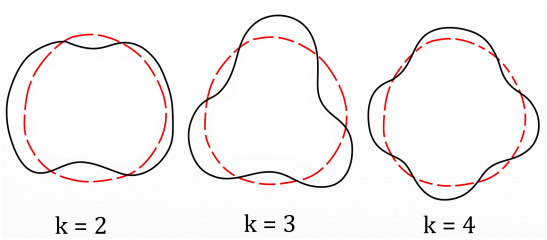


Figure 4.2: Schematics of the first three modes of interest: $k = 2$, $k = 3$ and $k = 4$. The mode number also corresponds to the number of minima or maxima in the mode. The red circles represent the circle of radius r_0. The deformations are exaggerated for better clarity.

We now introduce the relative radial displacement $u(\theta)$,

$$u(\theta) = \frac{r(\theta)}{r_0} - 1 \tag{4.4}$$

and we expand the fluctuating radius using a Fourier series,

$$r(\theta) = r_0 \left\{ 1 + \sum_{k=-\infty}^{\infty} u_k e^{ik\theta} \right\}. \tag{4.5}$$

The Fourier expansion is the mathematical expression of the fact that we decompose any instantaneous fluctuation into modes labelled with the index k. The first mode for $k = 0$ bears information about the area of the bubble, then the $k = 1$ mode has information about the translation of the circle with respect to its centre of mass. Those two modes do not contribute to the fluctuations, so we will not include them in the Fourier series. The modes with $k \geq 2$ represent a particular way to deform the interface, where the number k is not only the mode number but also the number of minima (or maxima) for each mode (see Figure 4.2).

To determine how much each of these modes weigh in any thermal fluctuation, we use a Fourier expansion with the circumference C and we obtain

$$C \approx 2\pi r_0 \left\{ 1 + \frac{1}{2} \sum_{k=-\infty}^{\infty} (k^2 - 1)|u_k|^2 \right\}, \tag{4.6}$$

and the free energy of the system F thus becomes

$$F = \sigma C \approx 2\pi r_0 \sigma + \pi r_0 \sigma \sum_{k=-\infty}^{\infty} (k^2 - 1)|u_k|^2. \tag{4.7}$$

Next, we use the equipartition theorem, which states that at thermodynamic equilibrium, each

mode gets $k_BT/2$, which leads to

$$\langle |u_k|^2 \rangle = \frac{k_BT}{2\pi r_0 \sigma} \left(\frac{1}{k^2 - 1} \right). \tag{4.8}$$

We Fourier transform this equation to find the static correlation function in real space, $g(\theta)$, defined by $g(\theta) = \langle u(\theta')u(\theta' + \theta) \rangle$ where the brackets denote an average over θ'. Noting that $\langle |u_k|^2 \rangle$ is an even function, we obtain

$$g(\theta) = \frac{k_BT}{2\pi r_0 \sigma} \sum_{k=2}^{\infty} \frac{\cos(k\theta)}{k^2 - 1}, \tag{4.9}$$

which can also be written

$$g(\theta) = \frac{k_BT}{2\pi r_0 \sigma} \mathrm{Re} \left[\sum_{k=2}^{\infty} \frac{e^{ik\theta}}{k^2 - 1} \right]. \tag{4.10}$$

Noting that (the proof is shown in the appendix at the end of this chapter)

$$\sum_{k=2}^{\infty} \frac{e^{ik\theta}}{k^2 - 1} = \frac{1}{2} \left\{ 1 + \frac{e^{i\theta}}{2} - 2i \sin(\theta) \ln(1 - e^{i\theta}) \right\}, \tag{4.11}$$

we can take the real part of equation 4.11 to obtain the following expression for $g(\theta)$

$$g(\theta) = \frac{k_BT}{4\pi r_0 \sigma} \left\{ 1 + \frac{\cos(\theta)}{2} + 2 \sin(\theta) \underbrace{\mathrm{Im}[\ln(1 - e^{i\theta})]}_{\mathrm{Arg}[1 - e^{i\theta}]} \right\}. \tag{4.12}$$

The static correlation function in real space is thus given by

$$g(\theta) = \frac{k_BT}{4\pi r_0 \sigma} \left[1 + \frac{\cos(\theta)}{2} + (\theta - \pi) \sin(\theta) \right]. \tag{4.13}$$

This function is particularly interesting as it has only one fitting parameter, the line tension σ. Note that $g(\theta)$ does not depend on the capillary length, as gravity plays no role in this confined system.

4.2.2 Dynamic case: the dispersion relation

We now consider the dynamics of the relaxation of a confined gas domain to derive a dispersion relation, see Figure 4.3. Two viscous liquids are confined between two walls separated by a distance w. Following the lubrication approximation, we neglect the inertial terms in the Navier-

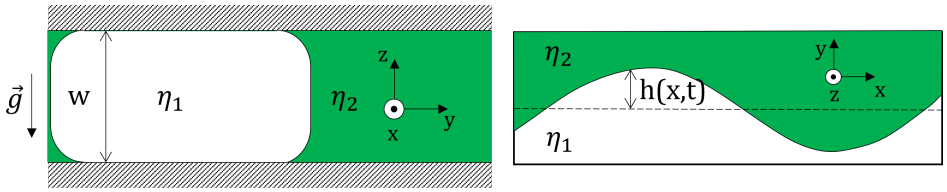


Figure 4.3: Parametrisation of the problem. Left: side view. The white phase is the gas bubble while the green phase is the liquid phase. Right: Top down view of a portion of the interface between the gas bubble and the surrounding liquid.

Stokes equation. Moreover, the pressure p does not depend on z and given the dimensions of the system, $v_z \ll v_x, v_y$. We assume the fluid is incompressible, which yields the following Navier-Stokes equation, at low Reynolds number:

$$-\overrightarrow{\nabla}_{3D}\, p + \eta \overrightarrow{\nabla}^2_{3D}\, \overrightarrow{v} = \overrightarrow{0}. \tag{4.14}$$

We then assume that $\frac{\partial p}{\partial z} = 0$ and $v_z = 0$. Furthermore, the lubrication approximation leads to a parabolic z-profile for v_x and v_y. After integrating along the z direction, we obtain:

$$-\overrightarrow{\nabla}_{2D}\, p + \eta \left(\overrightarrow{\nabla}^2_{2D} - \kappa^2 \right) \overrightarrow{v} = \overrightarrow{0}, \tag{4.15}$$

where $\kappa^{-1} \simeq w$. So far, this derivation is similar to that of the Poiseuille flow so the coefficient $\eta\kappa^2$ is comparable to the Poiseuille resistance of a slit $12\eta/w^2$. This means that

$$\kappa = \frac{2\sqrt{3}}{w}. \tag{4.16}$$

Since the two phases (gas bubble and liquid surrounding it) are assumed incompressible, we obtain for each phase noted (i):

$$-\overrightarrow{\nabla} p^{(i)} + \eta_{(i)} \left(\overrightarrow{\nabla}^2 - \kappa^2 \right) \overrightarrow{v}^{(i)} = \overrightarrow{0}, \tag{4.17}$$

$$\overrightarrow{\nabla} \cdot \overrightarrow{v}^{(i)} = 0. \tag{4.18}$$

$\overrightarrow{\nabla}$ and $\overrightarrow{v}$ are now defined in the (x, y) plane.

The boundary conditions at the interface are the continuity of the velocity along x and y as well as the continuity of the normal stress while the tangential stress is discontinuous. In

mathematical terms:

$$v_x^{(1)}(x,0,t) = v_x^{(2)}(x,0,t), \tag{4.19}$$

$$v_y^{(1)}(x,0,t) = v_y^{(2)}(x,0,t) = \partial_t h(x,t) \tag{4.20}$$

$$\sigma_{xy}^{(1)}(x,0,t) = \sigma_{xy}^{(2)}(x,0,t) \tag{4.21}$$

$$\sigma_{yy}^{(1)}(x,0,t) - \sigma_{yy}^{(2)}(x,0,t) = \gamma\, \partial_{xx} h(x,t). \tag{4.22}$$

We here define the stress tensor in phase i as follows:

$$\sigma_{\alpha\beta}^{(i)} = -\, p^{(i)}\delta_{\alpha\beta} + \eta_{(i)} \left(\partial_\alpha v_\beta^{(i)} + \partial_\beta v_\alpha^{(i)} \right), \tag{4.23}$$

with $\delta_{\alpha\beta}$ the Kronecker symbol. In addition, the pressure and velocity fields must vanish at infinity and as the equations are linear, we re-write them as:

$$\begin{aligned} \overrightarrow{v}^{(i)}(x,y,t) &= \overrightarrow{V}^{(i)}(y)\, e^{iqx-\omega t}, \\ h(x,t) &= H\, e^{iqx-\omega t}, \\ p^{(i)}(x,y,t) &= P^{(i)}(y)\, e^{iqx-\omega t}, \end{aligned} \tag{4.24}$$

with $q = k/r_0$ where k is the wavenumber of the static case: q is in m^{-1} while k is dimensionless. These expressions for the velocity, the height and the pressure mean that we now assume that pressure and velocity only depend on the y coordinate. Equations 4.17 and 4.18 lead to

$$\begin{aligned} V_x^{(i)} &= \frac{i}{q}\partial_y V_y^{(i)}, \\ P^{(i)}(y) &= \frac{\eta_i}{q^2}\left(\partial_{yy} - (q^2+\kappa^2)\right)\partial_y V_y^{(i)}, \\ \partial_{yyyy} V_y^{(i)} &- (2q^2+\kappa^2)\,\partial_{yy} V_y^{(i)} + q^2(q^2+\kappa^2)\, V_y^{(i)} = 0. \end{aligned} \tag{4.25}$$

The solutions are

$$\begin{aligned} V_y^{(1)} &= A_1\, e^{|q|y} + B_1\, e^{\sqrt{q^2+\kappa^2}\, y}, \\ V_y^{(2)} &= A_2\, e^{-|q|y} + B_2\, e^{-\sqrt{q^2+\kappa^2}\, y}. \end{aligned} \tag{4.26}$$

With the boundary conditions, we have five equations and five unknowns: A_1, A_2, B_1, B_2 and H. We then construct a determinant from the five equations (4.19 to 4.22), which we have to cancel to obtain a non trivial solution. This calculation is done in the appendix at the end of

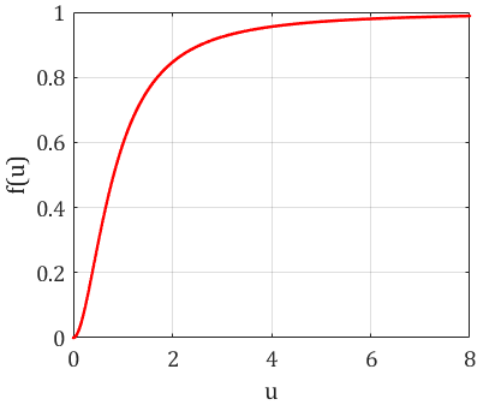


Figure 4.4: Shape of f as a function of u. $\hat{\eta}$ is fixed at 0.7 here.

this chapter. This leads to the following expression for the dispersion relation $\omega(q)$

$$\omega(q) = \omega_0(q)\, f\left(\frac{qw}{2\sqrt{3}}\right), \tag{4.27}$$

where

$$\omega_0(q) = \frac{\gamma|q|}{2(\eta_1+\eta_2)}, \tag{4.28}$$

and

$$f(u) = \frac{2u^2(\sqrt{u^2+1}-u)}{\sqrt{u^2+1}-\hat{\eta}u\left[8u^2(u^2+1)-4u(2u^2+1)\sqrt{u^2+1}+1\right]}, \tag{4.29}$$

with $\hat{\eta} = \left(\frac{\eta_1-\eta_2}{\eta_1+\eta_2}\right)^2$ and η_i the viscosity of phase i. η_1 is the viscosity of the gas phase while η_2 is that of the liquid phase. The first is on the order of 10 times that of water, while the second is higher than water but much closer to it such that if we assume that $\eta_1 = 10 \times \eta_{\text{water}}$ and $\eta_2 = \eta_{\text{water}}$, $\hat{\eta} = 0.7$. We now plot f as a function of u, see Figure 4.4. It is an increasing function varying from 0 to 1.

The expression for f being complex, we now examine asymptotic cases $q \ll \kappa$ and $q \gg \kappa$.

- For $q \ll \kappa$, the dispersion relation becomes

$$\omega(q \ll \kappa) = \frac{\gamma w^2 |q|^3}{12(\eta_1+\eta_2)}, \tag{4.30}$$

- In the opposite case, For $q \gg \kappa$, the dispersion relation becomes

$$\omega(q \gg \kappa) = \frac{\gamma|q|}{2(\eta_1+\eta_2)}. \tag{4.31}$$

4.3 Experimental methods

We study thermal capillary waves in confinement for two different statepoints described in table 4.1.

	Statepoint 1	Statepoint 2
ϕ_c	0.16	0.18
c_p	4	2
γ	21 nN/m	7 nN/m
L_c	4 μm	4 μm

Table 4.1: Characteristics of the two statepoints studied in this chapter.

4.3.1 Sample cell design

To prepare the sample cell, we follow the protocol illustrated in Figure 4.5. We drop 2.5 μL of the colloid-polymer mixture solution on a glass slide, which was cleaned with ethanol. We then lower a 15 mm $\times$ 15 mm coverslip of thickness between 130 μm and 170 μm on top that we have also cleaned with ethanol and dried under a gentle nitrogen flow. We lower it such that the drop of solution touches the coverslip on the edge of it first to minimise the risk of trapping a bubble of air in the middle of the coverslip. We seal the sample cell using NOA 61 UV glue that we spread all around the edges of the square coverslip so that it covers both the edge of the coverslip and the glass next to it. To minimise the evaporation of the solution, we place rectangular pieces of coverslips on top of the line of glue. Their role is to put weight on the glue such that any exiting air channel is chased out of the glue. Finally, we place this whole sample cell under the UV lamp for 20 minutes.

4.3.2 Data acquisition

We observe the bubbles of gas phase under a confocal microscope which is a 12 kHz resonant scanner head (Thorlabs) and a 532 nm laser, coupled to an Olympus IX73 inverted microscope equipped with a 60$\times$ (NA = 1.42) oil immersion objective (Olympus). The first step in the data acquisition process is to take a z-stack for each sample cell to measure their thickness. The typical sample thickness w is between 6 μm and 13 μm, see in Figure 4.6. This can be done even before complete equilibration. Because of the depletion interaction, the colloids wet both glass

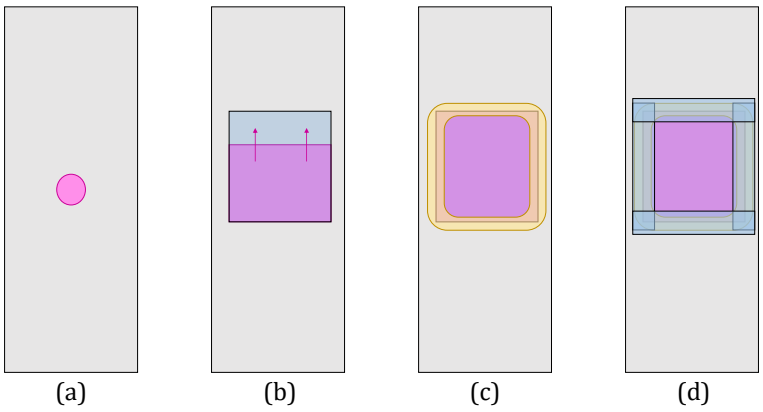


Figure 4.5: Schematics of sample cell making. (a) We drop 2.5 μL of solution on a clean microscope slide. (b) We put a coverslip on top such that the drop wets one edge and then invades it entirely through capillary action. (c) We add the glue (yellow) all round the edge of the coverslip. It must be placed such that it touches both the microscope slide and the coverslip. (d) We add pieces of a coverslip to weigh down on the glue and make sure that there are no air channels through which the solution could evaporate.

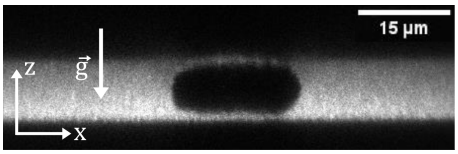


Figure 4.6: Z-stack taken by confocal microscopy.

surfaces at the top and at the bottom, which gives enough fluorescence signal to detect the glass edges and make a measurement. Then, the 512 x 512 pixel images were taken with the confocal microscope, at 4.5 images per second. Unless stated otherwise, the total duration of the data acquisition was about 20 minutes and the resolution of 200 nm per pixel.

4.3.3 Bubble location and edge detection

To track the bubbles, we first detect a circle with the built-in Matlab function (see left panel in Figure 4.7). This gives a first estimate of the position of the bubble. Then, we apply a circular mask onto the image, which has the same centre as the circle that has been detected and a radius R that we set to be between 1.5 or 2 times bigger, depending on how big the bubble is. This allows us to filter out any other partial or complete bubbles in the field of view (see right panel in Figure 4.7). After that, we binarise the image and invert it such that the phase of the bubble is white and the rest is black (see middle panel in Figure 4.7) to calculate the centre of mass of the image, which gives a better estimate of the centre of mass of the bubble, $O = [x_O, y_O]$. In the end, the picture is that on the right on Figure 4.7. The red cross is the centre of mass of the

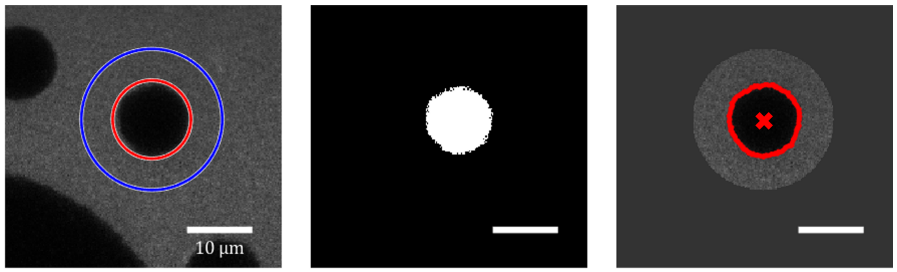


Figure 4.7: Image analysis process. Left: Confocal image microscopy. The red circle is the bubble as detected by Matlab's built-in routine. The blue circle has a radius R. Middle: Binarised image after inversion and exclusion from everything that is out of the blue circle. Right: Result of the 360 hyperbolic tangent fits from the red cross, which is the centre of mass of the binarised image. The red points are the detected interface. Everything beyond the radius R is assigned to have twice the intensity of the threshold used for the binarisation. All the scale bars are the same.

white pixels from the middle picture on Figure 4.7. To detect the colloidal liquid-gas interface, we fit the line of pixels starting at the centre O and extending outwards at an angle θ with a hyperbolic tangent function. The inflexion point gives the position of the interface. We carry out this step for 360 angles θ and 6000 images of the acquisition and save the coordinates of the 360 points and of the centres.

4.3.4 Corrections of the radii

First, we identify the centre of mass of the detected interface. This is crucial to avoid introducing errors in the lowest modes. With the binarisation method, the centre is not exact as depending on the threshold, it might be displaced in any direction. We therefore define the centre of mass of the bubble as the average of the points at the edge of it.

Next, we calculate the radii $r(\theta, t)$ as the distances between this new corrected centre O and the coordinates of the edges of the bubble. Then, we have to account for the possibility that the average shape of the bubble can be different from a perfect circle and some structure persists. As a consequence, the radial displacement is defined by susbtracting the average *shape* of the interface $\langle r(\theta, t)\rangle_t$, i.e. :

$$u(\theta, t) = \frac{r(\theta, t) - \langle r(\theta, t)\rangle_t}{r_0}. \tag{4.32}$$

Growth or shrinkage of the bubble through time is also corrected for, even though it is rarely a dominant feature through the experiments. To do so, we calculate the average of the

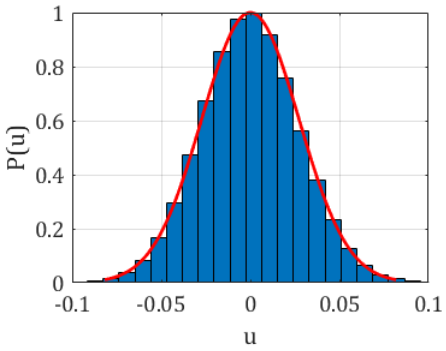


Figure 4.8: Probability distribution of the radial displacements u after corrections. The bars are the experimental data and the red line is the Gaussian fit. It is indeed centred around 0 and is symmetric.

radial displacement over the angles $u_\theta(t) = \langle u(\theta,t)\rangle_\theta$. We then substract it to $u(\theta,t)$.

In the end, the corrected radial displacement is given by

$$u(\theta,t) = \frac{r(\theta,t) - \langle r(\theta,t)\rangle_t}{r_0} - \left\langle \frac{r(\theta,t) - \langle r(\theta,t)\rangle_t}{r_0} \right\rangle_\theta . \tag{4.33}$$

After these corrections, we find that the distribution of the radii follows a Gaussian distribution (see Figure 4.8), similarly to the case of the flat interface, as expected for random interface fluctuations.

Area and perimeter of the bubble

Next, we test whether the perimeter $\mathcal{P}$ and the area $\mathcal{A}$ of the bubble are constant throughout the experiment. We see in Figure 4.9 that they fluctuate by a maximum of about 4% around their average values $\langle\mathcal{P}\rangle$ and $\langle\mathcal{A}\rangle$, which is consistent with the theoretical assumption that the perimeter and area are constant.

Correlation function calculation

The calculation of the correlation function $g(\theta)$ defined as

$$g(\theta) = \langle u(\theta',t)\, u(\theta'+\theta,t)\rangle_{(t,\theta')}, \tag{4.34}$$

has been carried out differently from the flat case. Here, we have to consider two cases. For $\theta' < 2\pi - \theta$, the calculation is identical to the flat case. However, if $\theta' > 2\pi - \theta$, then we have

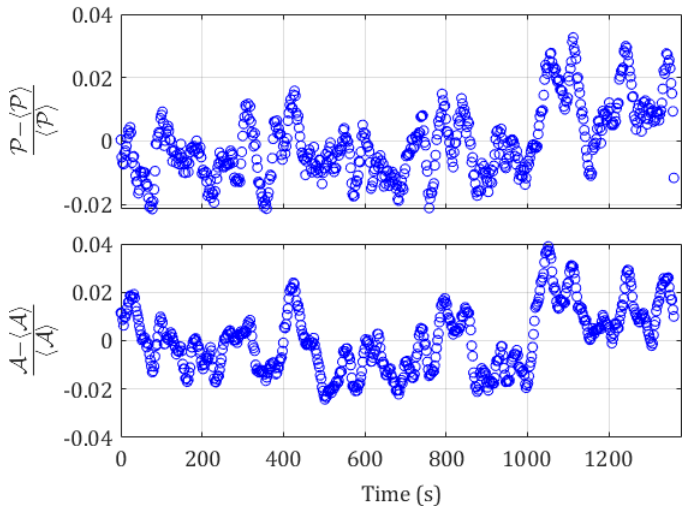


Figure 4.9: Fluctuations of the perimeter $\mathcal{P}$ and area $\mathcal{A}$ around their average values denoted with brackets as a function of time throughout the experiment.

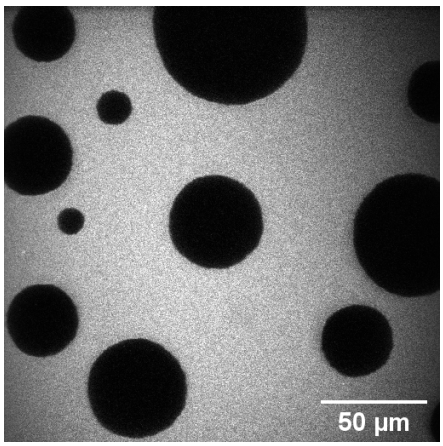


Figure 4.10: Confocal microscopy image, (x,y)-view of statepoint 1.

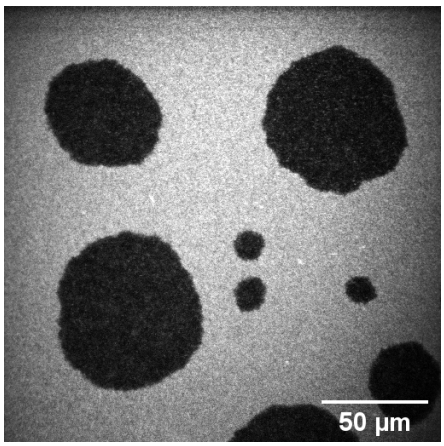


Figure 4.11: Confocal microscopy image, (x,y)-view of statepoint 2.

to consider the average of $u(\theta', t) \times u(\theta' - (2\pi - \theta), t)$.

4.4 Results and discussion

The sample cell is left overnight upside down (coverslip facing down) for phase separation and equilibration before observation the next day. Figures 4.10 and 4.11 show confocal microscopy images of both statepoints. The bubbles are made of colloidal gas phase and the surrounding medium is colloidal liquid. We can see that the interfaces of the bubbles of statepoint 1 are sharper than those of statepoint 2, which reflects the higher surface tension for bubbles of statepoint 1 (see table 4.1).

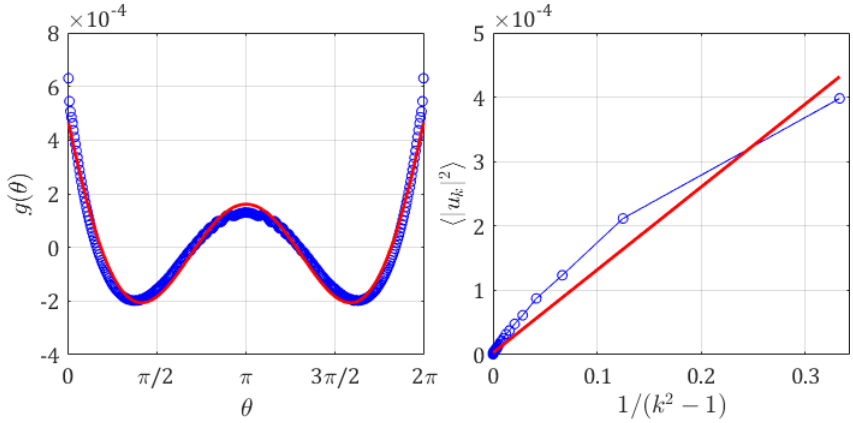


Figure 4.12: Left: correlation function $g(\theta)$. The blue symbols are the data and the red line is the fit with equation 4.13. Right: Amplitude of the Fourier modes as a function of $1/(k^2-1)$. The blue symbols are experimental data, linked with a straight line to guide the eye, while the red line is the linear fit.

4.4.1 Droplet of statepoint 1 with $R_0 = 5\,\mu$m

Figure 4.12 shows $g(\theta)$ the angular correlation function and the fit with the theoretical prediction (equation 4.13) on the left for a bubble of statepoint 1 and average radius $r_0 = 5\,\mu$m. The fit with equation 4.13 looks in reasonable agreement with the experimental data. From that, we can extract the line tension, which is here $\sigma = 3.5 \times 10^{-13}\,$N. We check this value against γw, which gives a good order of magnitude of the expected value for σ. This sample was made of statepoint 1 and the thickness was $11\,\mu$m, which yields a ratio of $2.3 \times 10^{-13}\,$N, in very good agreement with the value measured.

We then inspect the Fourier modes starting at $k = 2$ on Figure 4.12 on the right. Experimentally, the range of k values is bound between 2 and a higher value, $k_{\max}$, which corresponds to a small lengthscale l_m. Here, we choose to define it as the diameter of a colloid $l_m = 2r_c$, which, translated into angles gives $\theta_m = 2r_c/r_0$, which leads to $k_{max} = \pi r_0/r_c$. The data roughly follows the straight line although we do notice that the last point for $k = 2$ deviates from the fit. According to equation 4.8, we can extract a value for σ from the fit, which is here $\sigma = 3.6 \times 10^{-13}\,$N, in excellent agreement with the value measured on the correlation function.

The time correlation functions g_k gives information about the relaxation of the modes. According to [85], the time correlation function of each Fourier mode, $g_k(t)$, should relax exponentially with time. The relaxation time τ is given by

$$\tau = \frac{4r_0\eta}{\sigma k}, \tag{4.35}$$

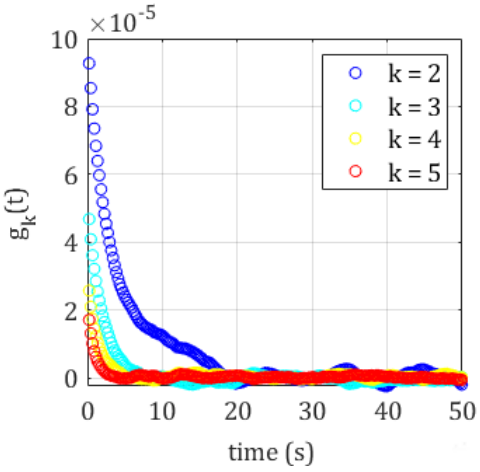


Figure 4.13: Time correlation function of the Fourier modes $g_k(t)$ for bubble $r_0 = 5\,\mu$m

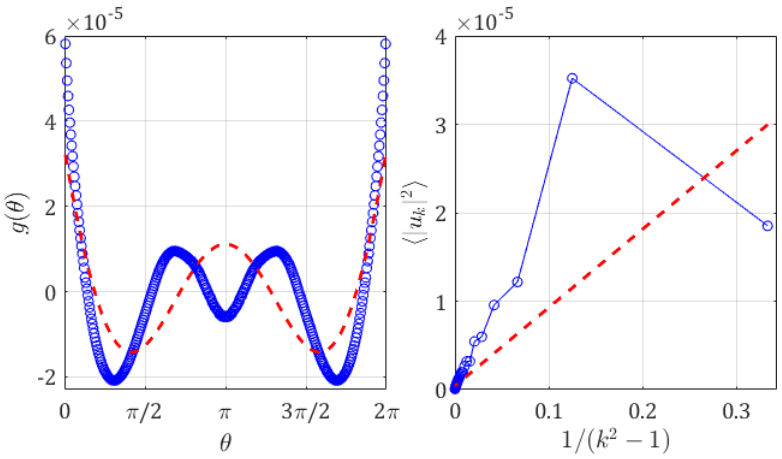


Figure 4.14: Left: correlation function $g(\theta)$. The blue symbols are the data and the red dotted line is the fit with equation 4.8. Right: Amplitude of the Fourier modes as a function of $1/(k^2-1)$. The blue symbols are experimental data, linked with a straight line to guide the eye, while the red dotted line is the linear fit, showing that for larger bubbles, the behaviour looks different. Those fits are not used to extract any values.

which is equivalent to what we obtain in equation (4.31) for large k, as $\tau = 1/\omega$. They are plotted in Figure 4.13 for modes $k = 2$ to $k = 5$. As predicted in [85], the decay of g_k is exponential and the decay time decreases as the mode number increases while the amplitudes of the curves decreases as the mode number increases, in agreement with equation 4.8.

4.4.2 Droplet of statepoint 1 with $R_0 = 29\,\mu$m

Next, we examine the case of large bubbles, whose radii are around or bigger than $15\,\mu$m. As before we calculate the angular correlation function and Fourier modes, which are shown for a bubble of statepoint 1 and radius $r_0 = 29\,\mu$m, see Figure 4.14. Unlike the $g(\theta)$ for small bubbles,

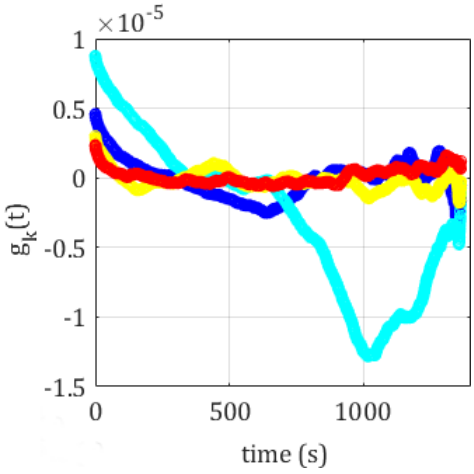


Figure 4.15: Time correlation function of the Fourier modes for bubble $r_0 = 29\,\mu$m.

there is a minimum around $\theta = \pi$, which makes the fitting procedure and extraction of the line tension unreliable. This minimum appears for large bubbles and its depth typically increases as the radius of the bubble increases. To elucidate where this drop at $\theta = \pi$ is coming from, we inspect the Fourier modes in Figure 4.14. We see that mode $k = 2$ deviates considerably from the rest of the data, which means that the dominant mode in the series becomes $k = 3$, which has 3 troughs, thus producing the minimum at $\theta = \pi$.

To explain this low amplitude for $k = 2$, we now take a look at the dynamics of the fluctuations, see in Figure 4.15. Contrary to the small bubble, modes $k = 2$ and $k = 3$ do not decay over the 20 min duration of the experiment. Moreover, the amplitude of the third mode is higher than that of the second mode and we notice that the third mode presents a large negative part. Besides, the $k = 2$ and $k = 3$ modes do not decay to zero at long times, whereas for the small bubble, it only takes about 30 s for all the modes to decay to zero. We attribute this to the fact that the lowest k modes, which are the slowest, need more time to relax.

To test whether the hypothesis of a longer duration of the experiment allows the lowest k modes to relax, we observe a bubble of radius $r_0 = 9\,\mu$m from statepoint 1 for 5 h. We then compare the correlation function and the amplitude of the Fourier modes obtained looking at only the first 20 min, and the same for the entire duration of the experiment. The results are presented on Figure 4.16. Between the top line where the first 20 min only of the experiment are analysed and the bottom line where the analysis is led over the total 5 h of the experiment, the difference in the correlation function is the behaviour around $\theta = \pi$. For the short experiment, $g(\theta \sim \pi)$ is flat and even presents a slight minimum, whereas for the long experiment, this

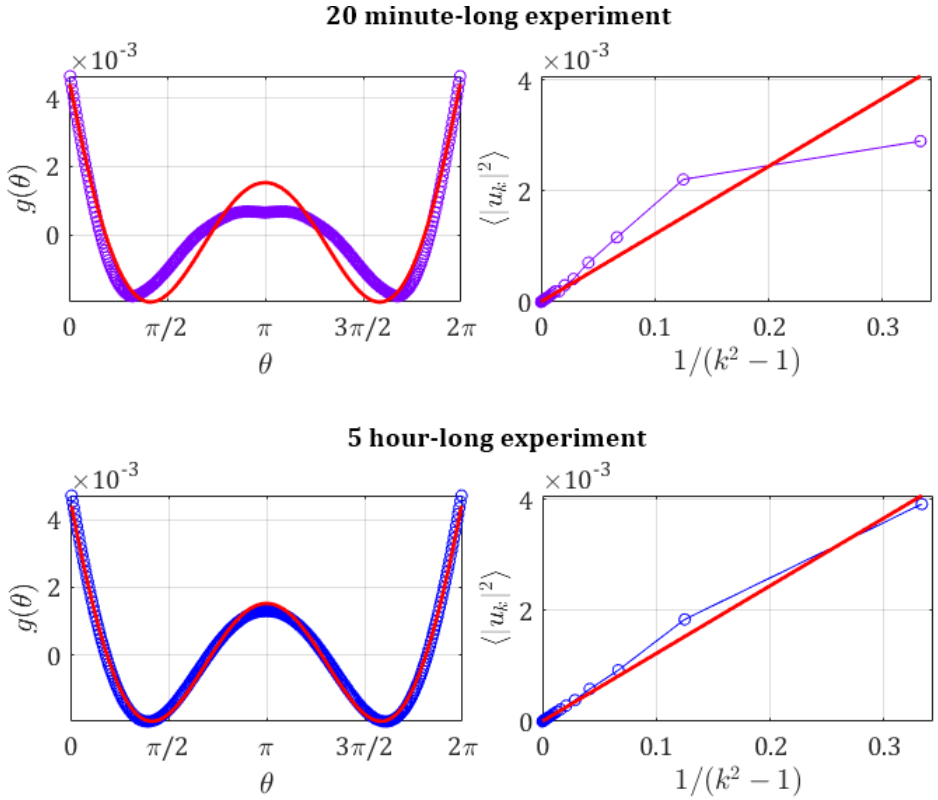


Figure 4.16: Top line: $g(\theta)$ (left) and amplitude of the Fourier modes (right) for the first 20 min of the experiment. Bottom line: $g(\theta)$ (left) and amplitude of the Fourier modes (right) for the 5 h-long experiment.

minimum is non existent and the fit with equation 4.8 is better. Moreover, the Fourier modes (left column on Figure 4.16) are noticeably different for the lowest modes, which are the highest values of $1/(k^2-1)$. As seen previously, the amplitude of the $k = 2$ mode is lower for the short experiment than for the long experiment. This thus confirms that the low k modes, particularly for large r_0, need a long time to relax and often longer than the 20 min of the usual data acquisition.

4.4.3 Comparison between statepoint 1 and 2

Now, we examine two bubbles, one at statepoint 1 and the other at statepoint 2, but both of radii $r_0 = 12\,\mu$m for a duration of 20 min. Their correlation functions, the amplitudes of the Fourier modes and their time correlation functions are shown in Figure 4.17. On the first line are both correlation functions $g(\theta)$. The bubble at statepoint 1 shows a correlation function which follows the theoretical prediction whereas the other one shows a minimum around $\theta \sim \pi$ and its troughs are deformed. Looking now at the amplitude of the Fourier modes (middle line

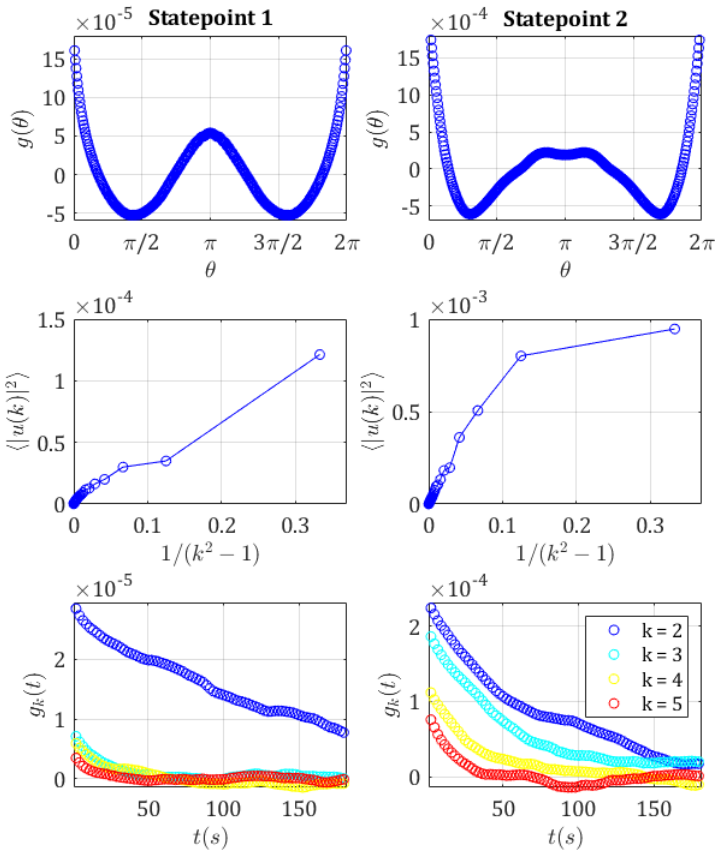


Figure 4.17: Observation of statepoint 1 (right) and statepoint 2 (left) for bubbles of radii $r_0 = 12\,\mu$m.

on Figure 4.17), the amplitudes for the bubble of statepoint 1 follow a straight line with only $k = 3$ being slightly weaker than expected. However, for the other bubble, $k = 2$ is much lower than expected and its value is almost equal to that of $k = 3$. This has consequences on the time correlation functions of these modes $g_k(t)$. For the bubble of statepoint 1, the curves for $k = 3$ and $k = 4$ are very close to each other whereas for the other bubble, the dominant mode $k = 2$ is much closer to $k = 3$ than expected. We understand this looking at the expression of the relaxation time of $g_k(t)$, given by equation 4.35, $\tau = \frac{4r_0\eta}{\sigma k}$. A good order of magnitude for σ is given by γw. Here, $\gamma_1 > \gamma_2$ so $\sigma_1 > \sigma_2$, which means that $\tau_1 < \tau_2$, for equal bubble size and fixed mode, which is consistent with our experimental observations.

4.4.4 Measurement of the dispersion relation

Next, we measure the dispersion relation, equation 4.27, and see which regime our system falls in between $q \ll \kappa$ and $q \gg \kappa$, see equations 4.30 and 4.31. As we do not know the viscosities of

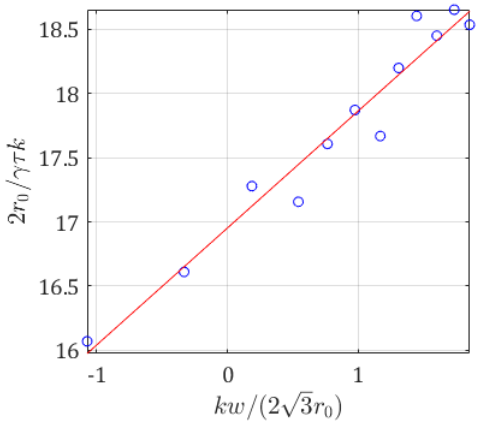


Figure 4.18: $2r_0/\gamma k\tau$ as a function of $kw/r_0 2\sqrt{3}$ on a log-log scale.

the gas and the liquid phase to calculate $\hat{\eta}$, we rewrite equation 4.27 as follows:

$$\underbrace{(\eta_1 + \eta_2)\, f(\frac{qw}{2\sqrt{3}})}_{F\left(\frac{qw}{2\sqrt{3}}\right)} = \frac{2\omega(q)}{\gamma|q|}, \tag{4.36}$$

which means in terms of what we measure experimentally

$$F\left(\frac{kw}{r_0 2\sqrt{3}}\right) = \frac{2r_0}{\gamma k\tau}. \tag{4.37}$$

To obtain ω, we measure the inverse of the decay time τ of $g_k(t)$ for $k = 2$ to 9 for the bubbles for which the $g_k(t)$ functions are exponentially decaying for the duration of the experiment. We then plot $2r_0/\gamma k\tau$ as a function of $kw/r_0 2\sqrt{3}$ on a log-log scale on Figure 4.18. The data falls on a line with a slope of ~ 1. This means that

$$\left(\frac{kw}{r_0 2\sqrt{3}}\right)^1 \propto \frac{2r_0}{\gamma k\tau}, \tag{4.38}$$

which entails

$$\tau \propto r_0^2 \tag{4.39}$$

The relaxation time thus increases as the square of the radius of the bubble, which means that between the small 5 μm-wide bubble and the large 29 μm-wide one, experimental time has to be about 36 times longer, amounting to 12 h. This also means that our system does not fall in either limits predicted by equation 4.30 or 4.31, but rather in between.

4.5 Conclusion and outlook

In summary, we have observed the thermal fluctuations of the interface separating bubbles of colloidal gas from the surrounding colloidal liquid under confinement, with confocal microscopy. We have found that the distribution of radial displacements follows a Gaussian law, meaning that what causes the fluctuations in the bubble's radius are only random thermal fluctuations. For bubbles with a radius typically smaller than $10\,\mu$m, we have measured the line tension of the interface by studying both the angular correlation function and the amplitude of the Fourier modes associated with the fluctuations of the interface. Both measurements agree with each other and are of a good order of magnitude. For larger bubbles, extracting a line tension has not been possible as the angular correlation function presents a minimum around $\theta = 180\,^\circ$ caused by the low k modes not relaxing fully during the observation time. By comparing two droplets of the same size but at different statepoints, we have shown that bubbles at a statepoint with a lower surface tension present modes which takes longer to relax than at a statepoint with a higher surface tension. Finally, we measured the dispersion relation for this range of ω and we find that

$$\omega(k) \propto \frac{\gamma}{2}\frac{w}{2\sqrt{3}}\left(\frac{k}{r_0}\right)^2. \tag{4.40}$$

To measure the dispersion relation for a wider range of both k and ω values, one would need to observe large bubbles for longer, such that all the modes have enough time to relax. Moreover, our study considered only the middle plane of the gas bubble but it would be interesting to carry out the measurements and analysis for the whole 3D bubble. Theoretical work [81] and simulations [80] have been laid out for biological vesicles and might apply to the case of colloid-polymer mixtures. Probing "bubbles of liquid" surrounded by the gas phase would be interesting. We do not expect the results to fully be symmetrical between a bubble of colloidal gas surrounded by colloidal liquid and vice versa. Firstly, as the colloidal liquid wets both the upper and lower glass walls, the geometry of liquid bubbles are in fact bridges of liquid with a hyperboloid shape, whereas bubbles of gas are ellipsoidal, see in Figure 4.19. In addition to that,liquid bridges can exchange colloids through the wetting layer, which is not true for a gas bubble. This could change the incompressibility condition and the wetting properties might be at play in the theory too.

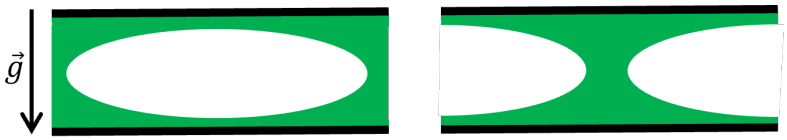


Figure 4.19: Left: geometry of a gas bubble surrounded by colloidal liquid. Right: geometry of a liquid bubble surrounded by colloidal gas.

Acknowledgements

Charles Savoie and Nina Elbers are thanked for his preliminary work. Jeffrey Urbach,Berend Van der Meer and Haim Diamant are thanked for their fruitful discussions.

Appendix

Equation 4.11

We here prove that

$$\sum_{k=2}^{\infty} \frac{e^{ik\theta}}{k^2-1} = \frac{1}{2}\left\{1 + \frac{e^{i\theta}}{2} - 2i\sin(\theta)\ln(1-e^{i\theta})\right\}. \tag{4.41}$$

To do so, we start from the right-hand side of the equality, and we drop the prefactor 1/2 for clarity:

$$\begin{aligned}
1 + \frac{e^{i\theta}}{2} - 2i\sin(\theta)\ln(1-e^{i\theta}) &= 1 + \frac{e^{i\theta}}{2} - 2i\sin(\theta)\,(-1)\sum_{k=1}^{\infty}\frac{e^{ik\theta}}{k} \\
&= 1 + \frac{e^{i\theta}}{2} + (e^{i\theta} - e^{-i\theta})\sum_{k=1}^{\infty}\frac{e^{ik\theta}}{k} \\
&= 1 + \frac{e^{i\theta}}{2} + e^{i\theta}\sum_{k=1}^{\infty}\frac{e^{ik\theta}}{k} - e^{-i\theta}\sum_{k=1}^{\infty}\frac{e^{ik\theta}}{k} \\
&= 1 + \frac{e^{i\theta}}{2} + \sum_{k=1}^{\infty}\frac{e^{i(k+1)\theta}}{k} - \sum_{k=1}^{\infty}\frac{e^{i(k-1)\theta}}{k}
\end{aligned}$$

We then change the indices in the two sums into $p = k+1$ and $l = k-1$, and we obtain

$$\begin{aligned}
1 + \frac{e^{i\theta}}{2} + \sum_{k=1}^{\infty}\frac{e^{i(k+1)\theta}}{k} - \sum_{k=1}^{\infty}\frac{e^{i(k-1)\theta}}{k} &= 1 + \frac{e^{i\theta}}{2} + \sum_{p=2}^{\infty}\frac{e^{ip\theta}}{p-1} - \sum_{l=0}^{\infty}\frac{e^{il\theta}}{l+1} \\
&= 1 + \frac{e^{i\theta}}{2} + \sum_{k=2}^{\infty}\frac{e^{ik\theta}}{k-1} - 1 - \frac{e^{i\theta}}{2} + \sum_{k=2}^{\infty}\frac{e^{ik\theta}}{k+1} \\
&= 1 + \frac{e^{i\theta}}{2} + \sum_{k=2}^{\infty}\frac{e^{ik\theta}}{k-1} - 1 - \frac{e^{i\theta}}{2} - \sum_{k=2}^{\infty}\frac{e^{ik\theta}}{k+1} \\
&= \sum_{k=2}^{\infty} e^{ik\theta}\left(\frac{1}{k-1} - \frac{1}{k+1}\right) \\
&= 2\sum_{k=2}^{\infty}\frac{e^{ik\theta}}{k^2-1},
\end{aligned}$$

which is equation 4.11.

Calculation of the dispersion relation

We here develop the calculation which leads to the dispersion relation. The solution for the velocity along the $y-$axis is given in equation 4.26. Using the incompressibility equation, we obtain

$$\begin{aligned} V_x^{(1)} &= A_1 \frac{i|q|}{q} e^{|q|y} + B_1 \frac{i\sqrt{q^2+\kappa^2}}{q} e^{\sqrt{q^2+\kappa^2}\,y}, \\ V_x^{(2)} &= -A_2 \frac{i|q|}{q} e^{-|q|y} + B_2 \frac{i\sqrt{q^2+\kappa^2}}{q} e^{-\sqrt{q^2+\kappa^2}\,y}. \end{aligned} \tag{4.42}$$

and equation 4.19 leads to

$$|q|(A_1 + A_2) + \sqrt{q^2+\kappa^2}\,(B_1 + B_2) = 0. \tag{4.43}$$

Then, by using equation 4.20, we obtain

$$\begin{aligned} A_1 + A_2 + \omega H &= 0, \\ B_1 + B_2 + \omega H &= 0. \end{aligned} \tag{4.44}$$

Equation 4.21 implies that

$$\left(|q| + \frac{q^2}{q}\right)(\eta_1 A_1 - \eta_2 A_2) + \left(|q| + \frac{(q^2+\kappa^2)}{q}\right)(\eta_1 B_1 - \eta_2 B_2) = 0. \tag{4.45}$$

And finally equation 4.22 leads to

$$|q|\left(\frac{\kappa^2}{q^2} + 2\right)(\eta_1 A_1 + \eta_2 A_2) + 2\sqrt{q^2+\kappa^2}\,(\eta_1 B_1 + \eta_2 B_2) + \gamma\, q^2 H = 0. \tag{4.46}$$

The five equations yield the following system

$$\begin{cases} |q|A_1 + |q|A_2 + \sqrt{q^2+\kappa^2}B_1 + \sqrt{q^2+\kappa^2}B_2 + 0H = 0 \\ 1A_1 + 0A_2 + 1B_1 + 0B_2 + \omega H = 0 \\ 0A_1 + 1A_2 + 0B_1 + 1B_2 + \omega H = 0 \\ \eta_1\left(q + \frac{q^2}{q}\right)A_1 + -\eta_2\left(q + \frac{q^2}{q}\right)A_2 + \eta_1\left(q + \frac{q^2+\kappa^2}{q}\right)B_1 + -\eta_2\left(q + \frac{q^2+\kappa^2}{q}\right)B_2 + 0H = 0 \\ \eta_1|q|\left(\frac{\kappa^2}{q^2}+2\right)A_1 + \eta_2|q|\left(\frac{\kappa^2}{q^2}+2\right)A_2 + 2\eta_1\sqrt{q^2+\kappa^2}B_1 + 2\eta_2\sqrt{q^2+\kappa^2}B_2 + \gamma q^2 H = 0 \end{cases}$$

There are 5 equations and 5 unknown amplitudes: A_1, A_2, B_1, B_2 and H. To obtain a non-trivial solution, we must cancel the determinant constructed from the these equations (4.19 - 4.22):

$$\begin{vmatrix} |q| & |q| & \sqrt{q^2+\kappa^2} & \sqrt{q^2+\kappa^2} & 0 \\ 1 & 0 & 1 & 0 & \omega \\ 0 & 1 & 0 & 1 & \omega \\ \eta_1\left(q+\frac{q^2}{q}\right) & -\eta_2\left(q+\frac{q^2}{q}\right) & \eta_1\left(q+\frac{q^2+\kappa^2}{q}\right) & -\eta_2\left(q+\frac{q^2+\kappa^2}{q}\right) & 0 \\ \eta_1|q|\left(\frac{\kappa^2}{q^2}+2\right) & \eta_2|q|\left(\frac{\kappa^2}{q^2}+2\right) & 2\eta_1\sqrt{q^2+\kappa^2} & 2\eta_2\sqrt{q^2+\kappa^2} & \gamma q^2 \end{vmatrix}, \tag{4.47}$$

which gives the dispersion relation equation 4.27.

Chapter 5

Laser-induced formation of colloidal liquid droplets in the colloidal gas phase

Abstract

In this chapter, a tightly focused beam of laser light is used to nucleate a droplet of colloidal liquid into the colloidal gas phase. The theory of kinetics of growth of a laser grown droplet is laid out before the experimental techniques used to observe them are explained. We study laser-induced nucleation as a function of laser power and height above the colloidal liquid-gas interface. We find that the final size of the droplet varies very little with the laser power and height above the interface. The growth kinetics are also similar throughout all the experiments and it is found that the main mechanism for droplet growth is the electrostrictive forces of the laser.

5.1 Introduction

Droplets are formed in nature in different contexts and different sizes. The morning dew on the grass is an example of millimetre-sized drops of water, while clouds are another example where the size of the drops is about $10\,\mu$m. In academia, the use of microfluidic devices is a way to control droplet formation [86], which can be useful to create model membranes [87] in biology. In industry, the study of droplet nucleation is key for inkjet printing [88].

There are generally two ways through which these drops are formed. The first is called *homogeneous nucleation* and the second is *heterogeneous nucleation*. The former refers to the formation of a nucleus in the bulk of a supersaturated gas phase. This nucleus is a small droplet and for it to survive, it must be created such that its radius exceeds a critical value for which the cost in surface free energy is at least exactly balanced by the gain in volume free energy. As such, the nucleation process has an energy barrier associated with it. On the other hand, heterogeneous nucleation requires either a substrate or a solute on which the droplet nucleates or a solute which lowers the price to pay in surface free energy for the droplet to survive, and the energy barrier for nucleation considerably.

Typically, in a molecular system such as water, the supersaturation required to nucleate a droplet through homogeneous nucleation is very high. It is in fact so high that the natural way to form these droplets is through heterogeneous nucleation. However, for a colloidal liquid-gas system, nucleation is much easier. The key reason is that for colloidal systems, the surface tension of the liquid-gas interface is much lower, up to a million times smaller than the molecular equivalent. The surface tension γ scales like k_BT/σ^2, where σ is the size of the colloid or the molecule. For colloids, $\gamma_{colloids} \sim 10\,\mathrm{nN/m}$, whereas for molecular systems $\gamma_{molecule} \sim 1\,\mathrm{mN/m}$.

Nucleation events happen spontaneously and as can be difficult to study in a controlled way. Here, we wait for the system to phase separate completely and take advantage of the low surface tension to nucleate droplets of the liquid phase inside the gas phase using optical tweezers. We aim to observe the dynamics of growth of the droplet and its final size as a function of distance from the interface and laser power.

5.2 Theory

The geometry of our experiments is illustrate in Figure 5.1. With our laser, we create an optical trap at a height h above the gas-liquid interface. The laser potential will attract particles from the colloidal gas phase to its minimum, at the centre of the beam, thus locally creating a higher density in the colloidal gas phase (see Figure 5.1). We will focus on two aspects of this

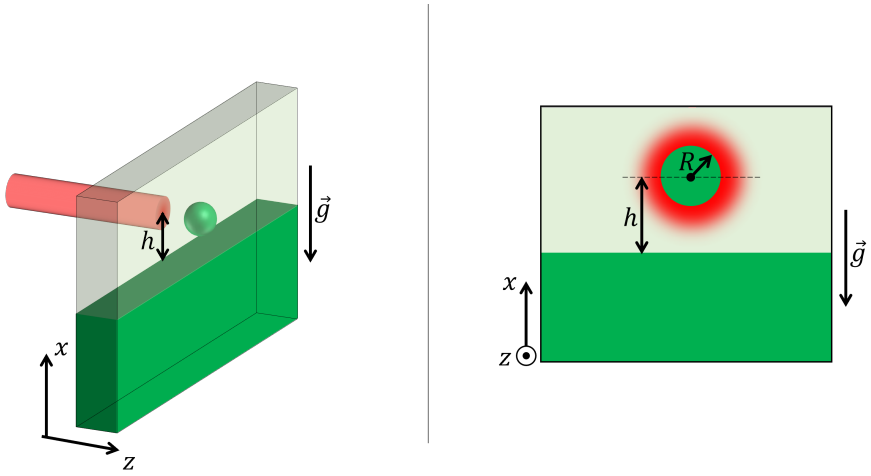


Figure 5.1: 3D and flat schematics of the setup. The red beam is the IR laser laser beam forming a trap in the colloidal gas phase, which attract particles until a liquid droplet is formed.

experiment. The first one is the final size of the droplets and the second is the growth kinetics. Delville established the theory behind the kinetics of laser-induced phase separation in a binary mixture in [89]. Here, we follow the same steps to derive the growth rate of a droplet inside a laser trap.

Firstly, we note that the action of the laser on the gas phase has several effects. The first one is to pull the colloids to the region of highest intensity, i.e. the centre of the beam. This is called *electrostrictive* effects. The second one is to push the colloids along the $z-$direction due to the radiation pressure. Finally, the laser may heat the solution locally, generating a thermal gradient. The colloids then move to the region of highest or lowest temperature, depending on their Soret coefficient. In this model, we do not consider the radiation pressure and focus on electrostrictive and thermal effects.

Let $\phi(\mathbf{r}, t)$ be the local volume fraction of the colloids. ϕ_0 and $\phi_E(\mathbf{r}, t)$ are respectively the volume fraction without the laser and the first order (in intensity) perturbation induced by the laser. Let us assume that the laser-induced perturbation in volume fraction has reached a steady

sate, such that $\phi_E(\mathbf{r}, t) = \phi_E(\mathbf{r})$, and given the symmetry of experimental geometry (see Figure 5.1), we assume that the changes in volume fraction will happen radially, i.e. $\phi_E(\mathbf{r}) = \phi_E(r)$. We consider a droplet of radius R located in the centre of the beam and solve the steady state diffusion equation for it

$$\nabla^2\phi(r) = \nabla^2\phi_E(r). \tag{5.1}$$

The boundary conditions here are that the volume fraction far away from the laser is that of the gas phase without the laser, ϕ_0, and that at the surface of the droplet, $\phi(r = R) = \phi_R(R)$, hence,

$$\begin{cases} \phi(r \longrightarrow \infty) = \phi_0 \\ \phi(r = R) = \phi_R(R) \end{cases}. \tag{5.2}$$

The solution of equation 5.1 with the boundary conditions given in equations 5.2 is

$$\phi(r) = \phi(0) + \phi_E(r) + (\phi_R(R) - \phi_0 - \phi_E(R))\,\frac{R}{r}. \tag{5.3}$$

The total flux of colloids at the droplet interface $\mathbf{J}_S(R)$ is

$$\mathbf{J}_S(R) = 4\pi R^2 D\,[\nabla\phi]_{r=R}, \tag{5.4}$$

and using equation 5.3, we obtain

$$\mathbf{J}_S(R) = 4\pi R D \left\{ \left[\frac{\partial}{\partial r}(r\phi_E(r)) \right]_{r=R} + \phi_0 - \phi_R(R) \right\} \frac{\mathbf{r}}{r}, \tag{5.5}$$

where D is the diffusion coefficient of the PMMA particles in the gas phase.

We now assume that the optical forces are not too strong such that the surface tension of the droplet is not affected by it. In that case, the Gibbs-Thomson relation, which describes the relation between surface tension and saturation vapour pressure in a binary system [90], gives

$$\phi_0 - \phi_R(R) = \frac{1}{(\phi_0 - \phi_d)(\partial\mu/\partial\phi)_T}\frac{2\gamma}{R}, \tag{5.6}$$

where ϕ_d the volume fraction inside the droplet and μ is the chemical potential per unit volume. Now by mass balance, the total flux of colloids in and out of the droplet is equal to its volume

change, which gives

$$\mathbf{J}_S(R) = (\phi_d - \phi_0)\frac{d}{dt}\left(\frac{4}{3}\pi R^3\right)\frac{\mathbf{r}}{r}. \tag{5.7}$$

We use the expression of the flux, equation 5.5, and find that the growth rate of the droplet is given by

$$\frac{dR}{dt} = \frac{D}{R}\left\{\frac{1}{\phi_d - \phi_0}\left[\frac{\partial}{\partial r}(r\phi_E(r))\right]_{r=R} - \frac{2d_0}{R}\right\}, \tag{5.8}$$

where

$$d_0 = \frac{\gamma}{(\phi_d - \phi_0)^2(\partial\mu/\partial\phi)_T}. \tag{5.9}$$

The two contributions of the laser light (electrostrictive forces and thermal effects) are in fact included in $\phi_E(r)$, as

$$\phi_E(r) = \phi_{el}(r) + \phi_{th}(r), \tag{5.10}$$

where $\phi_{el}(r)$ is the electrostrictive contribution and $\phi_{th}(r)$ the thermal one. Pouligny *et al.* show in [91] that

$$\begin{cases} \phi_{el}(r) \propto |\mathbf{E}|^2(r) \\ \phi_{th}(r) \propto T_E(r) \end{cases}, \tag{5.11}$$

where $|\mathbf{E}|^2(r)$ is the mean value of the square amplitude of the optical field over one optical period and $T_E(r)$ is the first order perturbation in temperature induced by the laser. In other words,

$$T(r) = T_0 + T_E(r), \tag{5.12}$$

with T_0 the temperature far from the laser. Furthermore, assuming that the laser is Gaussian, $|\mathbf{E}|^2(r) = E_0^2 \exp(-r^2/a_0^2)$, where a_0 is the beam radius, which means that $\phi_{el}(r) = (\phi_{el})_0 \exp(-r^2/a_0^2)$. For the thermal part, one uses the heat transfer equation and solves it at steady state:

$$\Lambda\nabla^2 T_E(r) + \alpha_a I(r) = 0\,. \tag{5.13}$$

Here α_a and Λ are respectively the absorption coefficient and the thermal conductivity of the gas phase. The intensity $I(r)$ is given by $I(r) = 1/2\epsilon_0\epsilon v|\mathbf{E}|^2(r)$, where v is the light velocity in the gas phase. Given the spherical symmetry, the intensity $I(r)$ of the laser beam is

$$I(r) = \frac{P}{4\pi a_0}\exp(-r^2/a_0^2)\,, \tag{5.14}$$

with $P = \int_0^\infty 4\pi r I(r) dr$ the beam power. The boundary conditions we use to solve the heat transfer equation 5.13 are that far away, the temperature induced by the laser is zero and its variation also goes to zero, i.e.

$$\begin{cases} T_E(r \longrightarrow \infty) = 0 \\ (\partial T_E/\partial r)(r \longrightarrow \infty) = 0 \end{cases} . \tag{5.15}$$

We obtain the following solution

$$T_E(r) = \frac{\sqrt{\pi}}{2} \left(\frac{\alpha_a P}{8\pi\Lambda} \right) \frac{\mathrm{erf}(r/a_0)}{r/a_0} , \tag{5.16}$$

where $\mathrm{erf}(x) = 2/\sqrt{\pi} \int_0^x \exp(-u^2) du$. Combining this with 5.11, we obtain

$$\phi_{th}(r) = (\phi_{th})_0 \frac{\mathrm{erf}(r/a_0)}{r/a_0}. \tag{5.17}$$

We now come back to the growth rate equation 5.8 and separate the electrostrictive and thermal contributions. In the end, under electrostrictive forces, the droplet growth rate is

$$\frac{dR}{dt} = \frac{D}{R} \left[\frac{(\phi_{el})_0}{\phi_d - \phi_0} \left(1 - 2\frac{R^2}{a_0^2} \right) \exp\left(-\frac{R^2}{a_0^2} \right) - \frac{2d_0}{R} \right] , \tag{5.18}$$

and under thermal forces, one obtains

$$\frac{dR}{dt} = \frac{D}{R} \left[\frac{(\phi_{th})_0}{\phi_d - \phi_0} \exp\left(-\frac{R^2}{a_0^2} \right) - \frac{2d_0}{R} \right] . \tag{5.19}$$

Neither of these equations are linear or easily solvable by hand, which is why Delville solves them numerically and plots $R(t)$ for a purely electrostrictive growth and a purely thermal driven one. The key finding is that each of these mechanisms can be approximated by a distinct power law: electrostrictive forces generate a $R(t) \propto t^{1/2}$ growth law, whereas thermal effects lead to $R(t) \propto t^{1/3}$.

Moreover, from an experimental point of view, even if we can measure ϕ_0 and ϕ_d, $(\phi_{el})_0$ and $(\phi_{th})_0$ are hard to measure or calculate. Their expressions are given in [89] to be

$$\begin{cases} (\phi_{el})_0 = \frac{1}{2}\epsilon_0 K_T \phi_0^2 (\partial\epsilon/\partial\phi)_T E_0^2 \\ (\phi_{th})_0 = -\frac{\rho_0 k_T}{\rho_c T_0} \left(\frac{\alpha_a P}{8\pi\Lambda} \right) \end{cases} , \tag{5.20}$$

where

- K_T is the osmotic compressibility,
- ρ_0 is the number density of the sample before the laser is shone through,
- ρ_c is the number density of the colloids,
- $k_T = D_T/D$, with D_T the thermodiffusion coefficient, is the Soret coefficient [92].

5.3 Experimental methods

The optical setup used is the one described in Chapter 2.

5.3.1 Sample cell design

The sample cell we use is a channel made of UV glue sealed between a microscope slide and a 15 mm × 15 mm coverslip of thickness between 130 μm and 170 μm. A schematic of the steps to make it is presented in Figure 5.2. First, we wash the microscope slide and the coverslip with ethanol and dry it under a gentle nitrogen flow. We then mix some UV glue (NOA 81) with 15 μm silica particles and we use the tip of a 0.1 to 2 μL pipette to deposit a line of this mixture at the top and at the bottom of the coverslip see Figure 5.2 (a). We then flip it and carefully push it against the microscope slide such that the glue spreads see in Figure 5.2 (b). The glue now forms a channel and the silica beads in it act as spacers that prevent the sample cell from being thinner than their diameter of 15 μm. We put the sample cell to cure under a UV-lamp for 15 min before dropping 2 μL of the solution of PMMA and Xanthan mixture at one end of

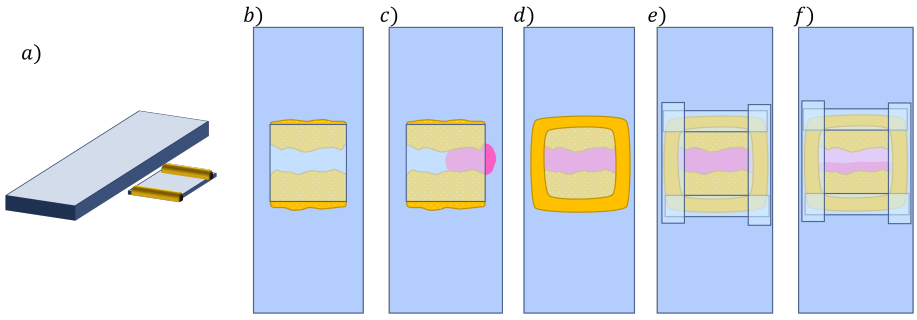


Figure 5.2: Steps followed to make a sample cell.

the channel and wait for the solution to enter through capillary action, see in Figure 5.2 (b). As soon as the solution has filled the entire channel, we quickly put an additional layer of glue (UV NOA 68) all around the coverslip to seal the channel see in Figure 5.2 (d) to prevent the evaporation of the 2 μL of solution. We make sure that the glue is both on the coverslip and the microscope slide before putting four thin pieces of a coverslip on top of the glue. We gently press them down, see in Figure 5.2 (e). This step is crucial and extends the average lifetime of a sample from hours to multiple days as it pushes the glue down on the glass, which makes sure that no air channel is left that would allow evaporation of the solution. Finally, we put the sample back under the UV-lamp for another 15 min. Overnight, on the microscope, the sample phase separates as shown in Figure 5.2 (f).

5.3.2 Image acquisition

We turn the laser on and observe the nucleation of a droplet for three different heights h above the interface: $h = 20\,\mu$m, $40\,\mu$m and $60\,\mu$m. We also use three different laser powers P: $P = 900\,$mW, $P = 1.4\,$W and $P = 2.1\,$W. The image acquisition consists in taking one image every 2.5 s for half an hour; this makes a total of 720 images per droplet.

5.3.3 Image corrections and measurement of droplet radius

To get rid of some persistent bright pixels, we apply a median filtering on the image (7 pixels by 7 pixels). We then track the radius of the droplet as a function of time. To locate the centre of mass of the droplet $O(x_O, y_O)$, we first binarise the image using the average intensities of gas and liquid phases as a threshold. We find that this step has to be carried out for each image and even if the position of the laser does not change in time, if the centre of mass of the droplet is badly located, the detection of the radius will be biased. For early times, no droplet is found as its intensity is not above the binarisation threshold, and the radius is assigned to be zero. As soon as a droplet is detected, we locate its centre of mass and extract the intensity profiles in 4 directions, at $\theta = 0$, $\theta = \pi/2$, $\theta = \pi$ and $\theta = 3\pi/2$ from O. We fit each of these profiles with a hyperbolic tangent function and the radius is the position of the inflexion point, similarly to what we do with the flat interface to extract the height. The average of these four radii is the radius for that time, $R(t)$.

5.4 Results and discussion

We obtain the droplets shown in Figure 5.3. The droplet at $h = 20\,\mu$m grown with $P = 2.1\,$W

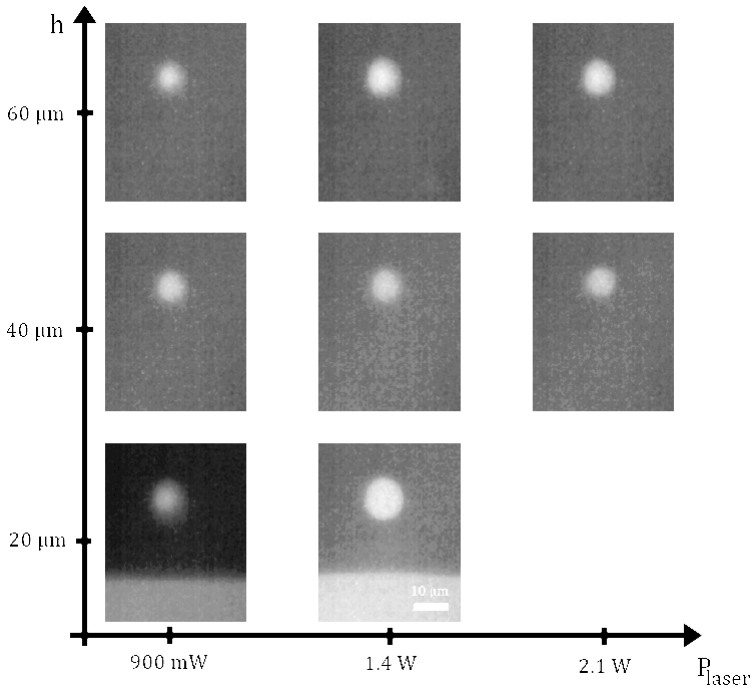


Figure 5.3: Fluorescence microscopy images of the all the droplets nucleated. The images shown here are taken at the end of each growth experiment. The scale bar applies to all the images.

is not shown here because it was not possible to nucleate it. In fact, for that case, the laser also pulls the interface up such that the droplet connects with it. One can see this effect starting to appear for the droplet grown at $h = 20\,\mu$m and $P = 1.4\,$W.

5.4.1 Final size of the droplet

The first observation is that the final size of the droplet fluctuates around $5\,\mu$m but not in a monotonous way across laser power and height. We can see it both in the images Figure 5.3 and in the plots Figure 5.4. The width of the radial intensity profiles do not vary significantly as a function of height above the interface or laser power.

We attribute the independence of the droplet radius with the height above the interface to the large gravitational length of our system. For our PMMA colloids, the gravitational length

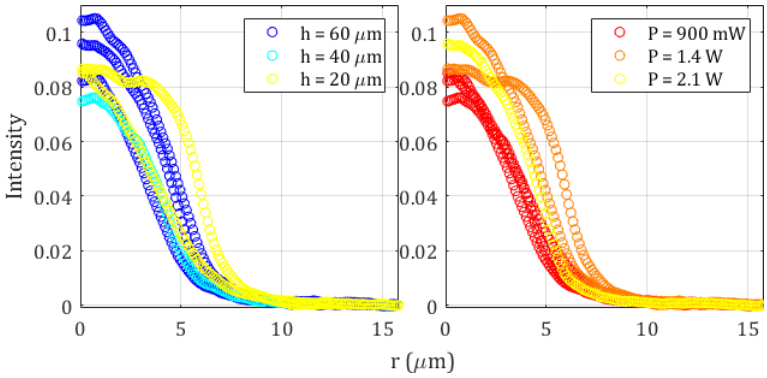


Figure 5.4: Azimutal average of the intensity starting from the centre of the droplet. On the left, the plots are colour-coded according to the height and on the right, according to the laser power.

is given by

$$l_g = \frac{k_B T}{m_b g} = \frac{k_b T}{\frac{4}{3}\pi R^3(\rho_{PMMA} - \rho_{water})g} = \frac{1.38 \times 10^{-23} \times 298}{\frac{4}{3} \times \pi \times (1 \times 10^{-7})^3 \times (1180 - 1000) \times 9.8} = 0.5\,\text{mm}\,, \tag{5.21}$$

which means that for all h values probed here, the concentration of colloids in the colloidal gas phase is the same. In other words, we are in the limit where $l_g \gg h$. Probing heights that compare with the gravitational height here is not possible as the maximum field of view of the camera is $215\,\mu\text{m} \times 215\,\mu\text{m}$.

In Figure 5.3, we see that the droplets grown at $h = 20\,\mu\text{m}$ are slightly bigger than the others. We think that this comes from the proximity of the droplet to the liquid-gas interface, such that the wetting layer on the glass wall is thicker at $h = 20\,\mu\text{m}$.

With regards to the laser power, the droplet size does not show a clear trend as we increase the trapping power. This can be explained using a result found for the case of trapping a single colloid. The underlying laser potential can be written as the following Gaussian

$$U_{laser} = -V_0 \exp\left(-r^2 \frac{k}{V_0}\right), \tag{5.22}$$

where V_0 is the depth of the potential, k is the trap stiffness and r is the distance to the trap. Single colloid trapping tells us that the ratio k/V_0 is a constant with respect to laser power as both these variables depends linearly on it [39, 40, 93]. That means that the standard deviation of the Gaussian remains fixed. However, given the V_0 prefactor, the higher the laser power, the deeper the potential well and the more colloids are trapped, so the intensity of the droplet should increase. Looking at Figure 5.5, this trend does not seem to be qualitatively followed

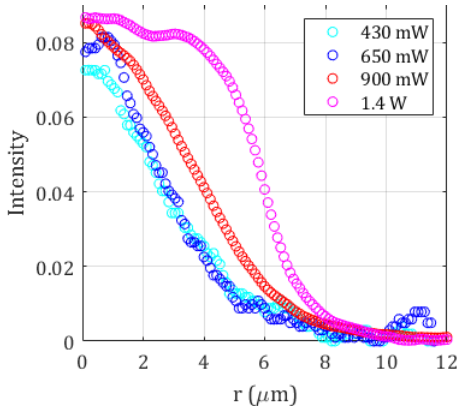


Figure 5.5: Different droplet shapes for a fixed height of $h = 20\,\mu$m, at different laser powers.

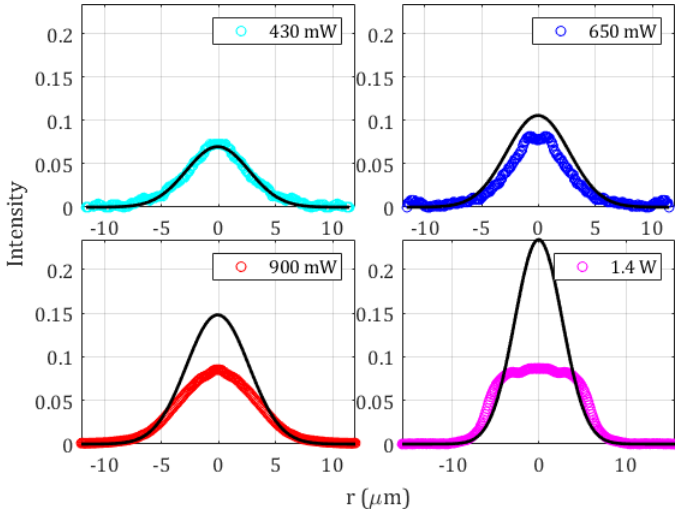


Figure 5.6: Intensity as a function of radius for different laser powers. The height is still fixed at $h = 20\,\mu$m. The black line denotes the fit for the first one and the Gaussian I_P for the other graphs. The data was also flipped in the negative r range for more visual clarity and convenience for the fitting procedure.

when it comes to the depth of the potential. The numbers show us that quantitatively, droplets are not as bright for twice the laser power, and if we look again at Figure 5.4, this trend does not seem to hold through the heights. Moreover, the width changes slightly between 430 mW and 900 mW before jumping significantly when it comes to 1.4 W.

However, there is another way to explain the different shapes of the intensity profiles for different laser powers. Given the single colloid trapping result, let us fit the lowest laser power curve (with $P = 430\,\text{mW}$) with a Gaussian, $I_{430mW} = I_0 \exp\left(-(r/\delta)^2\right)$. Let us then plot a Gaussian I_P for the other intensity profiles with the same standard deviation δ and a maximum value of $I_0 \times P(mW)/430$ to scale the prefactor with the laser power. The results are shown in Figure 5.6. As one could see in Figure 5.5, the maximum of the graphs seem to saturate at

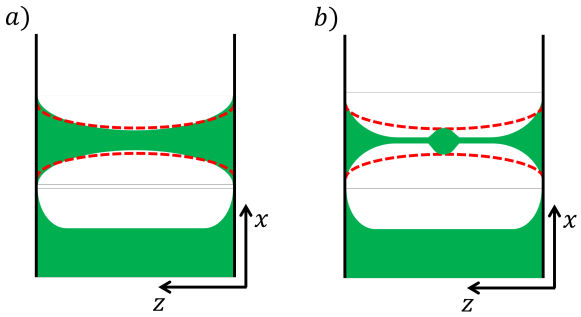


Figure 5.7: a) Scenario with a bridge of colloidal liquid bridge formed from one wall of the sample cell to the other. This would happen if the laser power is strong enough in all the $z-$slices to lead to phase separation. The droplet in the middle is mixed with the bridge. b) Scenario with a droplet in the middle and two thinner bridges left and right from it. This could happen as the surface tension separating the bridge and the gas phase is very low. This scenario could happen for lower laser power than in the a) schematics. Due to radiation pressure, this scenario could be asymmetric.

about $I = 0.09$, but what Figure 5.6 shows is that the standard deviation of all the Gaussians do agree quite well. The maximum of the intensities however seem truncated, especially in the $P = 1.4\,\mathrm{W}$ case where the top of the profile is flat. This hints at the fact that either the droplet is cylinder-shaped, or the droplet is actually connected to both ends of the sample cell, on the walls, and instead of forming a droplet, we are forming a bridge of colloids from one end where the beam waist sits at least. It could go all the way to the other wall of the sample cell or it could be that because of the radiation pressure, the symmetry between positive and negative z is broken. The cylinder-shaped droplet is not credible as the surface tension of it, even if it is low, would hardly favour such a shape. However, the idea of a bridge (see a) in Figure 5.7 explains both the flat shape at the top and the fact that the intensity looks truncate in Figure 5.6. This bridge of colloids then cannot accommodate more colloids, regardless of the laser power, which explains the fact that the droplets all look identical, intensity-wise. Looking again at Figure 5.6, the shapes for the $P = 430\,\mathrm{mW}$ and $P = 650\,\mathrm{mW}$ profiles do not look parabolic or Gaussian-like at the top. It rather looks like two decaying exponentials with a short, flat top. The plateau close to the centre might be due to a droplet in the middle of the sample while the sides might come from the shape of the bridge, see Figure 5.7.

5.4.2 Growth kinetics

Next, we plot $R(t)$ for all the droplets in Figure 5.8. All the curves are growing from $t = 0$, which is the first time at which a droplet is detected until the end of the experiment. Interestingly, regardless of laser power or height, the growth curves are very similar, at the exception of a

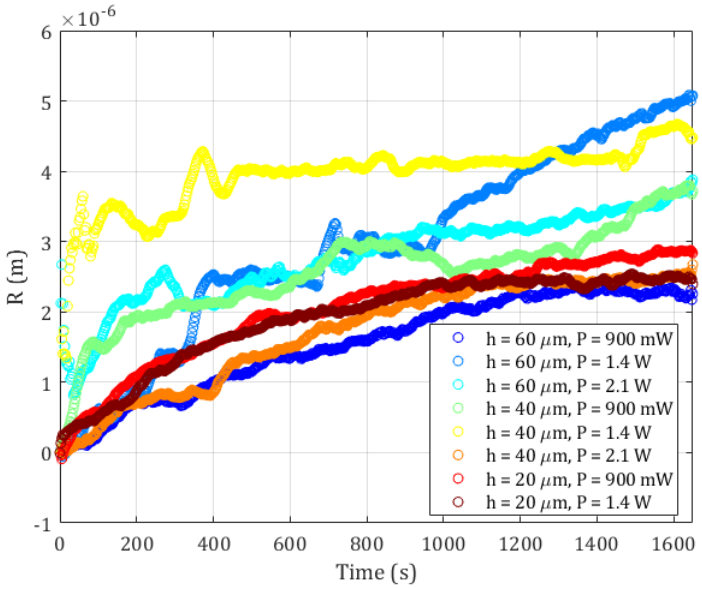


Figure 5.8: Radii as a function of time for all droplets.

few. One also notices that some show a rapid growth to a plateau (see $h = 40\,\mu$m, $P = 1.4\,$W in Figure 5.8) and some show growth spurts (see $h = 60\,\mu$m, $P = 1.4\,$W on Figure 5.8). The structures formed, whether it is droplets or bridges grow at a similar rate to a similar maximum size. As there is no dependence of the kinetics on the laser power or the height above the liquid-gas interface, we decide to average all these growth curves into one, $\hat{R}(t)$ (see top graph in Figure 5.9). Plotting it on a log-log scale (see bottom graph in Figure 5.9) shows that the growth law

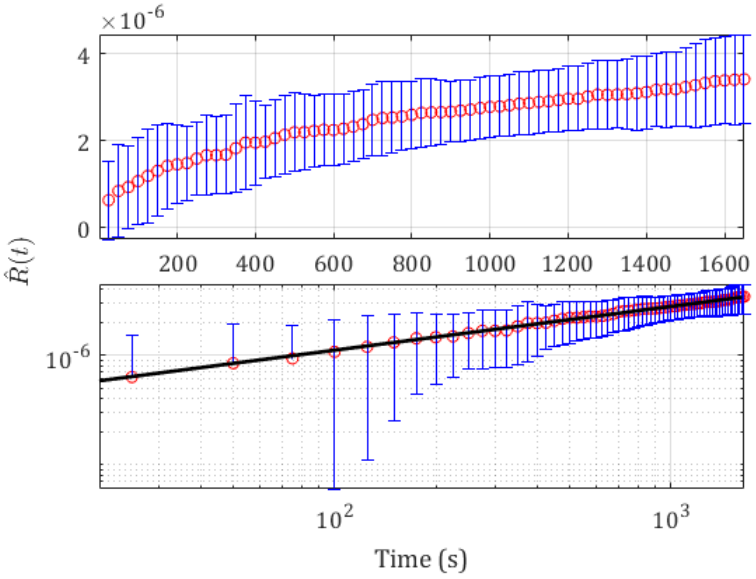


Figure 5.9: Average radius $\hat{R}$ as a function of time. Top graph is in natural scale, bottom graph is in a log-log scale. The error bars are given by the standard deviation of all the droplets. The black line is the linear fit, the slope is 1/2.

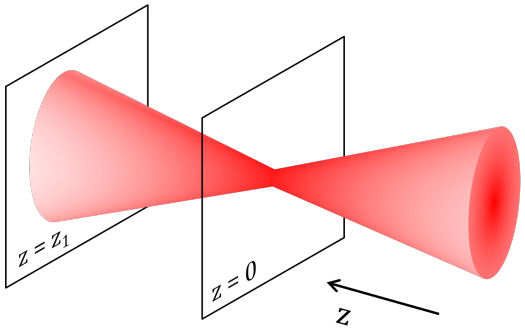


Figure 5.10: Schematics of the laser beam shape. The plane $z = 0$ cuts the beam at its waist while $z = z_1$ is further away..

follows a power law of 1/2. This result was predicted by Delville *et al.* in [89] (see section 5.2) for droplet growth that is purely electrostrictive, i.e. due to the difference of refractive index between the colloids and the solvent. As a consequence, thermal effects have no influence on droplet growth which is confirmed by Verhoeff *et al.* who carried out trapping experiments at low laser power with this exact same system of PMMA colloids and Xanthan in heavy water, and found that thermal effects were negligible [42].

The kinetics here follow the law predicted for a sphere whereas the data suggests that we might in fact be nucleating bridges, with a very different symmetry. From a geometric optics point of view, the laser is focusing at its waist and that is where it is the most intense, i.e. where the potential well is the deepest. However, the Gaussian potential well exists in each $z-$plane. Now the further the $z-$plane is from $z = 0$, the wider the potential well and the less deep it is. There are then two scenarios shown Figure 5.11. Either the laser power induces a change in volume fraction ϕ_E locally strong enough to cross the binodal line and lead to phase separation into liquid and gas (see a) in Figure 5.11; or the power isn't strong enough for phase separation but will only weakly increase the local volume fraction. This depends on the intensity in the trap and where we consider this in the beam. Close to the waist is where scenario a) is most likely, while far from the $z = 0$ plane and at high r, the second scenario is more likely.

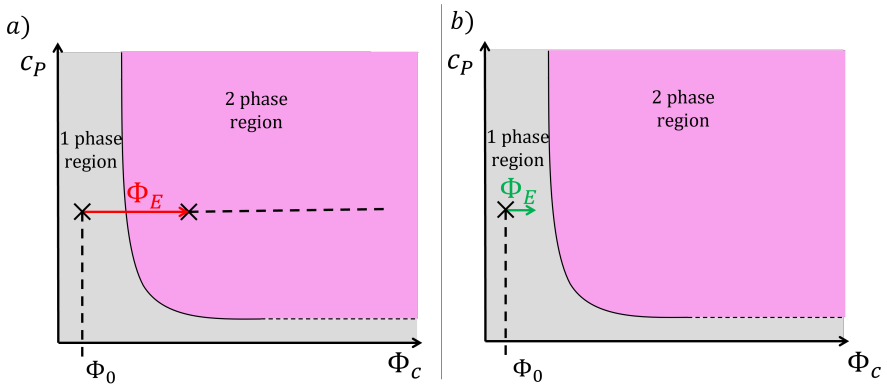


Figure 5.11: Two scenarios possible inside the laser beam. a) The power is strong enough to lead to phase separation. b) The power is not strong enough to lead to phase separation but only leads to a denser gas phase.

5.5 Conclusion and outlook

We have successfully nucleated droplets of colloidal liquid in the colloidal gas phase using optical tweezers. We did so at three different heights away from the liquid-gas interface and for three different laser powers. The height is found to have no effect on the growth kinetics or the final size of the droplet and we suggest that this might be due to the fact that h is very small compared to the gravitational length. The laser power does not influence the droplet size or the growth kinetics. However, we find that the maximum intensity of the trap is capped at a certain value, which we attribute to the nucleation of a bridge rather than a spherical droplet. The growth kinetics are found to follow a power law with an exponent of $1/2$, which shows that the growth is purely driven by electrostrictive effects.

To have a better understanding of the exact 3D structure that we nucleate, one would require confocal microscopy to scan along the $z-$direction and reconstruct the shape of the droplet or bridge. It would also be interesting to carry out similar experiments with a system with a gravitational length comparable with the height of the trap. This way, one expects to see the size of the droplets decrease as nucleation takes place higher away from the interface. It would also be interesting to characterise the structure of the colloids inside the trap. With this system, the colloids are too small to be clearly resolved individually and compute volume fractions. But moving to a system of bigger colloids, one could measure the volume fraction inside the trap to see if it increases as the laser power increases. One could also then visualise the movement of individual particles and see whether the radiation pressure is significant. Finally, with bigger colloids, one could probe whether the colloids can be trapped such that they undergo

a phase transition into a crystal phase inside of the laser beam.

Acknowledgments

Arran Curran is thanked for his help to build the tweezing and microscopy setup, and Taiki Yanagishima for fruitful discussions.

Chapter 6

Evaporation of laser-induced droplets of colloidal liquid in the colloidal gas phase

Abstract

In this chapter, the evaporation of liquid droplets nucleated with optical tweezers is studied. First, the theory for the diffusion of colloids away from a droplet is laid out. The droplet evaporation process is observed with fluorescence microscopy after the laser used for tweezing was switched off. In particular, we study the evaporation of droplets nucleated at a height of $40\,\mu$m and $60\,\mu$m above from the colloidal liquid-gas interface. From solving the diffusion equation, the diffusion coefficient of the colloids into the gas phase is measured. It is found not to vary with the height above the liquid-gas interface or the laser power used to nucleate the droplets. For droplets grown at a height of $20\,\mu$m, droplets sink at a constant velocity as they evaporate and interact with the liquid-gas interface below them.

6.1 Introduction

According to the International Union of Pure and Applied Chemistry, evaporation is the "physical process by which a liquid substance is converted to a gas or vapour". A common example of evaporation is found in how tree leaves can evaporate an amount of water that is multiple times their weight, and its impact on meteorology [94]. Multiple studies have been conducted to understand the way water circulates inside a tree [95] or the role of evaporation and how to control it for agricultural purposes [96]. These are an example of naturally occurring evaporation, but there are also numerous applications of evaporation in industry. For example, evaporation is a process used to concentrate substances: condensed milk is made from milk which was heated to about 90 °C so that about 60% of the water evaporates.

More recently, the study of evaporation kinetics has been conducted in different molecular systems in contact with substrates [97], for droplets with various shapes [98]. For long-lived droplets which are not in contact with a substrate, research has been done in molecular systems [99, 100].

Evaporation can also be established in colloidal systems. It has been observed for systems of droplets in contact with a substrate in [101] for instance, where the shape of the droplet and its rate of evaporation can be measured as a function of time. As seen in the previous chapter, a tightly focused laser beam, also called optical tweezers, can be used to nucleate a droplet of colloidal liquid into the colloidal gas phase. The droplet holds as long as the laser is on without it being in contact with any surface.

In this chapter, we study the evaporation of the droplet as the laser is turned off. We first introduce the theoretical elements to understand the evaporation of the droplet through the diffusion of the colloids it contains. Experimentally, we study the evaporation of droplets nucleated at heights $h = 20\,\mu$m, $40\,\mu$m and $60\,\mu$m above the interface separating the colloidal liquid and gas phases for three different laser powers: 900 mW, 1.4 W and 2.1 W. We find two different scenarios for the evaporation dynamics. The first one happens for droplets at height $h = 20\,\mu$m, which sink and interact with the colloidal liquid-gas interface and the second one, for droplets at heights of $40\,\mu$m and $60\,\mu$m, where droplets evaporate while remaining fixed in space.

6.2 Theoretical background

To understand the evaporation dynamics in terms of the diffusion of colloids out of a spherical colloidal liquid droplet, we consider the simplest diffusion equation, derived from the equation of local conservation of matter:

$$\frac{\partial n}{\partial t} + \nabla \cdot \overrightarrow{j} = 0, \tag{6.1}$$

where n is the number density of colloids in m^{-3} and $\overrightarrow{j}$ is the flux of particles, given by $\overrightarrow{j} = n\overrightarrow{v}$, with $\overrightarrow{v}$ the velocity of the colloids. We now use Fick's law that states that the flux of particle is proportional to the gradient of their concentration,

$$\overrightarrow{j} = -D(\overrightarrow{r}, n)\nabla n(\overrightarrow{r}, t) \tag{6.2}$$

where D is the diffusion coefficient. This means that the only driving force for the colloids to diffuse out of the droplet is the difference in concentration in and outside the droplet. Note that we ignore all interactions between the colloids, and with the polymer. We also assume that the diffusion coefficient is constant. Combining equations 6.1 and 6.2, we obtain the diffusion equation,

$$\frac{\partial n}{\partial t} = D\Delta n. \tag{6.3}$$

Experimentally, however, we do not measure the density of the particles but the intensity of the fluorescence. To link the density and intensity, we assume that they are proportional, $n(r,t) = \alpha I(r,t)$, and that they only depend on the distance r from the centre of the droplet and time t. This means that the diffusion equation becomes

$$\frac{\partial I}{\partial t} = D\Delta I. \tag{6.4}$$

As we assume the droplet to be spherical, we write this equation in spherical coordinates,

$$\frac{\partial I}{\partial t} = D\,\frac{1}{r^2}\frac{\partial}{\partial r}\left(r^2\frac{\partial I}{\partial r}\right), \tag{6.5}$$

which describes how the intensity of light changes in space and time as the particles diffuse out of the droplet.

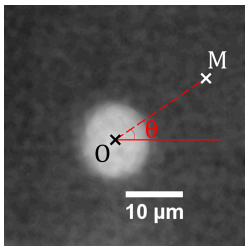


Figure 6.1: Fluorescence microscopy image of the droplet and segment $[OM]$ for a given θ.

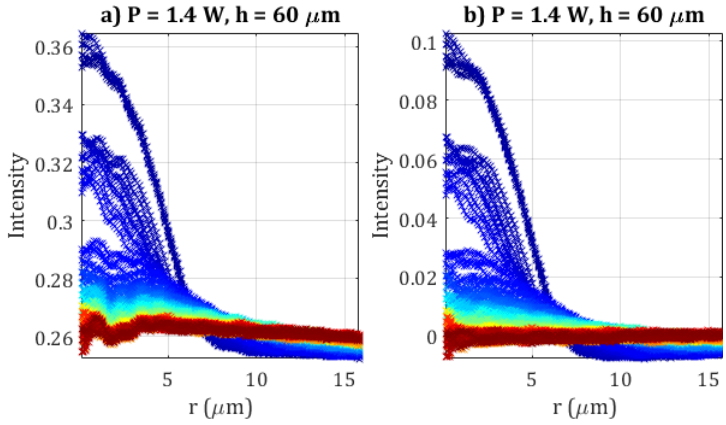


Figure 6.2: a) Raw $I_{raw}(r,t)$ before corrections. Note the trough at $r = 1.5\,\mu$m. b) $I(r,t)$ after substraction of the average of I over the last 20 frames. We note that the curves for later times (the red ones) are mostly flat at a value of 0 intensity and the trough previously observed on a) has disappeared.

6.3 Experimental methods

We use the optical setup described in Chapter 2 and the sample cell is the same as the one described in Chapter 5.

6.3.1 Image corrections

We start with a median filtering on the image to get rid of persistent bright pixels, as for the nucleation. We then binarise the image using the average between the intensity of the gas phase and that of the liquid phase as a threshold. This allows us to find the droplet and its centre of mass $O(x_O, y_O)$. From the centre, we compute the intensity $I_{raw}(r,\theta,t)$ along a segment $[OM]$ of length 150 pixels ($\simeq 15\,\mu$m) at angle θ (see Figure 6.1). We do this for 360 angles and then average over θ such that for each picture, we measure one average $I_{raw}(r,t)$. This intensity can be plotted in time and as a function of r for each time t (see Figure 6.2). The first observation is that even at very late times, on the red curves, there is some structure. To correct for that, we substract the intensity averaged over the last 20 frames $I_{20}(r) = \langle I(r,t)\rangle_{last20frames}$.

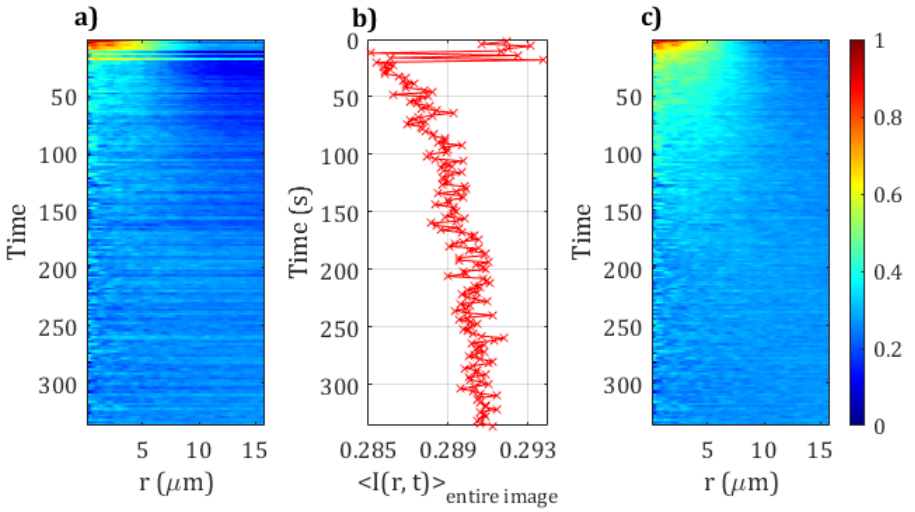


Figure 6.3: a) Data for $P = 2.1\,\mathrm{W}$ and $h = 60\,\mu\mathrm{m}$ before correction with respect to the average. We note that some lines are brighter than others. b) Average intensity as a function of time. The spikes correspond to the flashes seen on a). c) After correction and rescaling, the bright lines have now gone and the colour plot is overall much smoother.

Next, we see two sudden decreasing steps in intensity. The first one (see Figure b) on 6.2) happens between $I = 0.1$ and $I = 0.06$ at early times. We attribute it to the moment when we block the laser beam. The fluorescence signal being brighter before we block the laser hints at the two-photon excitation of the rhodamine by the laser light, given that the wavelength of the laser is twice that of the excitation of the fluorophore. Wu use this to define $t = 0$.

The colour plot of I as a function of r and t (see (a) on Figure 6.3) shows that a few times appear brighter than others. This happens for all sets of data at different times and to different extents. We realised that the average intensity on a whole image, which consists of liquid, gas and droplet, as a function of time also shows spikes (see (b) on Figure 6.3), and they correspond to the flashes in intensity. We attribute these jumps to either the illumination flickering, or the camera. Because those flashes do not saturate the image, those images still contain the information that we need. We just need to correct for the artificial offset. To that end, we substract the average intensity $I_{global}(t) = \langle I(r,t)\rangle_{entire\ image}$ calculated on the entire image as a function of time to the intensity $I(r,t)$. After this step, we rescale the intensities such that they vary between 0 and 1 as follows,

$$I(r,t) = \frac{I_{raw}(r,t) - min(I_{raw}(r,t))}{max(I_{raw}(r,t)) - min(I_{raw}(r,t))} \tag{6.6}$$

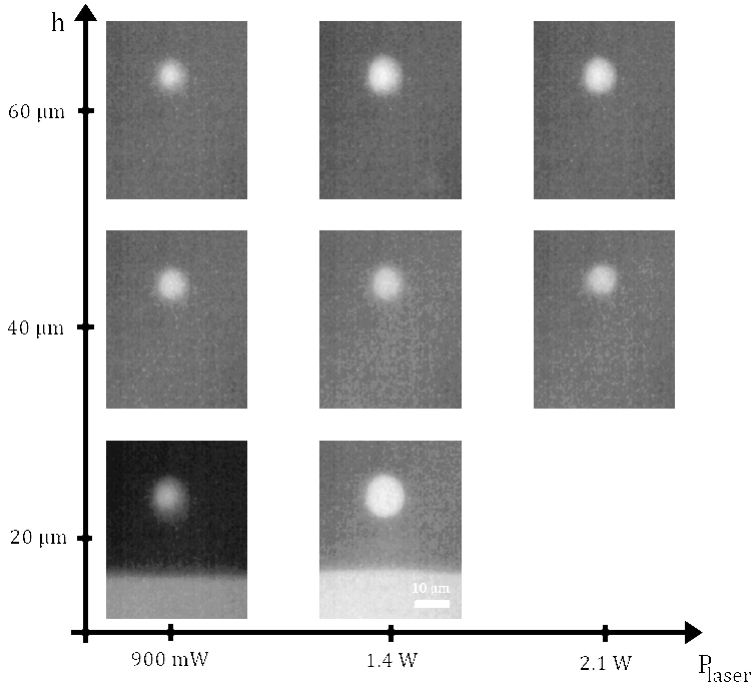


Figure 6.4: Fluorescence microscopy images of the all the droplets nucleated. The images shown here are taken at the beginning of each evaporation experiment. The scale bar applies to all the images.

6.4 Results and discussion

We here observe droplet evaporation after the laser is blocked, once they reach their final size, about 30 min after the start of their nucleation. Experimentally, we start an acquisition of 150 frames taken every 2 seconds and block the laser beam. This protocol was followed for all the droplets (see Figure 6.4), regardless of their height above the interface or the laser power used to nucleate them.

We note that the maximum intensity after we block the laser is comparable to the intensity of the liquid phase (see Figure 6.5). This confirms the hypothesis made in the nucleation chapter (Chapter 5) about the fact that the intensity saturates because we are in fact nucleating a bridge. Given that we assume the density of particles to be proportional to the intensity, this means that the trap maintains the colloids at a density close to that of the liquid. This is the case for all three heights and all three laser powers probed here.

We attribute the fact that the density does not change significantly with respect to the height from the interface to the gravitational length of the particles being about half a millimetre, such that a difference of 20 μm is negligible, as showed also for the nucleation process in Chapter

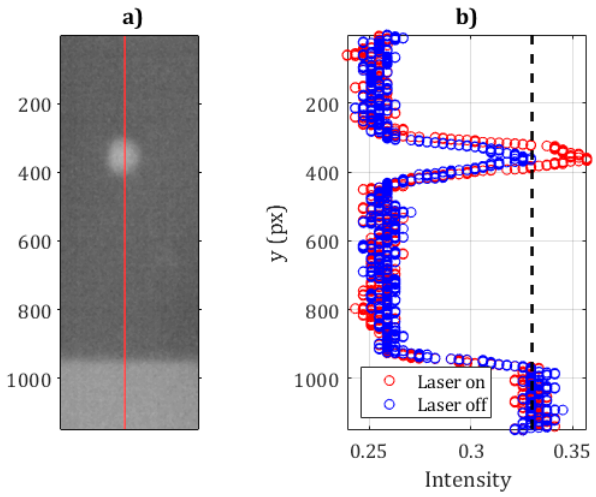


Figure 6.5: a) Fluorescence microscopy image while the laser is still on. the red line denotes the line along which the profiles on b) where measured. The width of the image is 42 μm. b) Profiles measured along the red line noted in a). The red symbols were measured while the laser was still on, the blue symbols, right after switching the laser off. The black dotted line is a guide to the eye at $I = I_{liq}$. The values of intensity have not been corrected here.

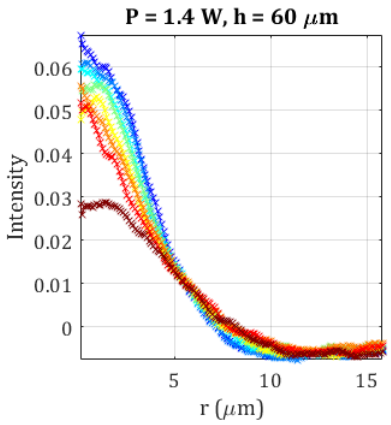


Figure 6.6: Here we only show the curves between the moment that the laser is switched off and the subsequent decrease in intensity. Blue is the earliest time and brown is the latest.

5.

Now, we focus on the intensity decrease from $I = 0.06$ about $I = 0.03$ in Figure 6.6, which happens for all droplets. Looking at the curves before the intensity decrease and the first one after it (see Figure 6.6), we see that if the first curves (blue-ish ones) show a shoulder before the decay, the last curve before the drop looks to actually go straight down. This change of shape can be explained by a bridge snap-off event. As mentioned in Chapter 5, a bridge might be formed, as shown in Figure 6.7, which can thin and snap when the laser is turned off. The snap is sudden such that right after it happens, there is a region with no colloids between the droplet and the rest of the bridge, which now recedes back to the wall. From the experiments carried

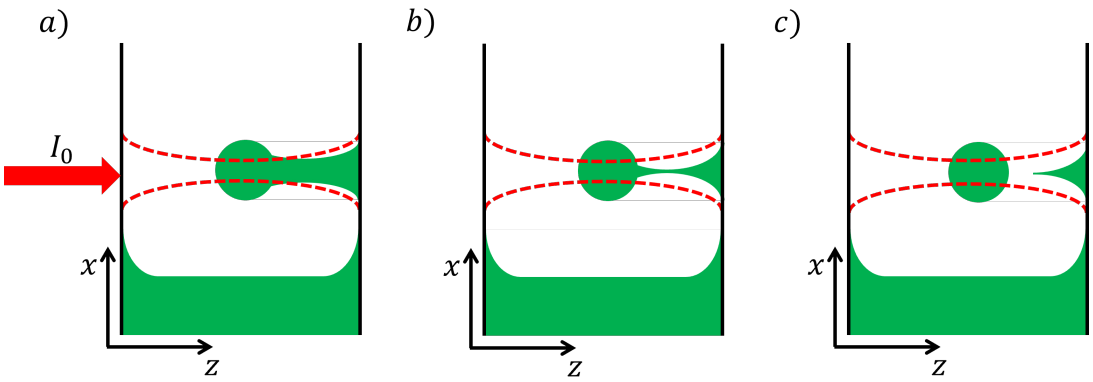


Figure 6.7: I_0 and the red arrow denote the direction of the tweezing laser beam. a) Schematic of the more realistic picture of the "droplet" that we form. b) After the laser is switched off, the bridge thins progressively until it snaps away from the droplet c), leaving the region between the droplet and the rest of the liquid phase empty of colloids, hence the drop in intensity. The bridge might be formed left and right, on only in the positive z region, if the radiation pressure is not negligible.

out first by Verhoeff *et al.* in [42], we know that when we release the interface after pinching it with a point force, the relaxation takes only a few seconds. Because these images were taken using a fluorescence microscope, we are actually imaging a superposition of $z-$planes as opposed to a thin confocal slice. As a result, after the snap off, the region between the droplet and the wall is now empty of colloids, which accounts for the decrease in intensity.

6.4.1 Droplet evaporation at height $20\,\mu$m

We now examine the evaporation of the droplets at a height $h = 20\,\mu$m above the interface. We probed two different laser powers, $P = 900\,$mW and $P = 1.4\,$W. Note that it was not possible to grow a droplet and watch it evaporate for $P = 2.1\,$W at this height as the laser also pulled the entire interface up.

These droplets are larger than the others, see in Figure 6.4. We attribute this to the proximity with the interface and the thickness of the wetting layer of the colloidal liquid on the glass wall.

The second characteristic unique to these droplets is that they sediment as they evaporate. To determine the sedimentation velocity, we track the centre of mass $O = (x_O, y_o)$ of the droplet. We find that the sedimentation velocity is constant and of $0.1\,\mu$m/s (see Figure 6.8). The velocity of a spherical object of size R and density ρ sedimenting in a fluid of density ρ_f and viscosity η is given by the equilibrium of the buoyancy force $F_b = (\rho - \rho_f)g\frac{4}{3}\pi R^3$ and Stoke's viscous

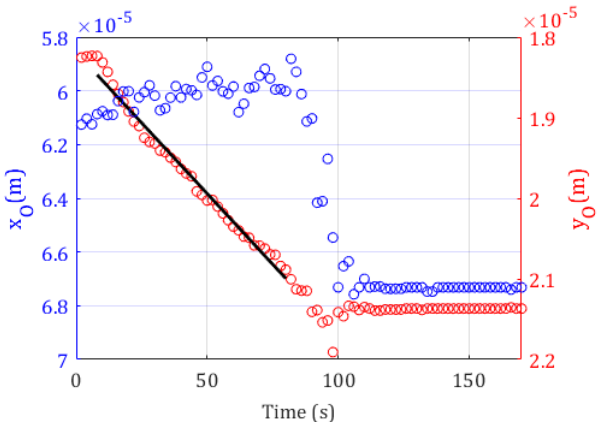


Figure 6.8: Position of the centre of the droplet (x_c, y_c) as a function of time. The symbols denote the data while the black solid line is the linear fit used to measure the sedimentation velocity. The $y-$position is constant for the first few frames until we block the laser beam and it decreases steadily. The $x-$position is constant until both x and y positions change their behaviour, at the same time, when the tracking of the droplet becomes uncertain, due to interacting with the interface.

friction force $F_s = 6\pi\eta R v$, such that we obtain

$$v = \frac{2}{9}\frac{(\rho - \rho_f)gR^2}{\eta} \tag{6.7}$$

First, we compare the sedimentation velocity we measure to that of of a droplet of PMMA of size $5\,\mu$m moving in water and we obtain $v_{\text{water}} = 90 \times 10^{-6}\,\text{Pa}\cdot\text{s}$. This value is above what we measure as the viscosity of water is lower than that of the colloidal gas phase, given the presence of Xanthan. We can also calculate that velocity for a fluid with a viscosity equal to that which we obtain through capillary waves analysis, $\eta = 3 \times 10^{-2}\,\text{Pa}\cdot\text{s}$. Note that this is the sum of the viscosities of the colloidal gas and colloidal liquid. We obtain $v = 3 \times 10^{-7}\,\text{Pa}\cdot\text{s}$, which is of the right order of magnitude with what we measure.

As shown on Figure 6.8, the tracking does not work for the entire duration of the experiment. This is due to a combination of two reasons. The first is that the droplet eventually gets too close to the interface to carry out the measurement of $I(r, \theta, t)$. For $\theta \simeq -\pi/2$, the segment $[OM]$ crosses the liquid phase. We shorten OM from 150 pixels to only 70, which corresponds to a change in length from $16\,\mu$m to $7\,\mu$m. Another reason is that the droplet has evaporated such that its density falls below the binarization threshold. In that case, the tracking is made such that it returns the last known position of the droplet, hence the flat end on the curves of $x_O(t)$ and $y_O(t)$ on Figure 6.8. For these reasons, we focus on the the images such that $t \leq 80\,\text{s}$.

Another interesting feature in this case is that the droplet interacts with the interface as

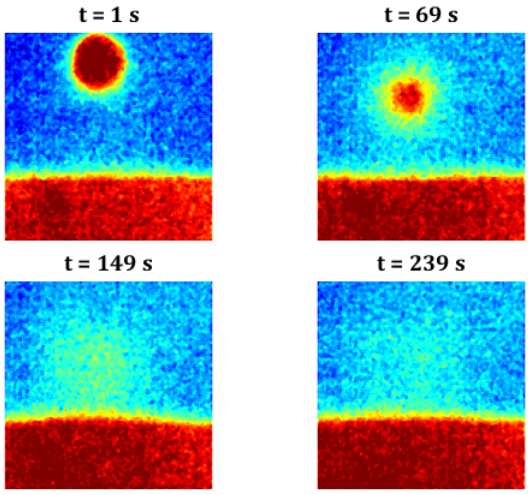


Figure 6.9: Images taken where the average position of the interface is the most deformed.

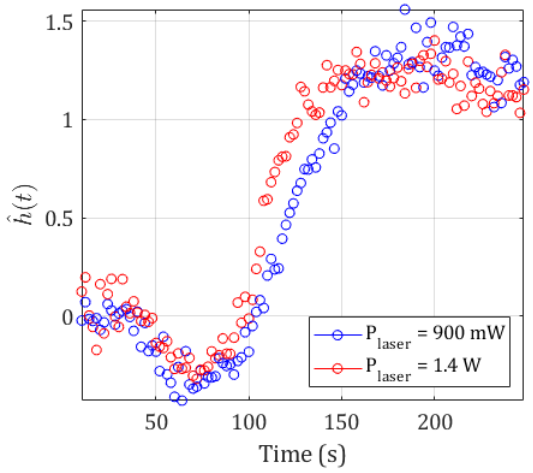


Figure 6.10: Height of the interface as a function of time, $\hat{h}(t)$.

it sediments see Figure 6.9. This prevents us from observing the full evaporation event on its own. To show the movements of the interface, we track the interface and calculate its average height as a function of time, $h_{interface}(t)$. We then plot $\hat{h} = h_{interface}(t) - h_{interface}(t = 0)$ (see Figure 6.10). At first, the droplet pushes the interface down, which is what we see from $t = 25\,\mathrm{s}$ to $t = 69\,\mathrm{s}$ on Figure 6.10. Then, when the droplet meets with the interface, the flux of new colloids make it rise up until the point where all those colloids have crossed the interface and are now mixed with the liquid phase ($t = 149\,\mathrm{s}$). Past this point, the interface relaxes down until, if we had continued taking data, it would have come back to its initial shape. Similar behaviours have been observed during phase separation of other colloid/polymer systems in [30], when droplets of colloidal liquid meet with the bulk.

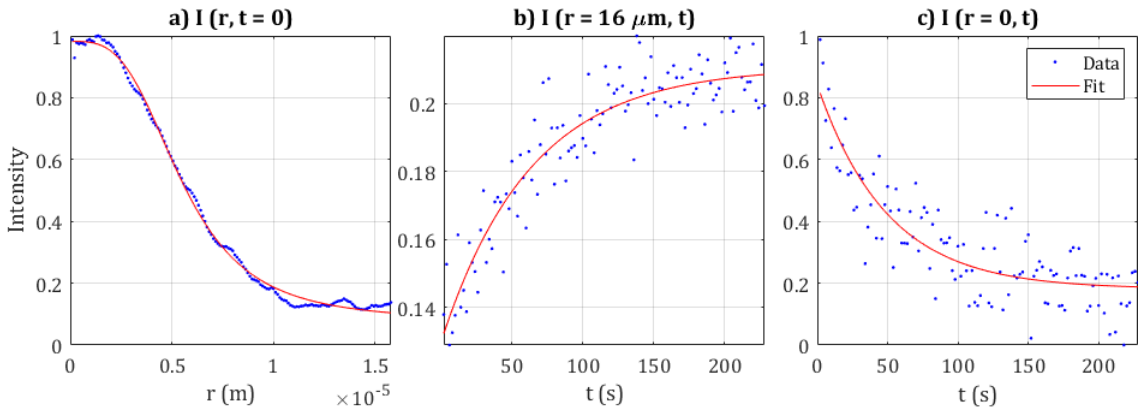


Figure 6.11: a) $I(r, t = 0)$ is the initial condition. b) $I(r = 16\,\mu\text{m}, t)$ is the boundary condition at the furthest position away from the centre of the particle. This curve is increasing. This shows that if at the beginning the region around the droplet is poor in colloids, as diffusion progresses, it gains more particles. c) $I(r = 0, t)$ is the boundary condition at the centre of the particle.

6.4.2 Droplet evaporation at heights $40\,\mu$m and $60\,\mu$m

In this case, evaporation takes place such that the position of the droplet is fixed throughout the process.

Measurement of the diffusion coefficient

As described in the theory section, the intensity of light should follow the following differential equation (see Equation 6.5)

$$\frac{\partial I}{\partial t} = D\,\frac{1}{r^2}\frac{\partial}{\partial r}\left(r^2\frac{\partial I}{\partial r}\right). \tag{6.8}$$

Measuring the diffusion coefficient D by dividing the time derivative by the spatial one is not possible given the noise in the data. Instead, to obtain a measure for D via an iterative scheme, we solve the diffusion equation numerically with an initial guess for D and then measure the error between the computed solution and the experimental data. We do this for a range of D values until the error reaches a minimum. We here demonstrate how this scheme works for the set of data taken at a height $h = 60\,\mu$m and laser power $P = 1.4\,$W. First, we need an initial condition $I(r, t = 0)$, and two boundary conditions. On is at the centre of the droplet $I(r = 0, t)$ and the other is as far away from the droplet as possible, here the segment $[OM]$ is $16\,\mu$m long at most so the second boundary condition is $I(r = 16\,\mu\text{m}, t)$ (see Figure 6.11). For the initial

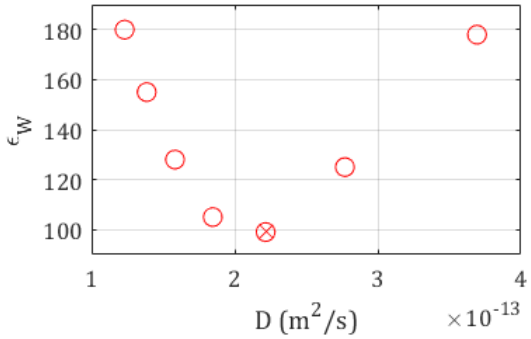


Figure 6.12: Error ϵ_W as a function of D for $\tau = \tau_0 = 20\,\mathrm{s}$. The cross denotes where the minimum is reached.

	900 mW	1.4 W	2.1 W
60 µm	1.6 $\times 10^{-13}$	2.2 $\times 10^{-13}$	2.2 $\times 10^{-13}$
40 µm	1.8 $\times 10^{-13}$	1.8 $\times 10^{-13}$	2.7 $\times 10^{-13}$

Table 6.1: Values of diffusion coefficient for all droplet evaporation experiments in m^2/s.

condition $I(r, t = 0)$ (a) in Figure 6.11, we fit the data with the following empiric fitting function

$$I(r, t = 0) = \frac{A_1}{1 + (r/B_1)^{2C_1}} + D_1. \tag{6.9}$$

The boundary condition $I(r = 16\,\mu\mathrm{m}, t)$ is fitted with $A_2\,(1 - \exp(-t/\tau_2)) + B_2$ and the one at $r = 0$ is $I(r = 0, t) = A_3\,\exp(-t/\tau_0)) + B_3$.

To calculate the error ϵ and quantify the difference between the solution computed with the guess and the experiment, we focus on the first hundred seconds of the experiment, to prevent giving too much weight to the later noise, past $t = 100\,\mathrm{s}$. Moreover, we weigh the error ϵ with a weighing function W, chosen as $W(t) = exp(-t/\tau)$, such that now the weighted error ϵ_W is

$$\epsilon_W = exp(-t/\tau) \sum_r \sum_{t<100\,\mathrm{s}} \sqrt{(I(r,t) - I_{comp}(r,t))^2}, \tag{6.10}$$

The value for τ is τ_0 that we have from the fitting of $I(r = 0, t)$. This gives us a measure for how long the decay takes. For this set of data, $\tau_0 = 22\,\mathrm{s}$ and the error reaches a minimum for $D = 2.2 \times 10^{-13}\,\mathrm{m \cdot s^{-2}}$, see Figure 6.12. The solution with the lowest error is shown Figure 6.13. Another way to see it is on Figure 6.14, where some intensity profiles are plotted either as a function of space with fixed time or vice versa, for both the experiment and the computed solution.

We run this scheme on all the six droplets and the obtained values for the diffusion co-

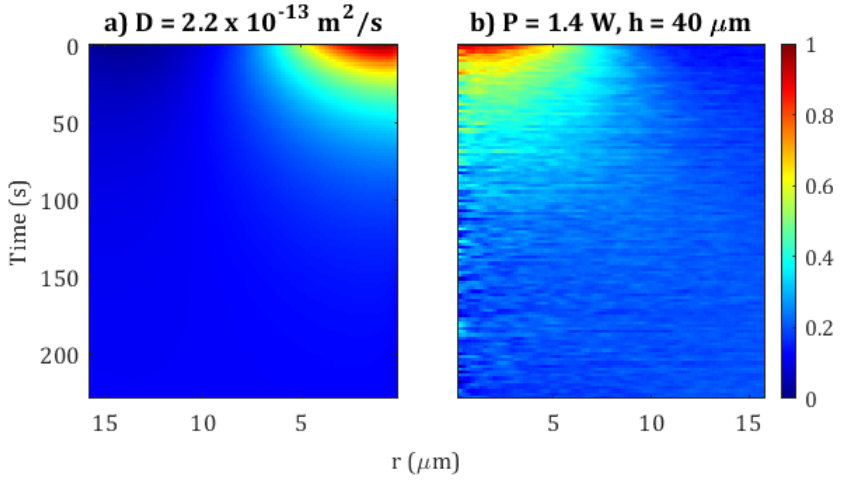


Figure 6.13: a) Solution computed numerically with the value of D that gives the lowest error. The plot was flipped for an easier comparison with b). b) Data.

efficients are summarised in Table 6.1. We compare those values to the diffusion coefficient of PMMA particles of radius R_c in water D_{water}

$$D_{water} = \frac{k_B T}{6\pi\eta R_c} = \frac{1.38 \times 10^{-23} \times 298}{6 \times \pi \times 1 \times 10^{-3} \times 100 \times 10^{-9}} = 2 \times 10^{-12}\,\mathrm{m}^2/\mathrm{s}. \tag{6.11}$$

This value is higher than what we obtain, which we attribute to the fact that the viscosity of the gas phase is higher than that of water, due to the presence of Xanthan, so D_{water} should be considered as an upper limit for D. To obtain a lower limit for D, we use the value of viscosity given by the capillary waves analysis for this statepoint, which is $\eta = 3 \times 10^{-2}\,\mathrm{Pa} \cdot \mathrm{s}$, which is in fact the sum of the viscosities of the gas and liquid phase at equilibrium [30]

$$D_{low} = \frac{k_B T}{6\pi\eta R_c} = \frac{1.38 \times 10^{-23} \times 298}{6 \times \pi \times 3 \times 10^{-2} \times 100 \times 10^{-9}} = 7 \times 10^{-14}\,\mathrm{m}^2/\mathrm{s}. \tag{6.12}$$

This value is lower than what we obtain in Table 6.1. The diffusion coefficients that we obtain (see Table 6.1) are thus of the expected order of magnitude, despite the various assumptions underlying the diffusion equation that we used, which confirms that the force driving the evaporation of the droplets is diffusion. Also we note that the diffusion coefficients are constant with respect to the height above the interface or laser power. The first is easily understandable given the gravitational height of the PMMA colloids, $l_g = \frac{k_B T}{m_b g}$, where m_b is the buoyant mass of the

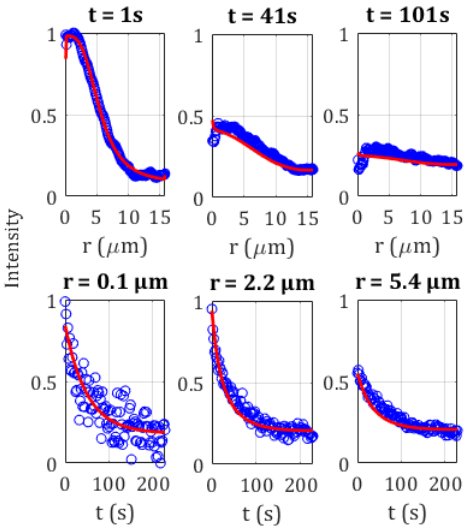


Figure 6.14: Top line: $I(r,t)$ at fixed t, bottom line: $I(r,t)$ at fixed r. The blue symbols are the data while the red lines are the solutions. The first graphs on the top and bottom lines follow the data very well as they are imposed as boundary/initial conditions. The agreement between data and numerical solution is much better than that of the first guess.

PMMA:

$$l_g = \frac{k_B T}{m_b g} = \frac{k_b T}{\frac{4}{3}\pi R^3(\rho_{PMMA} - \rho_{water})g} = \frac{1.38 \times 10^{-23} \times 298}{\frac{4}{3} \times \pi \times (1 \times 10^{-7})^3 \times (1180 - 1000) \times 9.8} = 0.5\,\text{mm}, \tag{6.13}$$

i.e. $l_g \gg h$, as we observed for the nucleation of the droplets in Chapter 5. As regards to the laser power, as seen in Chapter 5, in Figure 5.5, the maximum intensities are capped which does not allow for further conclusions.

6.5 Conclusion and outlook

The evaporation of the droplets which we nucleated using laser tweezing shows two behaviours. If the structure is close enough to the interface separating colloidal liquid and colloidal gas, then the structure is larger than further away and upon switching the laser off, it sediments at a constant velocity as it evaporates. If however the droplet was nucleated further above from the interface, then the evaporation takes place at fixed height and a diffusion coefficient of the PMMA colloids in the surrounding gas phase can be measured, with values that fall within a satisfactory order of magnitude, while using the simplest theory for diffusion.

What remains unsure is the exact geometry of the structure. The intensity decrease which

we observe here is consistent with the droplet being in fact a bridge. In that case, it would be interesting to investigate its symmetry, i.e. whether it spans through the entire 15 μm−wide sample cell or just one side as drawn in Figure 6.7. The symmetry may be broken due to the radiation pressure. But if the bridge is grown from one end of the sample cell to the other, it would be interesting to know if the snap off happens on both sides at the same time or not and watch the structure evaporate or sediment. A closer look into the exact nature of the 3D structures formed might also inform us into the density inside it. To answer these questions, a confocal setup with a trapping capacity would work.

Acknowledgments

Arran Curran is thanked for his help to build the tweezing and microscopy setup, and Taiki Yanagishima for his fruitful discussions.

Chapter 7

Conclusion and future work

In this thesis, multiple aspects of liquid-gas phase separating colloid-polymer mixtures have been studied. First, we examined the dynamics of phase separation in the nucleation and growth process for a colloid-polymer mixture. We find that there are three kinetic paths, which are observed in different parts of the phase diagram. In all of them we observe a decay of the number of droplets as a function of time. At high polymer concentration, droplets aggregate and slow down until they are frozen, which in turn stops them from growing. We speculate the growth and movement is arrested by the structure of the Xanthan polymer matrix surrounding the droplets of liquid. Another mechanism is found at lower polymer concentration and displays droplet growth with an exponent of about 1/2 and motion all along the observation time, with droplets sticking to each other. The last mechanism found at the lowest polymer concentration above the binodal line shows coalescence of the liquid droplets, which grow linearly as a function of time, until the size of the droplets exceeds the field of view that we observe, and results in macroscopic phase separation. The structure of the droplets evolves such that the size of a Voronoi cell increases linearly with the size of a droplet, which may be due to the positions of the droplets being correlated via the Xanthan matrix and strong interactions of the droplets with each other through the high q value of our system [78].

Then, we have observed the thermal fluctuations of the interface separating bubbles of colloidal gas from the surrounding colloidal liquid under confinement, with confocal microscopy. For bubbles with a radius typically smaller than $10\,\mu$m, we have measured the line tension of the interface by studying both the angular correlation function and the amplitude of the Fourier

modes associated with the fluctuations of the interface. Both measurements agree with each other and are of a good order of magnitude. For larger bubbles, extracting a line tension has not been possible as the angular correlation function presents a minimum around $\theta = 180\,^\circ$ caused by the low k modes not relaxing fully during the observation time. By comparing two droplets of the same size but at different statepoints, we have shown that bubbles at a statepoint with a lower surface tension present modes which takes longer to relax than at a statepoint with a higher surface tension. Finally, we measured the dispersion relation for this range of ω and we find that $\omega \propto k^2$.

Next, we use a home-built optical setup allowing to both observe our sample cells under fluorescence microscopy and tweeze them with an IR laser. Such a setup is used to nucleate droplets of colloidal liquid in the colloidal gas phase using optical tweezers. We did so at three different heights away from the liquid-gas interface and for three different laser powers. The height is found to have no effect on the growth kinetics or the final size of the droplet and we suggest that this might be due to the fact that h is very small compared to the gravitational length. The laser power does not influence the droplet size or the growth kinetics. However, we find that the maximum intensity of the trap is capped at a certain value, which we attribute to the nucleation of a bridge rather than a spherical droplet. The growth kinetics are found to follow a power law with an exponent of 1/2, which shows that the growth is purely driven by electrostrictive effects.

After the nucleation and growth of these droplets, we switch the laser off and study their evaporation, which shows two behaviours. If the structure is close enough to the interface separating colloidal liquid and colloidal gas, then the structure is larger than further away and upon switching the laser off, it sediments at a constant velocity as it evaporates. If however the droplet was nucleated further above from the interface, then the evaporation takes place at fixed height and a diffusion coefficient of the PMMA colloids in the surrounding gas phase can be measured, with values that fall within a satisfactory order of magnitude, while using the simplest theory for diffusion.

Future works based on these conclusions can span out in different directions. On the kinetics of phase separation, more work can be done on the Xanthan polymer matrix. As we cannot image Xanthan with our microscopy techniques, the use of rheology could lead to a better understanding of the structure of the Xanthan as its concentration is increased. Using larger

colloids could shed light on the exact mechanism of phase separation and determine whether it is RLCA or DLCA. Moreover, one could carry out the same types of experiments at higher colloid concentration and observe whether similar regimes are observed for mixtures phase separating through spinodal decomposition.

For the thermal fluctuations on a circular interface, it would be interesting to observe the fluctuations on larger droplets for longer and check that the dispersion relation also holds in that case as the phenomenology is the same. Moreover, one could observe liquid bridges and measure the dispersion relation of the waves on them. We expect them to be different as the condition for compressibility of the fluid is not verified given that the liquid can exchange colloids with the other bridges through the wetting layer on the glass.

On the laser induced nucleation and evaporation of droplets, future work could include the observation of the full 3D structure of the droplets that is grown, and checking whether it is a droplet or a bridge as we suspect. Investigating the symmetry of the bridge could reveal whether the radiation pressure plays an important role in the experiment. With a setup offering both confocal microscopy and tweezing capabilities, one could also have a better understanding of the density inside the droplet. Moreover, it would be interesting to know where exactly the bridge snaps-off during evaporation, whether it happens in the middle of the sample cell or if the radiation pressure induced by the laser breaks the symmetry here as well.

Bibliography

[1] Theodore A Wertime. Man's First Encounters with Metallurgy. 146(3649), 1964.

[2] Eduardo Guzmán, Davide Orsi, Luigi Cristofolini, Libero Liggieri, and Francesca Ravera. Two-Dimensional DPPC based emulsion-like structures stabilized by silica nanoparticles. *Langmuir*, 30(39):11504–11512, 2014.

[3] Denis Bartolo, Guillaume Degré, Philippe Nghe, and Vincent Studer. Microfluidic stickers. *Lab on a Chip*, 8(2):274–279, 2008.

[4] Pierre Guillot, Pascal Panizza, Jean Baptiste Salmon, Mathieu Joanicot, Annie Colin, Charles Henri Bruneau, and Thierry Colin. Viscosimeter on a microfluidic chip. *Langmuir*, 22(14):6438–6445, 2006.

[5] Jacques Leng and Jean Baptiste Salmon. Microfluidic crystallization. *Lab on a Chip*, 9(1):24–34, 2009.

[6] Sara Llamas, Eduardo Guzmán, Francisco Ortega, Nawel Baghdadli, Colette Cazeneuve, Ramón G. Rubio, and Gustavo S. Luengo. Adsorption of polyelectrolytes and polyelectrolytes-surfactant mixtures at surfaces: A physico-chemical approach to a cosmetic challenge. *Advances in Colloid and Interface Science*, 222:461–487, 2015.

[7] Urs T. Gonzenbach, André R. Studart, Elena Tervoort, and Ludwig J. Gauckler. Stabilization of foams with inorganic colloidal particles. *Langmuir*, 22(26):10983–10988, 2006.

[8] Douglas J. Durian and Srinivasa R. Raghavan. Making a frothy shampoo or beer. *Physics Today*, 63(5):62–63, 2010.

[9] Daniel Bonn, Jens Eggers, Joseph Indekeu, and Jacques Meunier. Wetting and spreading. *Reviews of Modern Physics*, 81(2):739–805, 2009.

[10] Herman Wijshoff. Drop dynamics in the inkjet printing process. *Current Opinion in Colloid and Interface Science*, 36:20–27, 2018.

[11] R. Tuinier H. N. W. Lekkerkerker. *Colloids and the Depletion Interaction*. Springer Link, 2011.

[12] E. Kumacheva, O. Kalinina, and L. Lilge. Three-dimensional arrays in polymer nanocomposites. *Advanced Materials*, 11(3):231–234, 1999.

[13] Anke Kuijk, Alfons Van Blaaderen, and Arnout Imhof. Synthesis of monodisperse, rodlike silica colloids with tunable aspect ratio. *Journal of the American Chemical Society*, 133(8):2346–2349, 2011.

[14] Yanyan Liu, Kazem V. Edmond, Arran Curran, Charles Bryant, Bo Peng, Dirk G.A.L. Aarts, Stefano Sacanna, and Roel P.A. Dullens. Core–Shell Particles for Simultaneous 3D Imaging and Optical Tweezing in Dense Colloidal Materials. *Advanced Materials*, 28(36):8001–8006, 2016.

[15] C. Fernández-Rico, M. Chiappini, T. Yanagishima, H. de Sousa, D.G.A.L. Aarts, M. Dijkstra, and R.P.A. Dullens. Shaping colloidal bananas to reveal biaxial, splay-bend nematic, and smectic phases. *Science*, 369(6506):960–965, 2020.

[16] Carla Fernández-Rico, Taiki Yanagishima, Arran Curran, Dirk G.A.L. Aarts, and Roel P.A. Dullens. Synthesis of Colloidal SU-8 Polymer Rods Using Sonication. *Advanced Materials*, 31(17), 2019.

[17] R. Brown. XXVII. A brief account of microscopical observations made in the months of June, July and August 1827, on the particles contained in the pollen of plants; and on the general existence of active molecules in organic and inorganic bodies . *The Philosophical Magazine*, 4(21):161–173, 1828.

[18] P. N. Pusey and W. van Megen. Phase behaviour of concentrated suspensions of nearly colloidal spheres. *Nature*, pages 2–4, 1986.

[19] Louis B.G. Cortes, Yongxiang Gao, Roel P.A. Dullens, and Dirk G.A.L. Aarts. Colloidal liquid crystals in square confinement: Isotropic, nematic and smectic phases. *Journal of Physics Condensed Matter*, 29(6), 2017.

[20] Alice L. Thorneywork, Joshua L. Abbott, Dirk G.A.L. Aarts, and Roel P.A. Dullens. Two-Dimensional Melting of Colloidal Hard Spheres. *Physical Review Letters*, 118(15):1–5, 2017.

[21] D. Quéré P.G. de Gennes, F. Brochard-Wyart. *Capillarity and Wetting Phenomena*. Springer Link, New York, 2004.

[22] François A. Lavergne, Dirk G.A.L. Aarts, and Roel P.A. Dullens. Anomalous grain growth in a polycrystalline monolayer of colloidal hard spheres. *Physical Review X*, 7(4):1–13, 2017.

[23] François A. Lavergne, Arran Curran, Dirk G.A.L. Aarts, and Roel P.A. Dullens. Dislocation-controlled formation and kinetics of grain boundary loops in two-dimensional crystals. *Proceedings of the National Academy of Sciences of the United States of America*, 115(27):6922–6927, 2018.

[24] R. P.A. Dullens, D. G.A.L. Aarts, and W. K. Kegel. Colloidal crystal-fluid interfaces. *Philosophical Magazine Letters*, 87(11):893–898, 2007.

[25] Cortes Louis. *Colloidal liquid crystals: phase behavior, dynamics and confinement.* PhD thesis, University of Oxford, 2019.

[26] Dirk G.A.L. Aarts, Matthias Schmidt, and Henk N.W. Lekkerkerker. Direct Visual Observation of Thermal Capillary Waves. *Science*, 304(5672):847–850, 2004.

[27] E. A.G. Jamie, R. P.A. Dullens, and D. G.A.L. Aarts. Spinodal decomposition of a confined colloid-polymer system. *Journal of Chemical Physics*, 137(20), 2012.

[28] E. A.G. Jamie, R. P.A. Dullens, and D. G.A.L. Aarts. Fluid-fluid demixing of off-critical colloid-polymer systems confined between parallel plates. *Journal of Physics Condensed Matter*, 24(28), 2012.

[29] Chengqian Yuan, Aviad Levin, Wei Chen, Ruirui Xing, Qianli Zou, Therese W. Herling, Pavan Kumar Challa, Tuomas P. J. Knowles, and Xuehai Yan. Nucleation and Growth of Amino Acid and Peptide Supramolecular Polymers through Liquid–Liquid Phase Separation. *Angewandte Chemie*, 131(50):18284–18291, 2019.

[30] Aarts D.G.A.L. *The interface in demixed colloid-polymer mixtures: wetting, waves and droplets.* PhD thesis, University of Utrecht, 2005.

[31] Denis Bartolo and Dirk G.A.L. Aarts. Microfluidics and soft matter: Small is useful. *Soft Matter*, 8(41):10530–10535, 2012.

[32] Lyderic Bocquet and Elisabeth Charlaix. Nanofluidics, from bulk to interfaces. *Chemical Society Reviews*, 39(3):1073–1095, 2010.

[33] Daniel B. Quinn, Jie Feng, and Howard A. Stone. Analytical model for the deformation of a fluid-fluid interface beneath an AFM probe. *Langmuir*, 29(5):1427–1434, 2013.

[34] Rene Ledesma-Alonso, Dominique Legendre, and Philippe Tordjeman. Nanoscale deformation of a liquid surface. *Physical Review Letters*, 108(10):1–5, 2012.

[35] Yuji Shimokawa and Keiji Sakai. Noncontact measurement of liquid-surface properties with knife-edge electric field tweezers technique. *Physical Review E - Statistical, Nonlinear, and Soft Matter Physics*, 87(6):4–6, 2013.

[36] Alexis Casner and Jean Pierre Delville. Laser-Induced Hydrodynamic Instability of Fluid Interfaces. *Physical Review Letters*, 90(14):4, 2003.

[37] Jean Pierre Delville, Matthieu Robert De Saint Vincent, Robert D. Schroll, Hamza Chrabi, Bruno Issenmann, Régis Wunenburger, Didier Lasseux, Wendy W. Zhang, and Etienne Brasselet. Laser microfluidics: Fluid actuation by light. *Journal of Optics A: Pure and Applied Optics*, 11(3), 2009.

[38] A. Ashkin. Acceleration and Trapping of Particles by Radiation Pressure. *Physical Review Letters*, 24(4):156–159, 1970.

[39] A. Ashkin, J. M. Dziedzic, J. E. Bjorkholm, and Steven Chu. Observation of a single-beam gradient force optical trap for dielectric particles. *Optics Letters*, 11(5):288–290, 1986.

[40] A. Ashkin, J. M. Dziedzic, and T. Yamane. Optical trapping and manipulation of single cells using infrared laser beams. *Nature*, 330(12):769–711, 1987.

[41] Justin E. Molloy and Miles J. Padgett. Lights, action: Optical tweezers. *Contemporary Physics*, 43(4):241–258, 2002.

[42] A. A. Verhoeff, F. A. Lavergne, D. Bartolo, D. G.A.L. Aarts, and R. P.A. Dullens. Optical trapping of interfaces at ultra-low interfacial tension. *Soft Matter*, 11(16):3100–3104, 2015.

[43] A Einstein. On the movement of small particles suspended in stationary liquids required by molecular-kinetic theory of heat, 1905.

[44] Sara Romer, Claus Urban, Hugo Bissig, Anna Stradner, Frank Scheffold, and Peter Schurtenberger. Dynamics of concentrated colloidal suspensions: Diffusion, aggregation and gelation. *Philosophical Transactions of the Royal Society A: Mathematical, Physical and Engineering Sciences*, 359(1782):977–984, 2001.

[45] J. P. Hansen and I. R. McDonald. *Theory of Simple Liquids*. Academic Press, 1986.

[46] B. V. Derjaguin and L. D. Landau. Theory of the stability of strongly charged lyophobic sols and of the adhesion of strongly charged particles in solutions of electrolytes. *Acta Physicochim*, 14:633, 1941.

[47] E J W Verwey and J T G Overbeek. Theory of the Stability of lyophobic colloids. pages 631–636, 1946.

[48] J. N. Israelachvili. *Intermolecular and surface forces: revised third edition*. Academic Press, 2011.

[49] Sho Asakura and Fumio Oosawa. On interaction between two bodies immersed in a solution of macromolecules. *The Journal of Chemical Physics*, 22(7):1255–1256, 1954.

[50] Sho Asakura and Fumio Oosawa. Interaction between particles suspended in solutions of macromolecules. *Journal of Polymer Science*, 33(126):183–192, 1958.

[51] A. Vrij. POLYMERS AT INTERFACES AND THE INTERACTIONS IN COLLOIDAL DISPERSIONS. *Colloid and Surface Science*, pages 471–483, jan 1977.

[52] S. M Ilett, A. Orrock, W. C. K. Poon, and P. N. Pusey. Phase behavior of a model colloid-polymer mixture. *Physical Review E*, 51:1344–1353, 1995.

[53] Mandelstam L. Über die Rauhigkeit freier Flüssigkeitsoberflächen. *Ann. Phys.*, 41:609–624, 1913.

[54] A. Vrij. Equation for the interfacial tension between demixed polymer solutions. *Journal of Polymer Science Part A-2: Polymer Physics*, 6(11):1919–1932, 1968.

[55] D. G. A. L. Aarts. Direct Visual Observation of Capillary Waves. *Science*, 847(2004):847–850, 2010.

[56] Bharat (California Institure for Quantitative Biosciences) Jagannathan and Susan (California Institue for Quantitative Biosciences) Marqusee. Protein Folding and Unfolding Under Force. *Biopolymers*, 99(11):860–869, 2013.

[57] M. Milas, M. Rinaudo, and B. Tinland. The viscosity dependence on concentration, molecular weight and shear rate of xanthan solutions. *Polymer Bulletin*, 14(2):157–164, 1985.

[58] I. Capron, G. Brigand, and G. Muller. About the native and renatured conformation of xanthan exopolysaccharide. *Polymer*, 38(21):5289–5295, 1997.

[59] G. H. Koenderink, D.G.A.L. Aarts, Volkert W.A. de Villeneuve, Albert P. Philipse, Remco Tuinier, and Henk N.W. Lekkerkerker. Morphology and kinetics of phase separating transparent xanthan-colloid mixtures. *Biomacromolecules*, 4(1):129–136, 2003.

[60] G. H. Koenderink, S. Sacanna, D.G.A.L. Aarts, and A. P. Philipse. Rotational and translational diffusion of fluorocarbon tracer spheres in semidilute xanthan solutions. *Physical Review E - Statistical, Nonlinear, and Soft Matter Physics*, 69(2 1):1–12, 2004.

[61] G. Bosma, C. Pathmamanoharan, Els H.A. De Hoog, Willem K. Kegel, Alfons Van Blaaderen, and Henk N.W. Lekkerkerker. Preparation of monodisperse, fluorescent PMMA-latex colloids by dispersion polymerization. *Journal of Colloid and Interface Science*, 245(2):292–300, 2002.

[62] W. D. Harkins. A General Theory of the Mechanism of Emulsion Polymerization. *Journal of the American Chemical Society*, 69(6):1428–1444, 1947.

[63] J Willard Gibbs. *The collected works of J. Willard Gibbs, volume I: thermodynamics*. Yale University Press, 1928.

[64] H. Abdul Razak. *Wetting behaviour of colloid-polymer mixtures in confinement*. PhD thesis, University of Oxford, 2017.

[65] Anthony A. Hyman, Christoph A. Weber, and Frank Jülicher. Liquid-liquid phase separation in biology. *Annual review of cell and developmental biology*, 30:39–58, 2014.

[66] Younghwan Kwon. Study on micron-sized colloidal ink formulations and colloidal patterns by inkjet printing. *Molecular Crystals and Liquid Crystals*, 584(1):123–130, 2013.

[67] Simon Alberti, Amy Gladfelter, and Tanja Mittag. Considerations and Challenges in Studying Liquid-Liquid Phase Separation and Biomolecular Condensates. *Cell*, 176(3):419–434, 2019.

[68] R. M.L. Evans, W. C.K. Poon, and F. Renth. Classification of ordering kinetics in three-phase systems. *Physical Review E - Statistical Physics, Plasmas, Fluids, and Related Interdisciplinary Topics*, 64(3):13, 2001.

[69] V. J. Anderson, E. H.A. de Hoog, and H. N.W. Lekkerkerker. Mechanisms of phase separation and aggregation in colloid-polymer mixtures. *Physical Review E - Statistical Physics, Plasmas, Fluids, and Related Interdisciplinary Topics*, 65(1):1–8, 2002.

[70] D.A. Weitz, J.S. Huang, M.Y. Lin, and J. Sung. Limits of the Fractal Dimension for Irreversible Kinetic Aggregation of Gold Colloids. *Physical Review Letters*, 54(13):1416–1419, 1985.

[71] Eric D. Siggia. Late stages of spinodal decomposition in binary mixtures. *Physical Review A*, 20(2):595–605, 1979.

[72] K. Binder. Theory for the dynamics of "clusters." II. Critical diffusion in binary systems and the kinetics of phase separation. *Physical Review B*, 15(9):4425–4447, 1977.

[73] E. K. Hobbie. Depletion-driven phase separation and reversible aggregation in confined colloidal mixtures. *Langmuir*, 15(26):8807–8812, 1999.

[74] J.W. Cahn and J.E. Hilliard. Free energy of a nonuniform system. I. Interfacial free energy. *The Journal of Chemical Physics*, 28(2):258–267, 1958.

[75] J.W. Cahn and J.E. Hilliard. Free energy of a nonuniform system. III. Nucleation in a two-component incompressible fluid. *The Journal of Chemical Physics*, 31(3):688–699, 1959.

[76] J.W. Cahn. On spinodal decomposition in cubic crystals. *Acta Metallurgica*, 10(3):179–183, 1962.

[77] J.W. Cahn. Phase separation by spinodal decomposition in isotropic systems. *The Journal of Chemical Physics*, 42(1):93–99, 1965.

[78] R.W. Style, T. Sai, N. Fanelli, M. Ijavi, K. Smith-Mannschott, Qin Xu, Lawrence A. Wilen, and Eric R. Dufresne. Liquid-Liquid Phase Separation in an Elastic Network. *Physical Review X*, 8(1):11028, 2018.

[79] Kilian Dietrich, Damian Renggli, Michele Zanini, Giovanni Volpe, Ivo Buttinoni, and Lucio Isa. Two-dimensional nature of the active Brownian motion of catalytic microswimmers at solid and liquid interfaces. *New Journal of Physics*, 19(6), 2017.

[80] Samo Penič, Aleš Iglič, Isak Bivas, and Miha Fošnarič. Bending elasticity of vesicle membranes studied by Monte Carlo simulations of vesicle thermal shape fluctuations. *Soft Matter*, 11(25):5004–5009, 2015.

[81] Isak Bivas. Shape fluctuations of nearly spherical lipid vesicles and emulsion droplets. *Physical Review E - Statistical, Nonlinear, and Soft Matter Physics*, 81(6):1–10, 2010.

[82] Hammad A. Faizi, Cody J. Reeves, Vasil N. Georgiev, Petia M. Vlahovska, and Rumiana Dimova. Fluctuation spectroscopy of giant unilamellar vesicles using confocal and phase contrast microscopy. *Soft Matter*, 16(39):8996–9001, 2020.

[83] F Brochard and JF Lennon. Frequency spectrum of the flicker phenomenon in erythrocytes. *Journal de Physique*, 36(11):1035–1047, 1975.

[84] Savoie Charles. Thermal capillary waves in confinement. Master's thesis, University of Oxford, Université de Lyon, ENS de Lyon, 2011.

[85] Erkan Tüzel, Guoai Pan, and Daniel M. Kroll. Dynamics of thermally driven capillary waves for two-dimensional droplets. *Journal of Chemical Physics*, 132(17), 2010.

[86] Shia Yen Teh, Robert Lin, Lung Hsin Hung, and Abraham P. Lee. Droplet microfluidics. *Lab on a Chip*, 8(2):198–220, 2008.

[87] T. Trantidou, M. S. Friddin, A. Salehi-Reyhani, O. Ces, and Y. Elani. Droplet microfluidics for the construction of compartmentalised model membranes. *Lab on a Chip*, 18(17):2488–2509, 2018.

[88] J Tai, H.Y. Gan, Y.N. Liang, and B.K. Lok. Control of Droplet Formation in Inkjet Printing Using Ohnesorge Number Category: Materials and Processes. *10th Electronics Packaging Technology Conference*, 2008.

[89] J. P. Delville, C. Lalaude, and A. Ducasse. Kinetics of laser-driven phase separation induced by a tightly focused wave in binary liquid mixtures. *Physica A: Statistical Mechanics and its Applications*, 262(1-2):40–68, 1999.

[90] Revie. Kinetics of nucleation in near-critical fluids. *Journal of Aerosol Science*, 11(1):112, 1980.

[91] B Pouligny, B Jean-Jean, E Freysz, A Ponton, and A Ducasse. Nonlinear propagation of Gaussian beams in binary critical liquid mixtures. 39(10):5268–5279, 1989.

[92] S. Duhr and D. Braun. Why molecules move along a temperature gradient. *Proceedings of the National Academy of Sciences of the United States of America*, 103(52):19678–19682, 2006.

[93] I. O. GÖTZE, J. M. Brader, M. Schmidt, and H. LÖWEN. Laser-induced condensation in colloid—polymer mixtures. *Molecular Physics*, 101(11):1651–1658, 2003.

[94] J Monteith. Evaporation and environment. *Symposia of the Society for Experimental Biology*, (19):205–234, 1965.

[95] H.L. Penman. Evaporation: an introductory survey. *Netherlands Journal of Agricultural Science*, 4(1):9–29, 1956.

[96] William G. Dedert. Evaporation. *Industrial and Engineering Chemistry*, 53(8):669–673, 1961.

[97] Rachael E.H. Miles, Kerry J. Knox, Jonathan P. Reid, Adèle M.C. Laurain, and Laura Mitchem. Measurements of mass and heat transfer at a liquid water surface during condensation or evaporation of a subnanometer thickness layer of water. *Physical Review Letters*, 105(11):1–4, 2010.

[98] Yeseul Kim, Marta Gonçalves, Deok Ho Kim, and Byung Mook Weon. Topological heterogeneity and evaporation dynamics of irregular water droplets. *Scientific Reports*, 11(1):1–7, 2021.

[99] Finlay Walton and Klaas Wynne. Control over phase separation and nucleation using a laser-Tweezing potential. *Nature Chemistry*, 10(5):506–510, 2018.

[100] Francis D Pope, Hai-jie Tong, Ben J Dennis-smither, Paul T Griffiths, Simon L Clegg, Jonathan P Reid, and R Anthony Cox. Mixtures with Sodium Chloride . II . Liquid-State Vapor Pressures of the Acids. pages 10156–10165, 2010.

[101] Binita Pathak, Sandeep Hatte, and Saptarshi Basu. Evaporation Dynamics of Mixed-Nanocolloidal Sessile Droplets. *Langmuir*, 33(49):14123–14129, 2017.

Acknowledgements

I would like to thank the team in the lab, sarting with Roel and Dirk's guidance all along. Their patience and support may it be scientific or moral support have been crucial for me throughout this project. Taiki's wisdom, Arran's expertise, Berend's coding genius, Petit Chef Louis, François's incredible glasses game, Joanne, Carla, Nick, Ruth, Joe, Miranda, Camille, Adam and Mariana's patience with me and my baby chemistry questions have been incredible. It has been inspiring to work and grow among such talented people and in the end, I remember how to cook colloids as much as I remember the long discussions about why bananas are/should be bent.

Bien sûr, le goût de la physique, je le dois à Marc Bigorre et à Laurent Potier.

Cependant, mes remerciements les plus chers vont à ma famille: Papa, un modèle de sagesse qui m'a transmis la patience et la persévérance dont j'ai eu tant besoin à travers ce travail de recherche, et Maman, un héros sans cape ni costume qui m'a toujours soutenue et guidée, inconditionnellement. Shahinez et Bédis, votre énergie et votre vivacité m'ont inspirée et poussée. 3ami Raouf, Tata Amina, Fadhila, Sara et Ihsen, merci pour la force que vous me donnez et les encouragements qui m'ont facilité le travail. Les escape game à la maison, et celui où on s'est perdu dans la nuit dans un champ de maïs sont symboliques de ce que ce travail de thèse a été pendant ces 4 ans: un parcours dans l'inconnu mais entourée des meilleures personnes possibles et guidée par des indices, des réflexions et des discussions. Merci.